Chem Soc Rev

REVIEW ARTICLE

View Article Online
View Journal | View Issue

Cite this: *Chem. Soc. Rev.*, 2022, **51**, 8923

Multi-atom cluster catalysts for efficient electrocatalysis

Libo Sun,[ab] Vikas Reddu [a] and Xin Wang *[ab]

Multi-atom cluster catalysts have turned out to be novel heterogeneous catalysts with atomic dispersion for electrochemical energy applications. Beyond a simple combination of single-atom catalysts, they could offer boosted activity as a result of the synergistic effects between adjacent atoms. Meanwhile, the multiple active sites in the catalytic center may render them versatile binding modes toward adsorbates and provide an opportunity for catalyzing complex reactions with diverse products. Herein, a comprehensive review of the recent development of multi-atom cluster catalysts for electrochemical energy applications is provided. Specifically, the origin of synergistic effects in multi-atom cluster catalysts and related modulation methods are illustrated and summarized. The introduction of multi-atom cluster catalysts to circumvent the scaling relationships as well as their potential for developing new descriptors is then discussed. Subsequently, the methods for fabricating multi-atom cluster catalysts and related characterization techniques are reviewed. This is followed by the discussion of their application in key electrochemical reactions such as water splitting, oxygen reduction, and carbon dioxide/monoxide reduction, as well as the real-time techniques for their mechanistic study. Finally, the future challenges and opportunities concerning the improvement of multi-atom cluster catalysts are outlined, which are essential to make such electrocatalysts viable for electrochemical energy conversion.

Received 10th July 2022

DOI: 10.1039/d2cs00233g

rsc.li/chem-soc-rev

[a] *School of Chemical and Biomedical Engineering, Nanyang Technological University, 62 Nanyang Drive, Singapore 637459, Singapore. E-mail: WangXin@ntu.edu.sg*
[b] *Cambridge Centre for Advanced Research and Education in Singapore Ltd (Cambridge CARES), CREATE Tower, Singapore 138602, Singapore*

1. Introduction

Practical application of electrocatalytic energy conversion relies on the availability of electrocatalysts with high activity, selectivity, and durability. Noble metal (Pt, Au, Ru, Ir, *etc.*) based

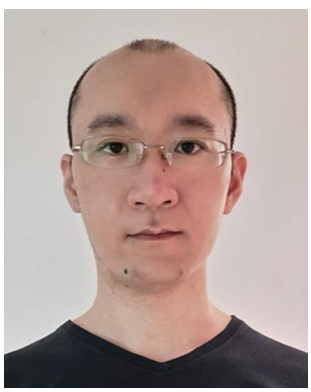

Libo Sun

Libo Sun received his bachelor's degree in chemistry (2009) from Jilin University. Then, he received his PhD in inorganic chemistry (2014) under the supervision of Prof. Jihong Yu from the State Key Laboratory of Inorganic Synthesis & Preparative Chemistry, Jilin University. He then started his further research in The University of Hong Kong and Nanyang Technological University. In 2017, he joined Prof. Xin Wang's group and worked in the Cambridge Centre for Advanced Research and Education in Singapore. His current research focuses on heterogeneous electrocatalytic CO_2 reduction and nitrate reduction with advanced molecular and cluster catalysts.

Vikas Reddu

Vikas Reddu received his BE (Hons.) degree in chemical engineering from Birla Institute of Technology and Science (India) in 2013, and his PhD in 2022 from Nanyang Technological University, under the supervision of Prof. Xin Wang. He has been working on electrocatalytic reduction of carbon dioxide to fuels and feedstocks. His research interests include electrochemical energy conversion and storage technologies.

electrocatalysts have been used for electrocatalytic CO_2 reduction reaction (CO_2RR), hydrogen evolution reaction (HER), oxygen evolution/reduction reaction (OER/ORR), nitrogen reduction reaction (NRR), *etc.*[1–5] However, the high cost and natural scarcity of these materials accompanied by insufficient activity hamper their large-scale applications. An alternative choice is to develop either non-precious metal electrocatalysts or noble metal-based electrocatalysts with highly efficient atom utilization and activity, which can tackle the above-mentioned problems while maintaining excellent performance.

Recently, catalysts dispersed at an atomic scale have drawn tremendous research interest for being good candidates for various applications.[6] It is widely accepted that the catalysts dispersed at an atomic scale can exhibit better performance with improved atom utilization than the bulk ones due to the unsaturated metal environment and unique electronic structure.[7,8] Recent studies have confirmed that single-atom catalysts (SACs) demonstrate a boost in catalytic performance in many electrocatalytic applications.[9,10] The strategy of using SACs could further facilitate their intrinsic performance by careful tuning of their coordination and electronic configurations.[11] Although great breakthroughs have been achieved by using SACs, a major shortcoming of these catalysts is the lack of structure complexity, which makes them unsuitable when faced with complex reactions. As such, complex reactions follow various reaction pathways *via* diverse intermediates to form multiple products with the assistance of multiple active sites on a catalyst.[12–15] Besides, the single active site of SAC materials makes it unlikely for them to be able to regulate the binding modes of adsorbed intermediates during reactions due to the lack of diverse synergistic interactions,[16–18] thus limiting their ability to surpass the intrinsic performance by circumventing the scaling relationship.[19] This calls for further development of suitable electrocatalysts.

Xin Wang

Prof. Xin Wang is Cheng Tsang Man Chair Professor in Energy at Nanyang Technological University, Singapore. He received his bachelor's (1994) and master's (1997) degrees in chemical engineering from Zhejiang University, and PhD (2002) in chemical engineering from Hong Kong University of Science and Technology. He has research interest in nanostructure control, surface functionalization and interface tuning for selective electrocatalysis towards key electrochemical reactions for energy and environmental applications. He is a Fellow of the Academy of Engineering, Singapore, and a Fellow of the Royal Society of Chemistry.

The introduction of additional metal atoms in the vicinity of single active sites of SACs to form multi-atom cluster catalysts, including dual atom catalysts (DACs), triple atom catalysts (TACs), *etc.*, could allow for the inheritance of the atomic dispersity, high atomic utilization, high activity and selectivity of SACs, and break the intrinsic limits as well.[20–26] To date, research on multi-atom cluster catalysts has revealed the opportunities in various applications, such as CO oxidation,[27–30] NO oxidation,[31,32] CO_2 hydrogenation,[33–35] glycerol hydrogenolysis,[36] alkene epoxidation,[37] oxidation of alcohols,[38] semi-hydrogenation of alkynes, and Suzuki coupling reaction along with other applications.[39–43] Although their development is still at an early stage, they already exhibit fascinating activity.[44] Notably, Fe–Co hetero-DAC exhibited superior oxygen reduction activity compared to Pt/C and its counterpart SACs.[45] The efficient activation of the binding of O_2 allows it to perform stably in H_2/O_2 fuel cells. The Ni/Fe–N–C hetero-DAC is highly selective ($>90\%$) for CO_2RR to produce CO over a wide potential range (-0.5 to -0.9 V *vs.* reversible hydrogen electrode (RHE)), wherein 98% selectivity could be obtained at -0.7 V *vs.* RHE with good long-term stability for at least 30 h.[46] Pt–Ru hetero-DAC also exhibited greatly improved hydrogen evolution activity and stability when compared to that of commercial Pt/C.[47] These studies proved that the multi-atom cluster catalysts could exhibit excellent electrocatalytic activity. One advantage of using these catalysts is that such materials can provide multiple active sites to bind with the adsorbent and optimize the binding mode through C-, O- and N-binding sites, which favor complex reaction paths and formation of complex products.[48] Moreover, through the synthesis of either homo- or hetero- multi-atom clusters, their electronic structure can be systematically tuned, thus providing a desired synergistic effect altering their intrinsic catalytic ability, which in turn renders the possibility to tune a reaction.[49,50]

Considering that multi-atom cluster catalysts are still in their infancy for electrocatalytic applications, we hope that through a thorough compilation of published work on multi-atom cluster electrocatalysts, a clear fundamental research map could be established (Fig. 1). Different from SACs, the synergistic effect that exists in multi-atom cluster catalysts (either homo- or hetero-atom clusters) is one of their main characteristics and contributes the most to boosted activity. The synergistic effect may affect the electronic structure of active centers and the binding behaviour of intermediates, and thus, the necessary parameters behind it and the methods of modulating these parameters are discussed first (including interatomic interaction, coordination environment, and substrate interactions). Subsequently, the theoretical understanding of the influence on the scaling relationships arising from the multi-atom cluster catalysts and the descriptors that may affect the intrinsic activity of such electrocatalysts are discussed. Then, as precisely controlled fabrication of multi-atom cluster catalysts remains a challenge, recently developed methods and related characterization techniques are reviewed to inspire more advanced preparation strategies. Furthermore, the experimental applications in CO_2RR, OER/ORR, HER, and NRR as

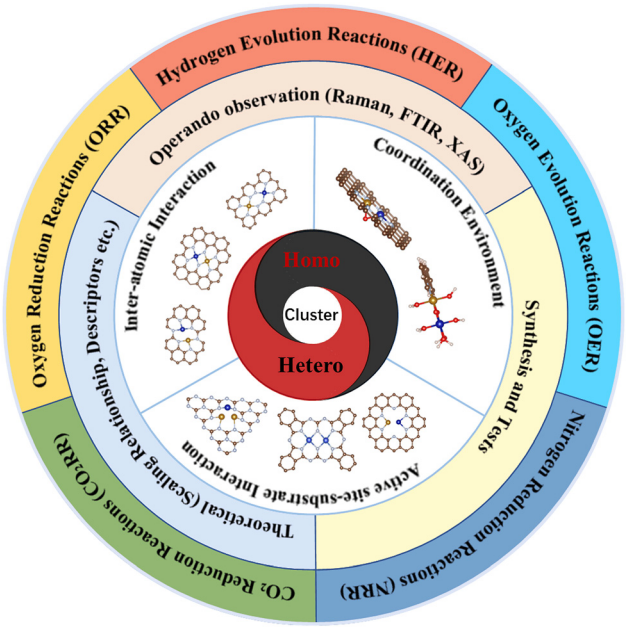

Fig. 1 Schematic view of topics covered in the review for the advancement of multi-atom cluster catalysts.

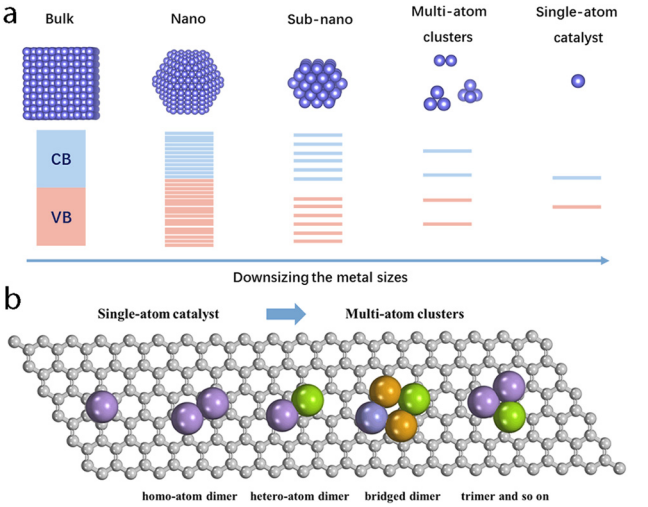

Fig. 2 (a) Representative geometric and electronic differences of materials with diverse sizes. (b) Possible multi-atom cluster catalysts.

well as the real-time techniques for mechanism investigation are summarized for a better understanding of the advantages of using multi-atom cluster catalysts. We hope this review could inspire interested readers in the further development of multi-atom cluster electrocatalysts.

2. Synergistic effects in multi-atom cluster catalysts

2.1 Synergistic effects

The synergistic effect plays a key role in boosting the performance of an electrocatalyst. It is believed that such an effect may be derived from the combined benefit from the components A and B forming synergistic $(A + B)_{syn}$, which should render higher activity outperforming the individual components A and B, so that $(A + B)_{syn} > A + B$. As the electrocatalytic reactions usually take place on a surface, any modification of the surface may affect its ability to interact with adsorbates.[51–53] Evidence suggests that either the electronic or geometric modifications of a surface can lead to a synergistic effect, resulting in improved activity, selectivity, or stability of a catalyst.[54–56] The synergistic effects are common in nanostructures, where the electronic and geometric modifications can be achieved by various techniques such as alloying, segregation-driven interphase formation, core–shell modification, *etc.*[57,58]

2.2 The origin of synergistic effects in multi-atom cluster catalysts

It is necessary to specify the scope of multi-atom cluster catalysts discussed in this work (Fig. 2a). According to the equation by Kubo,[59] the band gap (δ) can be approximately expressed as follows:

$$\delta = \frac{4\varepsilon}{3N} \quad (1)$$

where the ε is the Fermi level energy and N is the atom number of the metal particles. In this equation, the particle will lose the metallic state when δ exceeds the thermal energy of kT (k is the Boltzmann constant, T is the temperature) with a smaller atom number. Therefore, when the sizes of active metal species are decreased, their electronic structures may change from continuous valence bands of bulk materials to discrete HOMO-LUMO states.[60] Previous research suggested that besides the bulk materials, the metal nanoparticles (>2 nm) may exhibit a relatively continuous valence band. Then, for smaller metal nanoparticles with a particle size of above 1 nm, the so-called sub-nano materials can exhibit a relatively discrete state with a narrow bandgap.[61–63] When further decreasing the particle size to the cluster region, the discrete HOMO–LUMO state is significant, and the electronic state of these clusters could be affected by the surrounding environment. In this review we limit our discussion to multi-atom cluster catalysts.

As shown in Fig. 2b, multi-atom cluster catalysts may possess diverse configurations in electrocatalysis, including homo- and hetero-atom clusters such as homo-atom dimers, hetero-atom dimers, bridged dimers, homo- or hetero-atom trimers, and so on. The presence of various configurations in multi-atom cluster catalysts suggests that diverse interactions exist between various metal atom sites, and they cannot simply be regarded as separated entities.[64–66] Therefore, the construction of multi-atom cluster catalysts usually results in significantly different catalytic activity than that of single-atom catalysts.[67] The main factor leading to this observed difference is usually attributed to the synergistic effects after the introduction of additional atoms in the active centers. However, further explanation behind the synergistic effect is necessary. Through tuning the local geometric and electronic configuration of

active sites,[68–72] various parameters, such as the degree of d-band filling, the spin state, charge difference, electronegativity, and so on, could be systematically regulated, which may be used to explain the origin of synergistic effects of multi-atom cluster catalysts (Fig. 4a–c).[73–78] When such modified active centers are involved in the interaction with an adsorbate, they could optimize the binding mode, leading to effective activation of the adsorbate and optimized reaction energies, eventually tuning the activity of multi-atom cluster catalysts (Fig. 3a).

Specifically, after the incorporation of multi-atoms, the orbitals of metals and adsorbates could overlap with each other through more efficient orbital interactions with optimized σ or π donation, and π* back-donation bonds, leading to better activation of the adsorbates (Fig. 3b).[79–86] As such, Jiang *et al.* established $TM_2@C_2N$ (M = Pt, Co, Ni, Cu) dual atom models and compared them with their counterpart $TM@C_2N$ for ORR.[87] Taking $Co_2@C_2N$ as an example, $Co_2@C_2N$ presented remarkably higher adsorption energy (2.39 eV) for the O_2 molecule with side-on binding configuration than $Co@C_2N$ (1.18 eV) with end-on binding configuration. Therefore, the O–O bond length of 1.22 Å in the free O_2 molecule was elongated to 1.47 Å with $Co_2@C_2N$, which was longer than 1.33 Å in $Co@C_2N$. This could be ascribed to a shifted d-band center to the Fermi level, which increased orbital coupling between Co 3d orbital and O_2 2p orbital. This may have increased charge transfer to O_2 from 0.51 to $0.76e^-$, thus leading to better dissociation of O_2 for ORR with dual atom configuration of metal atoms.

The spin polarization of multi-atom cluster catalysts also plays a role in electrocatalytic reactions.[88,89] For instance, as oxygen is a paramagnetic molecule, the ferromagnetic half-metal (HM, with one spin-orbital crossing the Fermi level) of [(Co and/or Fe)-N_x-gra, x = 1–6] dual sites with spin-polarized electrons could create a moderate non-uniform magnetic field to couple and activate O_2 in ORR.[90] Meanwhile, the formation of the O–O intermediate in OER also requires spin conservation to yield the paramagnetic triplet state of oxygen by interaction with active centers. Thus, the spin-polarization of Co–Fe dual atoms could guarantee the parallel spin alignment of oxygen molecules during the reaction, to facilitate either the activation of O_2 in ORR or the formation of O–O in OER. Therefore, the spin polarization was capable of describing the activity of ORR and OER, wherein the spin moment of Fe should be between 0.4 and 1.5μ_B for an ideal dual atom Fe–Co bifunctional electrocatalyst. Recently, Zhang *et al.* reported the incorporation of Mn in the vicinity of Fe to regulate it from a low spin state of $t_{2g}5e_g0$ to an intermediate spin state of $t_{2g}4e_g1$.[88] This one e_g electron (d_{z^2} orbital) may couple with the anti-bonding π-orbital of oxygen and activate it to improve the ORR.

In general, the surface polarized active sites may also indicate the existence of strong interactions with the intermediates during reactions. For instance, Chen *et al.* calculated and found that $Cu_2@C_2N$ may synergistically exhibit a large charge density of $+0.62e^-$ than that of Cu-bonded N atoms ($-0.09e^-$) during CO_2RR.[91] Later, Zapol *et al.* found that for bimetallic dimers,

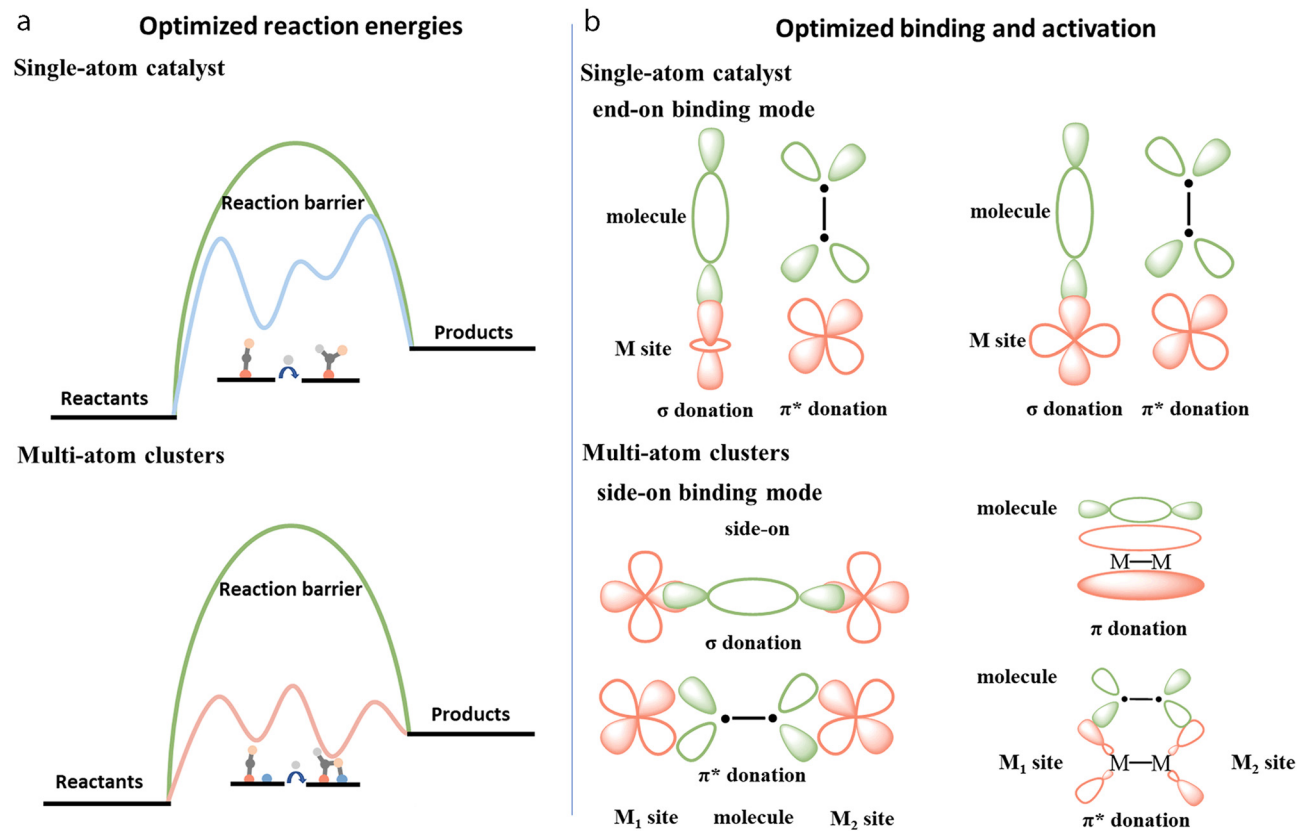

Fig. 3 Illustration of (a) optimized reaction energies, and (b) binding and activation of multi-atom cluster catalysts when compared with single-atom catalysts.

the charge difference (ΔQ(N–M)) was linearly correlated with the electronegativity difference ($\Delta\chi_{M-N}$).[76] Accordingly, the total electron transfer from the metal dimers to the substrate could be described using $\chi_{MN} = 0.69\chi_N + 0.31\chi_M$. This equation suggested that the total charge transferred between the cluster and the substrate is related to the electronegativity difference of metals. This charge transfer may affect the subsequent binding strength of intermediates during reactions. Later, Wu *et al.* were able to establish an equation of $\eta = 5.67\Delta\chi + 0.13$ to describe such relationships of activity with the electronegativity difference.[92] Du *et al.* found that in the Mo–Ru model for NRR, the Mo-end could transfer $0.35e^-$ and the Ru-end could transfer $0.18e^-$ to the N_2 molecule.[93] Thus, the electrons in the d orbitals of Mo and Ru atoms may be donated to the empty π^* orbital of N atoms to activate the triple bond in N_2. In contrast, the N_2 molecule on the SAC may have one N atom gaining electrons and the other one losing electrons. The charge difference of N atoms adsorbed onto Mo and Ru could also polarize the N_2 molecule to further weaken the triple bond. Besides, through the bond order analysis of projected crystal orbital Hamilton popular (pCOHP), the integrated pCOHP value (ICOHP) of −7.19 for the adsorbed N–N bond on Mo–Ru was also closer to the Fermi level than that of −10.15 on the Ru SAC, suggesting a stronger N–N bond for the latter when interacting with the N_2 molecules.

2.3 Techniques in modulating key parameters

In the above section, we mentioned that the parameters such as the degree of d-band filling, the magnetic moment, charge difference, and electronegativity could result in the synergistic effects of multi-atom cluster catalysts. As these parameters are physical variables experimentally adjustable, the understanding of such parameters from an experimental point of view could help better modulate them.[94–96] From the atomic level, the introduction of one or more kinds of atoms in the vicinity of active sites can form new atomic interfaces. Such an atomic interface may tune the electronic configuration of the active sites and lead to new binding sites, modes, and different binding strengths with the intermediates. Besides, the interaction of catalysts with the substrate cannot be neglected when considering factors influencing catalytic activity. Previous research has disclosed that the selection of diverse substrates can affect selectivity through effective (but varied) interactions between the catalytic sites and the substrate.[76,77] The substrate can act as an electron sponge and help tune the valence state of the active sites, may stabilize the metal atoms and can facilitate the electron transfer to the catalytic moieties.[27] Research also indicates that the coordination environment of the active sites can affect the activity of catalysts.[90] Therefore, we will elaborate on the modulation of the atomic interface interactions from these three aspects: inter-atomic interface, coordination environment, and substrate (Fig. 4d–f).

2.3.1 Inter-atomic interface modulation. The introduction of additional metals in the vicinity of a single active site catalyst could lead to the creation of either a homo- or hetero-atom cluster catalyst that forms an inter-atomic interaction. This may bring in charge polarization, electronegativity difference, magnetic moment difference, *etc.*, which alters the electronic configuration of the catalysts and allow them to exhibit diverse selectivity and boosted activity than their counterpart SACs.

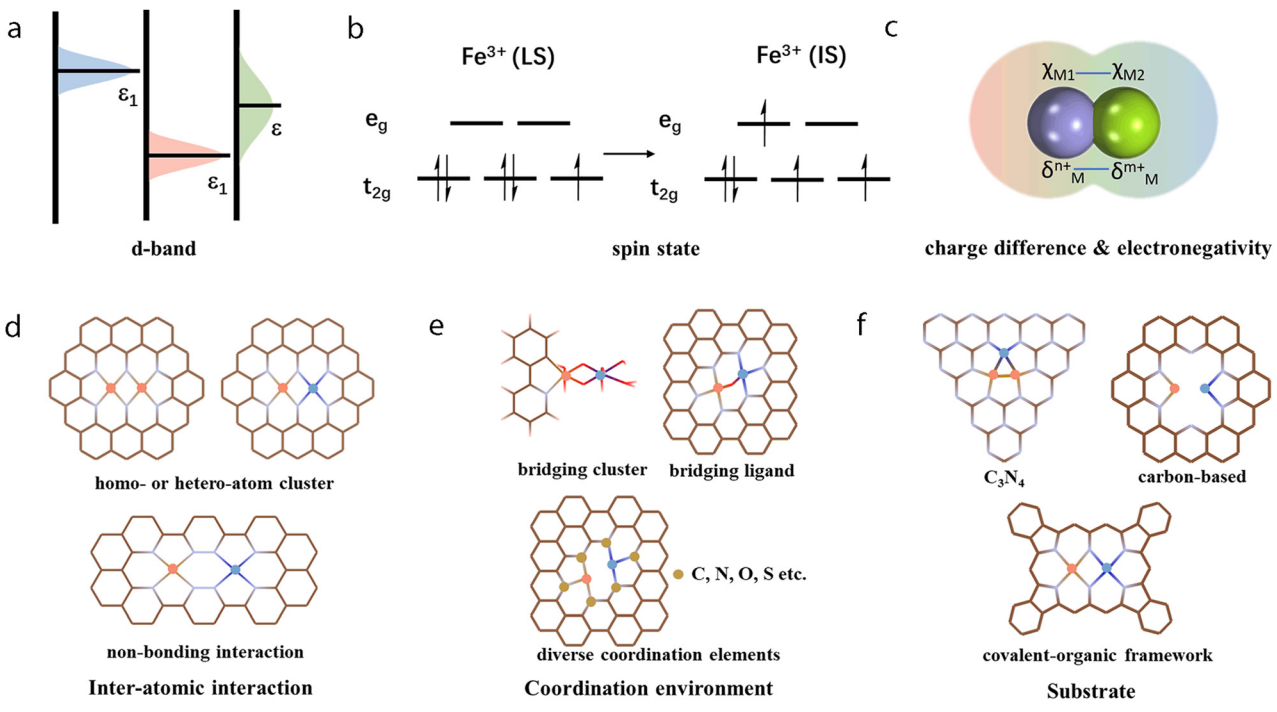

Fig. 4 The origin of synergistic effects in multi-atom cluster catalysts, including (a) d-band filling, (b) spin state, (c) charge difference and electronegativity. Modulation techniques, including (d) inter-atomic interaction, (e) coordination environment, (f) substrate.

We can regard such kind of design as inter-atomic interface modulation.

For instance, Sun's group identified with the help of DFT models that the use of metal dimers (Cu_2, MnCu, and NiCu) for CO_2RR could offer different selectivity. Cu_2 was found to be active for CO production, MnCu was promising for CH_4 generation, while NiCu yielded methanol.[97] Furthermore, a detailed inspection of metal dimers and single-atom catalysts for ORR by Hankel *et al.* found that CoPt@N_8V_4 was more promising for ORR than the others.[89] Besides, the DFT calculations disclosed a volcano correlation of onset potential with the free energy of the adsorbed hydroxyl intermediate, where the -OH group can be related to the spin moment change of cobalt atoms through d-orbital splitting. Thus, the introduction of the additional atoms could result in the tuning of d-orbitals and the reaction diversity of electrocatalysts. In addition, researchers recognized that the d-band center could also be used to evaluate the activity of multi-atom cluster catalysts. A systematic investigation of heteroatom metal dimers anchored on graphdiyne monolayers (FeM@ and NiM@GDY, M = Ti, V, Cr, Mn, Fe, Co, Ni, and Cu) for NRR suggested that FeCo@ and NiCo@GDY were suitable for NRR with HER suppression ability. This might have been due to the modulated d-band center by effective cooperation of the additional hetero-atom.[98]

2.3.2 Coordination environment modulation. It has already been demonstrated that the coordination environment is important for enhancement of performance during reactions.[99,100] It was found that the N/S coordination could promote activity during electrolysis.[101,102] The mediation of the coordination environment could help tune the geometric structure, leading to affected electronic configuration, shifting the d-band center, activating the adsorbed molecules, and thereby boosting the reaction activity. Therefore, Hunter *et al.* presented a series of models based on CoPt@N_xV_y, where x is the number of N atoms (N) in the model and y is the number of carbon atoms removed from a vacancy (V).[103] The HER ability of those materials could be enhanced by increasing N atom concentration, as the concentration of coordinated N atoms could affect the H atom adsorption ability. Similarly, through the detailed DFT calculations of hydroxyl group modified single metal atom and bi-metal atom catalysts anchored on graphene, for the electrocatalytic oxygen reaction in an alkaline medium, Zhao *et al.* found that the coordination with the hydroxyl groups could help improve OER and ORR activity.[104] Further, with the assistance of *in situ* Fe K-edge XANES spectra, it was found that the performance of $FeCoN_5$–OH climbed close to the apex of the ORR volcano plot with a moderate Fe–O binding energy. The reason is that the formation of triangular Fe–Co–OH configuration could help weaken the O–O bond and thus helped activate the oxygen molecule.[105] The co-adsorption of *H, *OH, and *CO and their influence on CO_2RR were also reported, where they can serve as good mediators for the CO_2RR, and decreased reaction barriers were obtained.[106]

2.3.3 Substrate modulation. The substrates selected for loading metal clusters are important as they should possess enough coordination sites to anchor the metal clusters with good stability, facilitate fast electron transfer between the substrate and the metal clusters, contain a large surface area to hold more catalytic sites, *etc.* For electrocatalysts, substrates such as graphene,[107] graphitic carbon nitride (C_3N_4, C_2N),[91,108] graphdiyne (GDY),[109] covalent–organic frameworks,[80,110] and other materials are regarded as good supports for metal clusters.[111,112] These substrates could affect the intrinsic catalytic activity of the metal clusters through effective interactions. As such, DFT calculations were used to analyze Fe_2 clusters anchored to defective graphene with pristine (C-DV/G) or porphyrin-like divacancy (N-DV/G), graphitic carbide nitride (g-C_3N_4), and graphdiyne (GDY).[75] It was found that g-C_3N_4 supported Fe_2 clusters had better activity towards NRR due to relatively small limiting potential than that of others. Furthermore, graphdiyne, as one kind of π-conjugated pure-carbon network with high electron conductivity and abundant π-bonds, was predicted to hold tetrahedral 3d transition metal clusters (TM_4). The well-built TM_4@GDY (TM = Sc, Ti, Mn, Fe, Co, Ni, and Cu) models were investigated for HER activity, where Fe_4@GDY and Co_4@GDY possessed higher HER activity.[72] It was found that such high activity might be due to the observed electron transfer rates from the TM_4 cluster to GDY, thus helping to activate the nearby C and TM atoms with optimized *H adsorption ability. The strong interactions between a substrate and metal clusters can potentially destroy the delocalized charge distribution of the latter and trigger an electron structure redistribution due to charge polarization. For instance, it was calculated that in the g-C_3N_4 supported tetrahedral Cu_4 cluster, charge transfer and orbital hybridization might occur between the pyridinic nitrogen atoms from the substrate and the bottom three Cu atoms.[108] Thus, a slightly oxidized Cu site might be obtained while the top Cu atom still remains at an almost zero valence. This non-symmetry between Cu^0 and Cu^{x+} species might promote the C–C coupling of two *CHO species and lead to the conversion of CO_2 to ethanol with a low limiting potential (0.68 V).

It is worth pointing out that the above-mentioned modulation of the materials should be regarded as a complex process of tuning the electrocatalysts. In most systems, electrocatalysts are not affected merely by one kind of effect, and therefore, multi-effects should be considered. One example that has been reported is for NRR, with an iron-based metal dimer anchored on graphene (Fe–TM_{DA}/GS, TM = Ti, V, Cr, Mn, Fe, Co, Ni, and Cu), where Fe–Ti_{DA}/GS had the highest NRR activity among them, with a limiting energy of 0.88 eV.[113] The DFT calculation results showed that an effective electron transfer might have resulted in moderate nitrogen adsorption for Fe–Ti_{DA}/GS, and the introduction of a second metal atom might have promoted the electron transfer between N_2 and the substrate, finally improving the catalytic activity of NRR. Another example is one using Fe–Co dual metal-doped N-coordinated graphene ($FeCoN_6$, $FeCoN_7$, and $FeCoN_8$) for ORR/OER.[43] It was reported that $FeCoN_7$ and $FeCoN_8$ were more promising for ORR/OER than $FeCoN_6$, and Co was found to be more active than Fe. However, the presence of Fe was also required as it could modify the electronic structure of the Co atom and helped

improve the binding behavior to the *O intermediate. Besides, the d-band center of the Co atom could be correlated with the ΔGO* of the intermediates during reactions for predicting the overpotential of such Fe–Co dual metal catalysts for ORR/OER.

3. The scaling relationship

Multi-atom cluster catalysts represent a new class of catalysts that combine the concept of single-atom catalysts and multiple atom clusters through the introduction of additional atoms to single-atom catalysts.[114–116] Either homo-nuclear or hetero-nuclear moieties can be constructed as multi-atom cluster catalysts by the selection of additional atoms.[117,118] Multiple active sites are beneficial for electrochemical reactions with a complex reaction path and intermediates possessing several binding sites. For example, in the electrochemical CO_2 reduction, several kinds of intermediates (*CHO, *COOH, *COH, *etc.*) including C-affinity and O-affinity sites can bind to multiple active sites of an electrocatalyst at the same time and lead to a different binding mode than that of SACs, which may help either lower the reaction barrier or change the reaction path, resulting in diverse selectivity and enhanced activity.[48,119,120] Such decoupling of the original scaling relationship also requires new descriptors, all of which have further been discussed below.

3.1 The origin of scaling relationship

In order to explore the most suitable materials for a certain reaction, one has to minimize the overpotentials (η) during reactions.[121] Researchers are able to predict η in electrocatalytic reactions by calculating the relative stability of adsorbed intermediates using the computational hydrogen electrode (CHE) model.[119,122] The rate-determining step energy, namely limiting potential (U_{lim}), calculated from the energy difference of adsorbed intermediates, is used as per the below equation to obtain η:

$$\eta = U_{eq} - U_{lim} \quad (2)$$

where U_{eq} is the equilibrium potential and could be regarded as a constant for a certain reaction. Therefore, the aim of smaller η could be turned into minimizing U_{lim}, or optimizing the binding strength of adsorbed intermediates.

Furthermore, the classical Sabatier principle suggests that the best catalysts should possess an optimum bond strength between the adsorbed species and surfaces, neither too weak to disfavor activation nor too strong to prevent the desorption of the adsorbed species.[123] Previous research has successfully established thermodynamic energy scaling relationships, generally linearly related, which can be used to correlate different adsorbed species across the reaction path for a series of catalyst surfaces.[124–126] One of the early examples was reported by Abild-Pedersen *et al.*, who suggested that the linear scaling relationships may exist for the intermediates of CH_x (x = 0, 1, 2, 3), NH_x (x = 0, 1, 2), OH_x (x = 0, 1), and SH_x (x = 0, 1) to that of C, O, N, and S atoms, respectively, during the reaction process.[127] In general, considering the adsorbates AH_x and the relevant A atom as a common expression, they assumed that A has an optimal electron density of n_0 with the contribution of both x hydrogen atoms and surface. From the bond order conservation view,[128] the surface contribution of electron density (n_{surf}) to A can be written as

$$n_{surf} = \frac{x_{max} - x}{x_{max}} n_0 \quad (3)$$

where x_{max} is the maximum amount of hydrogen that can bond with A and x is the real amount of hydrogen in AH_x. A further understanding of the adsorption energy between the surface and the adsorbate from the d-band model discloses a combined contribution of both the sp state and the d state, where the latter mainly contributes to the energy change ($\Delta E_d(x)$). Such energy change can be related to the below equation with the consideration of both second-order theory and effective medium theory:

$$\Delta E_d(x) \propto n_{surf} \propto \frac{x_{max} - x}{x_{max}} \quad (4)$$

Then, the scaling relation could be defined as

$$\Delta E_{AHx} = \gamma \Delta E_A + \xi \quad (5)$$

$$\gamma = \frac{x_{max} - x}{x_{max}} \quad (6)$$

Eqn (5) suggests that a linear relation of adsorption energy exists between adsorbates AHx and A (Fig. 5), where the slope γ is constant and can be obtained with the bond-counting rules and the intercept ξ is sensitive to different coordination environments. According to eqn (6), the slope between adsorbate OH and O is 0.5 when considering that x_{max} for the O atom is 2, while the slope between CH_3, CH_2, CH, and C is 0.25, 0.5, and 0.75, respectively, when considering that x_{max} for C is 4. This can explain well the trend found by Abild-Pedersen *et al.* The concept of scaling relationships can be further extended to other systems with complex intermediates.[129–131] For instance, the scaling relation of ΔG(*OOH) = ΔG(*OH) + 3.2 eV was found to explain the OER/ORR trend for the surface of low index metals, alloys, metal oxides, *etc.*[132] The scaling relationships also exist in electrocatalytic CO_2 reduction, where the adsorption energy of E_b(*CHO) = 0.88E_b(*CO) + 2.03 eV, E_b(*COOH) = 0.73E_b(*CO) + 1.82 eV, E_b(*CH_2O) = 0.54 E_b(*CO) + 0.25 eV, *etc.* can be found.[45] Furthermore, the combination of the linear relations with the Brønsted–Evans–Polanyi (BEP) correlations of activation energy and reaction energy for surface reactions can be used to establish the full potential energy diagram for a certain reaction, which can predict the maximum reaction rates and screen promising catalysts.[133]

3.2 The limitation and breaking of the scaling relationship

The combination of scaling relationships and CHE models can facilitate the prediction of optimal electrocatalysts for certain electrocatalytic reactions with fewer independent variables to be considered. However, these relationships inevitably impose a thermodynamic limitation on the catalysts to be predicted.

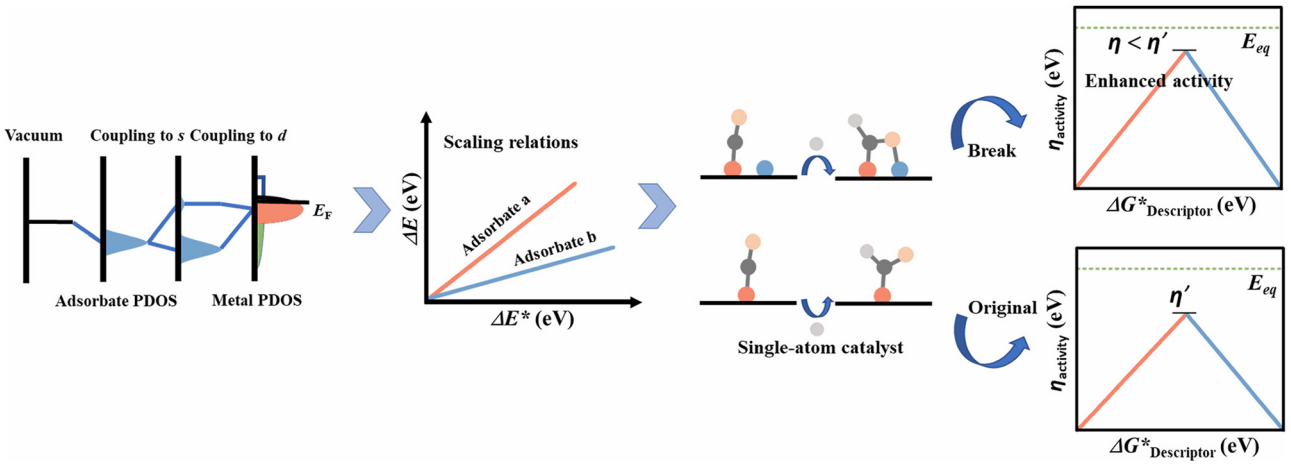

Fig. 5 Illustration of the interaction between the adsorbate and the surface of the electrocatalyst to form the linear relations and to break such relations during a reaction (the left figure was replotted with permission,[148] Copyright 2008 Elsevier).

For reactions with complex reaction intermediates of the same central atom, like that in CO_2RR, it is hard to circumvent the relationship by strengthening the adsorption energy of one kind of intermediate. For example, the strengthening of adsorption energy for *CHO would weaken it for the other (*e.g.* *CO) due to the linear relationship between them.[134,135] Similarly, in the ORR, the scaling relationships exist between intermediates *O, *OOH, and *OH. The apex points of the volcano curves represent a maximum limiting potential of around 0.86 V. As the equilibrium potential for each elementary step is 1.23 V with a linear relation of ΔG(*OOH) = ΔG(*OH) + 3.2 eV, the minimum η is calculated to be 0.37 V from equation 2.[121] However, if the adsorbing species could interact with a surface carrying various kinds of active sites, it may allow circumventing the scaling relationships.[5,134,136–140] Jiang *et al.* established a new relation of ΔG(*OOH) = ΔG(*OH) + 2.41 eV with dual active site models, which is very close to the ideal linear relation of ΔG(*OOH) = ΔG(*OH) + 2.46 eV.[70] The new relation could provide a maximum limiting potential of around 1.04 V and proved the possibility of using multi-atom clusters to break the scaling relationships.

For multi-atom cluster catalysts, the introduction of additional atoms to form multi-active sites may decouple the inherent scaling relationships.[73,141–143] This strategy is quite useful for reactions that involve complex reaction paths.[70,109,144] An example was reported by Wang *et al.* in the context of CO_2RR, wherein they established models containing twenty-one kinds of heteronuclear transition metal dimers embedded in a C_2N substrate.[48] Through the calculations, they found that both the metal atoms could bind with the adsorbed species through oxygen and carbon sites. This resulted in the decoupling of E_b(*CO) *versus* E_b(*CHO) and E_b(*CO) *versus* E_b(*COOH) from the original scaling relationship. Therefore, the free energy profiles obtained showed that both CuCr/C_2N and CuMn/C_2N could produce CH_4 with limiting potentials as low as −0.37 V and −0.32 V, respectively. These results proved the efficiency improvement as a result of introducing multi-active sites which helped in circumventing the original scaling relationships to obtain complex products with high activity.

3.3 Descriptor

The electrochemical reactions are usually multi-step processes accompanied by multiple electron–proton transfers. During a reaction, the interaction of adsorbed species with the surface of a catalyst may lead to diverse binding strength on different catalysts, which results in complex reaction pathways and the production of diverse products. To selectively control the production of desired products through a certain reaction pathway with high activity, one has to screen for the most suitable catalysts, which is usually tedious and laborious. Thus, it will be helpful if key parameters could be identified and help reduce the complexity of grouping the reactions and guide a rational catalyst design strategy with the assistance of techniques such as DFT calculations, and also with the newly emerging machine learning technique.[132,145] In this regard, the descriptors mentioned in the previous section could help provide a catalyst design strategy by elucidating the activity trends and hence unraveling the most promising catalysts.

So far, the successful application of a descriptor for this purpose has been exemplified in the use of the binding energy of adsorbed species *O and *OH as a descriptor $(\Delta G_{*O} - \Delta G_{*OH})$ for disclosing the activity trend of OER/ORR reactions.[132,146,147] However, it is hard to regard it as a universal principle to predict new series of catalysts as it is still ambiguous about the intrinsic factors of the catalysts that govern the binding strength of adsorbates in a simple adsorption–activity relationship. Therefore, it is necessary to identify the real intrinsic characteristics of the catalysts to help establish a more universal descriptor that can help adjust the adsorption behavior of adsorbates, in turn affecting the activity.[148] Some progress has been achieved for electrocatalysts, where the d-band center,[149–152] p-band center,[153] e_g occupancy,[125,154] surface distortion,[155] coordinative unsaturated metal cation,[156] electronegativity,[126] *etc.*, have been adopted to elaborate on these relationships.

Nevertheless, none of these descriptors hold promise to represent a universal descriptor to disclose the intrinsic feature of diverse catalysts. Therefore, in the development of multi-atom cluster catalysts, specific descriptors should be built for a better adjustment of the adsorption energies of intermediates and the activity of such catalysts.[98,157]

Wu's group developed a series of homonuclear (M_2, M = Mn–Cu) and heteronuclear (FeM, M = Mn–Cu) nitrogen co-doped binuclear transition metal models for ORR, apart from developing a linear relationship between the overpotential and electronegativity difference. They also developed descriptors based on free energies (ΔG_{*O} and ΔG_{*OH}) and d band center to screen these catalysts. $FeCoN_6$-Gra turned out to be the most promising one, which coincided with the experimental results.[92] Similar descriptors can also be used for the NRR with the use of two-dimensional bi-atom catalysts, where the adsorption energy of *H and $*N_2H$ can be used as a suitable descriptor.[158] The above descriptor is commonly used in diverse electrocatalytic systems, yet it has the limitation to cover all kinds of catalysts.[159] Specific descriptors considering the parameters mentioned in the above section to screen efficient multi-atom cluster catalysts effectively are still waiting to be developed. These descriptors, including the ones based on the N_2 polarization charge for NRR by Zhao's group and the dissociative chemisorption energy of water to depict HER by Qiao's group, could help the rational design of multi-atom cluster catalysts.[160,161] However, as those descriptors can help correlate the intrinsic feature of catalysts to the activity and selectivity among a series of catalysts, the use of more accurate and universal descriptors is crucial in assisting the experimental screening of optimized multi-atom cluster catalysts and is worth more endeavors.[162]

4. Preparation method of multi-atom cluster catalysts

To better utilize the resulted synergistic effects in electrocatalysis, it is necessary to prepare multi-atom cluster catalysts with precise structural characteristics, and this requires researchers to develop novel and rational strategies. However, accurate control over the synthesis of a given homo- or hetero-composition for multi-atom cluster catalysts remains more challenging than the well-developed top-down and bottom-up synthesis strategies of SACs. The metal atoms also tend to aggregate to form nanoparticles or decompose to single atoms during the synthesis process. It would be of utmost importance to find out rational ways that facilitate the formation of multi-atom cluster catalysts without any unwanted structures. To date, various strategies, such as precursor preselection, spatial confinement–pyrolysis, coordination stabilization, and electrochemical strategies, atomic layer deposition method, and some other methods (electrospinning, ball-milling, mass-selected soft landing, *etc.*) have been reported to prepare multi-atom cluster catalysts and are discussed below (Fig. 6).

4.1 Precursor preselection strategy

The precursor preselection method can anchor metal clusters (such as metal complexes) of either homo- or hetero-atoms with desired atom numbers onto a substrate (oxides, graphene, *etc.*).[163] Such precursors possess characteristic metal clusters protected by a chelating ligand, which can help hamper the aggregation or decomposition of the metal clusters. Subsequent pyrolysis ensures the formation of multi-atom cluster catalysts on the substrate with retained cluster structure and composition. Using this strategy, Li *et al.* reported the use of bis(dicarbonyl-cyclopentadienyl iron) ($Fe_2O_4C_{14}H_{10}$) as a precursor, which was then dispersed on mpg-C_3N_4.[37] Careful pyrolysis under a 5% H_2/Ar atmosphere at 300 °C finally gave Fe_2/mpg-C_3N_4. The precursor preselection method was also used to prepare a series of tunable Fe clusters using $Fe(acac)_2$, $Fe_2(CO)_9$, and $Fe_3(CO)_{12}$, which were encapsulated in ZIF-8 to prepare Fe–N–C, Fe_2–N–C, and Fe_3–N–C respectively.[164] Later, trinuclear Fe_3, Fe_2Zn, and Fe_2Co were reported to be post-impregnated into [Zn(BPB)]·guest (AIST-1) for the preparation of Fe_3-NPs/GNCL, Fe_2-GNCL, and Fe_2/Co_1-GNCL with isolated Fe_2 and Co sites on the substrate.[165] Recently, Yao *et al.* reported that using $Ni_2(dppm)_2Cl_3$ (dppm = bis(diphenylphosphino)methane) as the precursor, further encapsulation and pyrolysis in MOFs could produce a Ni_2/NC dual-site material.[166] The precursor preselection method turned out to be a convenient method in terms of both the availability of precursors and the ease of operation for the preparation of multi-atom cluster catalysts. Although there are already some examples available for preparing the homo-clusters with such a method, the demand for the synthesis of hetero-clusters still calls for more endeavors due to the lack of suitable precursors.

4.2 Spatial confinement–pyrolysis strategy

The spatial confinement–pyrolysis method is widely used as an effective tool for the synthesis of atomic-scale materials. Considering that mere impregnation may cause the formation of isolated SACs or give rise to nanoparticle impurities rather than multi-atom cluster catalysts, the encapsulation of metal precursors in spatially confined porous materials such as metal–organic frameworks (MOFs) or covalent–organic frameworks (COFs) can prevent the sintering of precursors during the subsequent pyrolysis.[160,161] Several paths of using the spatial confinement method are listed. In the first example, Wang *et al.* developed a Zn/Co bimetallic MOF by using metal-organic frameworks as a confined space. Then, such a porous material could be used as a host to capture the second element of iron salt in the cavities.[45] During the pyrolysis process, the Zn^{2+} ions get reduced by the as-generated carbon and are vaporized due to the relatively low boiling point of Zn, while the Fe^{3+} moieties are reduced and get connected with the cobalt atoms in their vicinity to form the DAC Fe–Co structure. This atomic phase transformation could be traced through HAADF-STEM images and was proved with EXAFS fitting. Another example is the use of as-prepared CoNi-MOFs to fabricate a Co–Ni DAC.[167] The CoNi-MOFs with two different metal elements could be prepared from chemical co-precipitation of Ni salt and $Co(CN)_6^{3-}$ during the synthesis. After being coated with dopamine during the self-polymerization process, the material was carbonized with NH_3 at 500 °C to obtain CoNi–NPs/NC. The nanoparticles

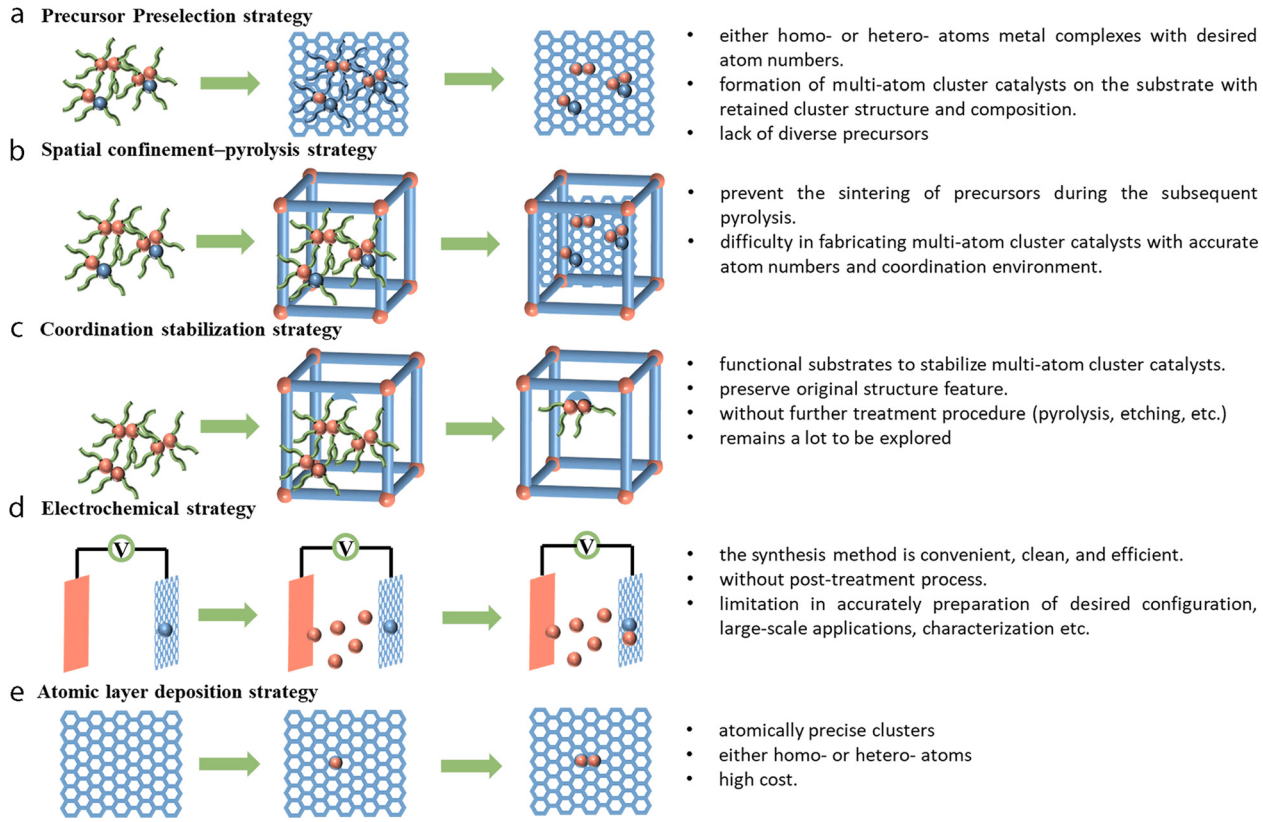

Fig. 6 (a) Precursor preselection strategy. (b) Spatial confinement-pyrolysis strategy. (c) Coordination stabilization strategy. (d) Electrochemical route strategy. (e) Atomic layer deposition strategy.

were then removed by acid leaching to obtain CoNi-SAs/NC. It is worth noting that the above two paths still lack precise control in obtaining multi-atom custers with designated structures, and the spatial confinement method to encapsulate precursors within well-defined structures could potentially offer better control of the composition. One example was reported by Ji *et al.*, where $Ru_3(CO)_{12}$ was dispersed in the cages of ZIF-8 through one-pot synthesis wherein the as-prepared $Ru_3(CO)_{12}$@ZIF-8 decomposed to uniformly dispersed Ru_3 clusters upon heat treatment.[38] The method of spatial confinement is much easier to adapt to fabricate multi-atom cluster catalysts. However, as mentioned, an arbitrary combination of different elements to form clusters with an accurate multi-atom cluster structure and coordination environment remains difficult for such techniques; thus it is better if smart precursors with well-defined structures could be utilized.

4.3 Coordination stabilization strategy

In the spatial confinement–pyrolysis strategy, it is necessary to overcome the high surface energy and anchor the clusters to the substrate by pyrolysis treatment. However, multi-atom clusters can also be stabilized directly by strong surrounding coordination sites to overcome their high surface energy.[168,169] Therefore, substrates possessing coordination sites, such as MOFs, COFs, organic ligands, functional carbon substrates, *etc.*, could be used to prepare multi-atom cluster catalysts.[170] For instance, a series of crystalline trinuclear copper clusters were prepared by Lan *et al.* through solvothermal reaction using copper halides, imidazole, and pyrazole, where their precise structural features were verified from the single-crystal diffraction analysis.[170] From the result, the $Cu_3(\mu_3\text{-OH})$ core was stabilized by equatorial bridging pyrazole ligands, and the remaining square-planar vacancy of copper was coordinated by the imidazole ligand. Another example was reported by Duan *et al.* with the use of graphdiyne (GDY) to stabilize copper nanoclusters.[171] The triple bond of graphdiyne made it behave as an electron-donating substrate for immobilized copper atoms. The uniform pore of graphdiyne rendered it the ability to confine the size of metal clusters and enhance its interaction with electrolytes. The use of ligands to stabilize the metal clusters was reported by Li *et al.*,[172] where the co-facial dual palladium complex, $\{cis\text{-}[(2,2'\text{-bipyridine})\text{palladium(II)}]_2(\mu\text{-}1,3\text{-}NO_3)_2\}$ core, could be precipitated onto acetylene black to prepare the Pd_2 catalysts. Here, each palladium atom was coordinated by a 2,2′-bipyridine ligand. The bidentate nitrate in the complex helps to chelate and bridge two palladium atoms to form the co-facial arrangement. In summary, the method of coordination stabilization strategy could prepare multi-atom clusters without further treatment procedures (pyrolysis, etching, *etc.*) and thus can preserve the original structure feature. This may help to build a precise moiety model to investigate the reaction mechanism and such a strategy remains to be explored a lot.

4.4 Electrochemical strategy

The electrochemical route could be regarded as convenient, clean, and efficient for producing multi-atom cluster catalysts without the post-treatment process.[173] For instance, through the electrochemical leaching, segregation, and deposition process, the atoms may be etched and dealloyed gradually from one electrode and migrate through the electrolyte to deposit onto the other electrode under an applied voltage. The electrochemical potential for leaching an element from the bulk materials can be overcome by operating at a suitably applied voltage. Experimentally, such a method was reported for the synthesis of SACs and can be extended for the synthesis of multi-atom clusters.[174] Theoretically, Liu *et al.* investigated the feasibility and universality of such a strategy to prepare a series of materials using oxides, graphene, and graphdiyne as substrates with a different atomic scale of the catalysts (ranging from SACs to MACs).[175,176] Zhang *et al.* prepared a Co–Pt DAC (A–CoPt–NC) with this method to prepare multi-atom cluster catalysts.[177,178] The as-prepared Co-MOF was first pyrolyzed to form cobalt nanoparticles (Co-NC), and then the Co-NC were drop-cast onto a glassy carbon electrode and with the subsequent long-term cyclic voltammetry activation (0.1 to 1.1 V *vs.* RHE, 8000 cycles) of the sample with Pt wire as a counter electrode, A–CoPt–NC could be prepared by slow segregation and deposition of Pt on to the glassy carbon electrode. Cyclic voltammetry scanning can also be used to deposit metal ions directly from the electrolyte or form clusters. One such example has been reported by Wang *et al.*, where the sulfur atom decorated graphene oxide (HG) was used to chelate $Ni(acac)_2$ to form HG–Ni.[179] Then the as-prepared HG–Ni was drop-cast onto a glassy carbon electrode (GCE) followed by the cyclic voltammetry scanning of pristine HG–Ni/GCE with $FeCl_3$ in the electrolyte to form a pristine HG–NiFe dual-site. All these electrochemical methods can be extended to fabricate materials with different substrates, but limitations still exist when faced with the accurate synthesis of desired configuration, large-scale synthesis, characterization, *etc.*

4.5 Atomic layer deposition strategy

Atomic layer deposition (ALD) can be used for the deposition of noble metals or metal oxides to form atomically precise clusters with the use of gas-phase precursors, and this method allows the preparation of atomically precise clusters of either homo- or hetero-atoms. Yan *et al.* reported the preparation of oxidized Pt_2 dimers on graphene for hydrolytic dehydrogenation of ammonia borane.[180] A first dose of precursor trimethyl(methylcyclopentadienyl)-platinum(IV) ($MeCpPtMe_3$) was introduced. Then the self-limiting surface reaction between graphene and $MeCpPtMe_3$ followed by subsequent exposure to O_2 at 250 °C helped to form Pt_1/graphene. The next reaction of Pt_1 single atoms as nucleation sites with $MeCpPtMe_3$ at 150 °C helped to form Pt_2/graphene without any metal aggregation. The subsequent exposure of samples to ozone successfully removed the ligand to form oxidized Pt_2O_x, which exhibited a much higher specific rate of 2800 mol_{H_2} mol_{Pt}^{-1} min^{-1} for hydrolytic dehydrogenation of ammonia borane. This was around 17- and 45-fold higher than that of the Pt SAC and nanoparticles on graphene, respectively. The ALD technique calls for a stable interaction between the substrates and the precursors and the precursors should be easy to evaporate and anchor onto the substrates. The subsequent removal of protective ligands to obtain catalysts requires researchers to find relatively cheap sacrificial precursors to reduce the cost.

4.5 Other strategies

The techniques of electrospinning,[181] ball-milling,[182] soft template-directed interlayer confinement,[183] mass-selected soft landing,[33] *etc.* are also promising for preparing multi-atom cluster catalysts. For instance, Fu *et al.* reported using Fe, Co-Phen, polyacrylonitrile (PAN), and ZnO nanoparticles as precursors for the preparation of nanofibers by the electrospinning technique.[184] The ZnO introduced could be reduced and evaporated during the subsequent pyrolysis process to create numerous hollow pores. These hollow pores could combine with the nanofibers prepared through the electrospinning technique to increase the total metal loading to about 9.8 wt%. The ball-milling method is capable of kilogram-scale synthesis of materials,[182,185] and as such, M_2/N-C (M_2 = Ni, Co) and Fe_1M_1/N-C (M_1 = Pd, Ni) were prepared and used for the reverse water–gas shift (r-WGS) reactions with the ball-milling method.[163] The technique of using soft and reactive landing of mass-selected ions to deposit them onto the surfaces turns out to be a powerful tool due to its ability to accurately control the synthesis of catalysts with selected element species, cluster size, and total charge. This technique can be used to build more accurate and reliable catalytic models, which can help gain insights into the nature of the catalytic reactions.[33] For instance, Let *et al.* reported that Ag_n (n = 2 to 4) clusters go through a quadrupole mass filter and deflector assembly and are then deposited on the oxide supports.[186] Similarly, as-generated Cu_4 clusters in Al_2O_3 thin film exhibited CO_2 hydrogenation to methanol at both high and low CO_2 partial pressures.[34] However, this method is of both high cost and low yield, thus limiting its practical application.

The preparation methods summarized above can complement each other in the fabrication of multi-atom cluster catalysts. So far, most of the methods developed are not universal and there is a high demand for the development of new strategies that can be used to prepare arbitrary and precise homo- or hetero-clusters. This can be regarded as a vital and fundamental requirement for the further study of the structure–activity relationship.[187]

5. Advanced characterization methods of multi-atom cluster catalysts

The successful preparation of multi-atom cluster catalysts should be confirmed using advanced characterization methods.[25] Besides, verifying the existence of effective synergistic effects through observing their physical and chemical properties, such

as the electronic state, coordination environment, morphology, the possible single-crystal structure, *etc.*, is also necessary.[188] Furthermore, monitoring the reaction kinetics (coordination environment, geometric structure, valence state, electronic structure, intermediate, adsorbate, *etc.*) during the catalytic process with multi-atom cluster catalysts with advanced characterization techniques is also necessary.[189] This may deepen the comprehensive understanding of intrinsic features of these materials, facilitate their mechanistic investigation, and thus help to develop advanced electrocatalysts.

5.1 Structure characterization

Considering that the amount of multi-atom cluster catalysts loaded on the substrate is usually quite small, only highly sensitive techniques can be used for their characterization. To date, the following characterization techniques such as scanning transmission electron microscopy (STEM),[190,191] X-ray absorption spectroscopy (XAS),[192,193] single-crystal X-ray diffraction (SC-XRD),[194] X-ray photoelectron spectroscopy (XPS),[195] *etc.*, are commonly used to probe the structure information of multi-atom cluster catalysts.

5.1.1 HAADF-STEM. Aberration-corrected high-angle annular dark-field scanning TEM (HAADF-STEM) with atomic resolution is one kind of advanced technology capable of rendering the imaging and spectroscopic information at the atomic level.[190] As transition metals with larger atomic numbers usually exhibit brighter dots than lighter elements (usually carbon, nitrogen, oxygen, *etc.*), HAADF-STEM can be used to visualize the distance of neighboring multi-atom clusters directly, thus verifying their possibility to cooperate with each other through effective interaction. For instance, Zhang *et al.* carried out HAADF-STEM to observe dual-site Ni-CNC, where the bright dots were resolved as Ni atoms and the distance of neighboring Ni atoms was about 2.5 Å (Fig. 7a and b).[181] This indicates that a possible interaction could be obtained between adjacent Ni atoms for electrocatalysis, which was supported by both the improved activity for CO_2 reduction and the DFT calculation of the modulated d-band center. In addition, the composition information of the multi-atom clusters can be further obtained with electron energy loss spectroscopy (EELS) (Fig. 7c–e).[191] Although HAADF-STEM and EELS can provide direct information of materials, they also have difficulty in distinguishing elements possessing similar atomic numbers at the atomic level. Meanwhile, the STEM image only provides a two-dimensional projection, rather than special information of materials. Finally, the coordination species, such as metal–carbon and metal–oxygen bonds, could not be discerned from STEM.

5.1.2 XAS. The synchrotron X-ray absorption spectroscopy technique is a powerful tool to provide a more detailed local environment and electronic structure of multi-atom cluster catalysts, thus serving as one essential tool to confirm the structure of multi-atom cluster catalysts and analyze the synergistic interaction of such structures.[192] In detail, the X-ray absorption near edge structure (XANES) can be used as a fingerprint peak to disclose the spatial arrangement, valence state, d-band occupancy of the probed atom, etc, whereas the extended X-ray absorption fine structure (EXAFS) can be used to obtain the coordination number, coordination atoms, and distances. Then the atomic structure of multi-atom cluster catalysts and the possible electronic structure could be obtained with reference to the XANES and EXAFS results. In Chen *et al.*'s work,[193] XANES and EXAFS were combined with each other to confirm the configuration, valence state, and coordination of IrCo–N–C. The Co K-edge XANES spectrum of IrCo–N–C suggested the coexistence of an asymmetric diatomic structure with a D_{4h} symmetric Co-N4 configuration (Fig. 7f). From the Co K-edge XANES spectra, the valence state of Co from IrCo–N–C is slightly lower than that of Co–N–C. Besides, the valence state

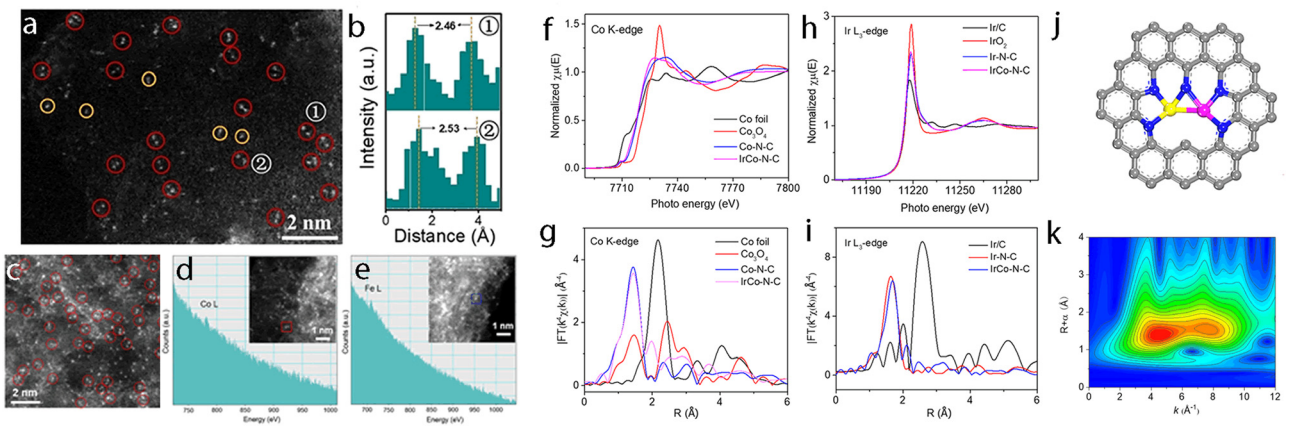

Fig. 7 (a) HAADF-STEM image and (b) the corresponding intensity profile of Ni-CNC-1000. Reproduced with permission.[181] Copyright 2021 John Wiley & Sons. (c) Aberration-corrected HAADF-STEM image. The dashed circles highlight the paired bright spots. (d) Cobalt element and (e) Iron element identification with EELS analysis of the selected paired spot and single spot in the inset HAADF-STEM images of Co2/Fe–N@CHC. Reproduced with permission.[191] Copyright 2022 John Wiley & Sons. (f) Co K-edge XANES spectra. (g) Fourier transform of extended X-ray adsorption fine structure (FT-EXAFS) spectra of Co K-edge. (h) Ir L_3-edge XANES spectra. (i) Fourier transform of extended X-ray adsorption fine structure (FT-EXAFS) spectra of Ir L_3-edge. (j) Illustration of the structure of the IrCo–N–C catalyst. (k) WT of the Ir L_3-edge for IrCo–N–C. Reproduced with permission.[193] Copyright 2021 American Chemical Society.

of Ir from IrCo–N–C in the Ir L-edge XANES measurement indicated a slightly higher valence state of Ir than that of Ir–Co–C (Fig. 7h). This suggested a charge transfer from Ir to Co due to the electronegativity difference between them. From the Fourier transform of extended X-ray absorption fine structure (FT-EXAFS) and the R space fitting result, it is found that the coordination number of Co–N and Ir–N in IrCo–N–C is *ca.* 3.3 and 3.0, respectively (Fig. 7j-i). The Ir–Co path was also presented, which was further confirmed using EXAFS wavelet transform (WT) analysis, thus assuring the diatomic Ir–Co configuration (Fig. 7k). However, the XAS result is an average analysis of the data collected, which means the synthesized structure should be uniform and precise. Besides, the XAS result reflects merely the bulk information and the electrocatalysis usually occurs on the surface of active sites, and thus it is necessary to consider this information when analyzing the electrocatalytically active sites. Finally, most multi-atom clusters can form metal–carbon and metal–nitrogen bonds, while XAS has difficulty discerning each other.

5.1.3 Other characterization techniques. The above mentioned techniques of HAADF-STEM and XAS are regarded as the most powerful tools that combine with each other to resolve the environment and electronic structure of multi-atom cluster catalysts and indicate the existence of possible interactions. Apart from them, other techniques available for capturing the environment and electronic structure are also indicated here. For instance, the single-crystal X-ray diffraction (SC-XRD) technique has been widely used as a non-destructive tool to determine the structure of high-quality single-crystalline materials.[170,194] The data collected can be solved and refined to obtain the structural information including unit information, bond lengths, bond angles, *etc.* For multi-atom clusters derived from well-grown MOFs and organic ligands one could adopt the SC-XRD method to obtain their structural information. The X-ray photoelectron spectroscopy (XPS) technique can be another useful tool to capture the composition and oxidation states of probed species,[195] and validate the existence of electron transfer behaviours for multi-atom cluster catalysts. The techniques capable of obtaining environmental and electronic information and the effective interaction of multi-atom cluster catalysts are not limited to the above-mentioned techniques. For instance, the electron paramagnetic resonance (EPR) technique is highly sensitive to unpaired electrons and thus is promising for determining the orbital occupations of transition metals.[196] Mössbauer spectroscopy can be used to differentiate the valence state, coordination, and electronic structures.[87] There are increasing efforts in employing them for multi-atom clusters. The characterization techniques summarized above could help establish a good understanding of the materials, and the results could be combined with theoretical models to deepen the mechanistic investigation. Yet these measurements are operated without *in situ* considerations. It will be better if *in situ*/operando techniques were used to capture the signals during reactions, thus obtaining more accurate kinetic structure evolution and valence state change, finding out the possible reaction intermediates, understanding the key role of interaction-induced synergistic effects in multi-atom cluster catalysts, and finally guiding the future design of promising catalysts. Therefore, the *in situ*/operando measurements on multi-atom cluster catalysts will be discussed below.[197]

5.2 Electrocatalytic process evolution

The real-time characterization techniques are also indispensable for observing catalytic processes on multi-atom cluster catalysts.[188,189] So far, several *in situ*/operando techniques have been explored, including Raman spectroscopy, Fourier transform infrared spectroscopy, XAS (XANEs and EXAFS), *etc.*[198] By observing the coordination environment and geometric structure evolution, valence state and electronic structure comparison, and intermediate and adsorbate identification, opportunities could be identified to observe the local active sites and the reaction mechanisms. A brief introduction will be given in this section and a further discussion is provided in Section 7 (Tables 1–5).

5.2.1 Coordination environment and geometric structure evolution. Though STEM can reveal atomic scale images directly, the real-time observation at the atomic scale level in liquid electrocatalytic conditions is still difficult and calls for endeavors.[199] Thus, XANES, EXAFS, Raman spectroscopy, *etc.*, are used for real-time observation of the catalytic process of multi-atom cluster catalysts. XANES and EXAFS could be combined to provide the dynamic behaviors of the coordination environment, and structural reconstruction information during reactions.[200,201] Raman spectroscopy is also promising to check

Table 1 Summary of multi-atom cluster catalysts for electrocatalytic HER

Catalysts	Metal content (ICP/XPS, wt%)	M–M distance (STEM/XAS, Å)	Electrolyte	Overpotential at 10 mA cm^{-2} (mV)	Tafel slope (mV dec^{-1})	Ref.
Pt–Ru dimer on NCNTs	Pt 0.9, Ru 0.31/—	2.4 ± 0.4/2.34 ± 0.04	0.5 M H_2SO_4	~20	28.9	47
A–CoPt–NC	—	3.4/—	0.5 M H_2SO_4/1 M KOH	27/50	31/48	178
Pd/Cu–Pt NRs	—	—/2.64	0.5 M H_2SO_4	22.8	25	210
Pt_1@Fe–N–C	Pt 2.1, Fe 1.0/—	3.0/—	0.5 M H_2SO_4	60	42	211
Fe–Rh SAs	—/Rh 1.1, Fe 1.8	—/2.59 ± 0.02_{Fe-Fe}, 2.59 ± 0.04_{Rh-Fe}	0.5 M H_2SO_4	36	26	212
NiCo–SAD–NC	Ni 3.719, Co 3.331/—	2.41 ± 0.24/2.55	0.5 M H_2SO_4/1 M KOH	54.7/61	31.5/55	213
W_1Mo_1–NG DAC	W 6.82, Mo 1.02/—	3.0–3.6/3.29	0.5 M H_2SO_4/1 M KOH	24/67	30/45	214

Table 2 Summary of multi-atom cluster catalysts for electrocatalytic ORR

Catalysts	Metal content (ICP/XPS, wt%)	M–M distance (STEM/XAS, Å)	Electrolyte	Half-wave potential (V *vs.* RHE)	Onset potential (V *vs.* RHE)	Limiting current density (mA cm^{-2})$_{1600\ rpm}$	Tafel slope (mV dec^{-1})	Specific activity (mA cm^{-2})	Ref.
(Fe,Co)/N-C	Fe 0.93, Co 1.17/—	—/2.25	0.1 M $HClO_4$	0.863	1.06	~5.7	66	2.842 (0.90 V)	45
$Ni_{66}Fe_{34}$–NC	Fe 0.29, Ni 0.14/—	—/2.35–2.51	0.1 M KOH	0.85	—	~5.6	107	—	49
Co_2N_5/Co NP	Co 4.3/Co 1.06	2.11–2.12/2.12	0.1 M $HClO_4$	0.79	0.92	~6.0	55.8	—	64
FeNi–N_6–C	Fe 1.448, Ni 1.472/—	—	0.1 M $HClO_4$	~0.8	—	~5.2	—	—	66
Fe–NiNC-50	Fe 0.33, Ni 0.57/—	1.8/2.43	0.1 M KOH	0.85	~1.0	~7.0	55	—	67
FeCo-IA/NC (X60-900)	Fe 0.26, Co 1.06/—	—	0.1 M KOH	0.88	0.98	~6.5	97	—	70
(Zn,Co)/NSC	—/Zn 0.13, Co 0.26	2.64 ± 0.2/—	0.1 M KOH	0.893	1.07	~5.3	50	—	101
FeCoNx/C	—/Fe 1.06, Co 1.12	2.2–2.3/2.1–2.2	0.1 M $HClO_4$	0.86	1.02	~5.7	47.9	16.07 (0.80 V)	105
Fe_2–N–C	Fe 0.38/—	—/2.60	0.5 M H_2SO_4/ 0.1 M KOH	0.78/0.905	—	~5.7/	83/—	16.4 (0.75 V)	164
Fe_2/Co_1-GNCL	—/Fe 0.48, Co 0.19	$2.6_{Fe–Fe}$/$2.6896_{Fe–Fe}$	0.1 M KOH	0.846	—	~5.8	—	—	165
CoNi-SAs/NC	—	—/2.22	0.1 M KOH	0.76	0.88	4.95	—	23.2 (0.50 V)	167
(Fe,Co)/CNT	Fe 1.21, Co 1.13/—	—/2.22	0.1 M KOH	0.954	1.15	5.5	—	17.51 (0.90 V)	175
a(Co–Pt)@N8V4	Co 1.72, Pt 0.16/—	—/2.5–2.9	0.1 M KOH	0.96	—	5.7	—	1.41(0.90 V)	177
Fe,Co SAs-PNCF	Co 4.32, Fe 5.48/—	~2.30/2.37–2.55	0.1 M $HClO_4$/ 0.1 M KOH	0.78/0.93	0.94/1.04	~5.8/~6.2	126/77	—	184
Co_2/Fe–N@CHC	Co 2.13, Fe 0.98/ Co 1.94, Fe 0.85	$6.3–7.6_{Fe–Co}$/ $5.3–8.8_{Fe–Co}$, $2.41_{Co–Co}$	0.1 M $HClO_4$/ 0.1 M KOH	0.812/0.915	—	~5.8	73/62	8.36/9.44 (0.80 V)	191
IrCo−N−C	Ir 0.18, Co 1.02/—	~2.30/~2.30	0.1 M KOH	0.911	1.00	~4.4	54	29.73 (0.85 V)	193
Pt_1@Fe−N−C	Pt 2.1, Fe 1.0/—	3.0/—	0.5 M H_2SO_4	0.80	0.93	~6.3	—	—	211
M/FeCo-SAs-N-C	Fe 3.32, Co 3.33/ Fe 5.12, Co 4.39	—/$2.52_{Fe–Fe}$	0.1 M $HClO_4$	0.851	0.981	~4.8	83	32.04 (0.80 V)	215
AC@f-$FeCoNC_{900}$	—/Fe 0.53, Co 0.54	—/2.55	0.1 M KOH	0.89	1.05	5.75	—	—	216
(Au-Co) DP-NPAs	Au 1.18, Co 3.48/ Au 1.55, Co 3.35	2.05/1.93	0.1 M $HClO_4$	0.820	0.918	~4.7	69	—	218
Zn/CoN-C	Zn 0.33, Co 0.14/—	2.2 ± 0.4/2.1	0.1 M $HClO_4$/ 0.1 M KOH	0.796/0.861	0.97/1.004	/6.1	/67	—	219
Meso/micro-FeCo-Nx-CN-30	Fe 0.40, Co 0.12/—	—	0.1 M KOH	0.886	954	6.3	—	—	220
Co/Zn–NCNF	Co 4.89, Zn 4.04/—	2.3/2.49	0.1 M $HClO_4$	0.797	0.997	~5.4	—	—	221
NCAG/Fe–Co	Fe 0.7, Co 1.1/ Fe 0.9, Co 1.0	—/2.787	0.1 M KOH	0.89	1.04	~5.6	—	8.5 (0.85 V)	222
Fe-Zn-SA/NC	Fe 0.22, Zn 0.1/—	—/2.45	0.1 M $HClO_4$/ 0.1 PBS/0.1 KOH	0.78/0.72/0.85	0.87/0.94/0.94	4.72/~4.2/~4.8	54.3/112.6/41.7	—	224
Fe_1Co_1-CNF	Fe 0.62, Co 0.54/—	—/2.43–2.55	0.1 M KOH	0.87	0.99	4.3	88	—	225
FeCo-DACs/NC	Co 0.80, Fe 0.76/—	~4/—	0.1 M KOH	0.877	0.984	5.7	85	11.05 (0.85 V)	228
Ni_7Fe_3-CNG	Ni 2.2, Fe 5.3/ Ni 3.4, Fe 2.2	/~3.0	0.1 M KOH	0.82	—	5.6	—	—	257

Table 3 Summary of multi-atom cluster catalysts for electrocatalytic OER

Catalysts	Metal content (ICP/XPS, wt%)	M–M distance (STEM/XAS, Å)	Electrolyte	Onset potential (V *vs.* RHE)	E (V) at 10 mA cm^{-2}	Tafel slope (mV dec^{-1})	Ref.
$Ni_{66}Fe_{34}$-NC	Fe 0.29, Ni 0.14/—	—/2.35–2.51	0.1 M KOH	1.51	1.697	120	49
Fe–NiNC-50	Fe 0.33, Ni 0.57/—	1.8/2.43	1 M KOH	1.50	1.57	54	67
NiFe@PCN	Ni 15.36, Fe 8.82/—	—	1 M KOH	—	1.54	38	69
Fe_2/Co_1-GNCL	—/Fe 0.48, Co 0.19	$2.6_{Fe-Fe}/2.6896_{Fe-Fe}$	1 M KOH	—	1.58	70	165
CoNi-SAs/NC		—/2.22	0.1 M KOH	—	1.57	58.7	167
Co–Fe–N–C (Fe activated)	Co 9.4 ($\pm$ 1.4) $\times$ 10^{-8}, Fe 8.6 ($\pm$ 1.6) $\times$ 10^{-9} mol cm^2/—	—/2.51–2.71	1 M KOH (10 ppm Fe(III))	—	1.539	37	173
HG–NiFe	—	—/2.7	1 M KOH (12 μM Fe(III))	—	—	39	179
IrCo–N–C	Ir 0.18, Co 1.02/—	~2.30/~2.30	0.1 M KOH	—	1.53	79	193
Pt_1@Fe–N–C	Pt 2.1, Fe 1.0/—	3.0/—	0.1 M KOH	1.33	1.54	62	211
Meso/micro-FeCo-Nx-CN-30	Fe 0.40, Co 0.12/—	—	1 M KOH	1.60	1.67	57	220
NCAG/Fe–Co	Fe 0.7, Co 1.1/Fe 0.9, Co 1.0	—/2.787	1 M KOH	—	1.523	70	222
Fe_1Co_1-CNF	Fe 0.62, Co 0.54/—	—/2.43–2.55	0.1 M KOH	1.56	1.73	102	225
FeCo-DACs/NC	Co 0.80, Fe 0.76/—	~4/—	1 M KOH	—	1.60	82.7	228
Ni_7Fe_3-CNG	Ni 2.2, Fe 5.3/Ni 3.4, Fe 2.2	—/~3.0		—	1.50	74	257

if any possible phase transition of multi-atom cluster catalysts exists during reactions.[202,203]

5.2.2 Valence state and electronic structure comparison. The valence state and electronic structure play key roles in disclosing the electrocatalytic activity of multi-atom cluster catalysts.[189] Yet the poor mass loadings of such materials pose a challenge in obtaining information regarding the real-time valence state and electronic structure. Real-time XANES could provide the opportunity to observe the dynamic process of a certain electrocatalytic reaction by comparing the electronic state change of active sites and has been widely explored so far.[204–206] The above mentioned techniques such as Mössbauer spectroscopy, EPR, XPS, *etc.*, could also be used to reveal the valence state information, yet the real-time use of them for multi-atom cluster catalysts in reactions remains challenging.

5.2.3 Intermediate and adsorbate identification. FTIR and Raman spectroscopy have emerged as powerful tools to observe surface adsorbates and reaction intermediates from their vibration mode on certain active sites due to their surface sensitive feature which can also be strengthened *via* surface enhancement techniques, finally elucidating the possible reaction mechanisms.[189] FTIR and Raman spectroscopy are complementary to each other, with one detecting the light adsorption from the change of dipole moment, and the other detecting the inelastic scattering by change of polarizability. In the electrocatalytic process, this may provide the chance to correlate surface adsorbates or intermediates to factors such as applied potentials, electrolytes or deuterated reagents, and gases dissolved in the solution, facilitating the investigation of the real-time kinetics. For instance, real-time Raman spectroscopy is capable of identifying possible active species during reactions through discerning the phase signals and adsorbate mode.[207] The local adsorbed species could also be used to correlate the local pH to the reaction kinetics.[208] The real-time FTIR could be used to detect superoxo-like and peroxo-like intermediates during ORR.[164] The reaction intermediates such as *CO, *COO, *CHO, *COOH, *etc.*, could be observed in the CO_2RR.[209] However, the intense adsorption of water in FTIR may affect the quality of signals, while the scattering of water is much poorer in Raman spectroscopy. The response time for real-time FTIR and Raman spectroscopy may also be not timely towards reaction intermediates with very short lifetimes.

6. Electrocatalytic applications of multi-atom cluster catalysts

6.1 H_2 production

Hydrogen is one of the most attractive and alternative fuels to replace traditional fossil fuels due to its high energy density and the advantage of yielding non-polluting products. Therefore, many techniques have been explored for the production of hydrogen wherein the electrochemical hydrogen production with the direct use of water as a source has been regarded as a promising one to produce high-purity hydrogen. Although the precious platinum catalyst has proven to be the most effective for the HER, it is expensive and scarce, which hamper its scale-up and practical application. Therefore, great efforts have been devoted to developing other promising alternatives with high activity. Besides, some non-noble metal-based electrocatalysts such as single-atom catalysts emerged as excellent candidates with promising performance for HER, but the simplicity of the active sites limited the further regulation of their electronic structure to boost the activity of active centers. However, the synergistic interaction of multi-atom cluster catalysts provides a new opportunity to regard them as some of the best HER electrocatalysts.[210,211]

It has been found that the charge polarization between metals in adjacent layers is essential to help boost the activity towards HER. Zhang *et al.* reported the preparation of dispersed A–CoPt–NC by the electrochemical activation method.[178] In their method, the Co-MOF was used to prepare atomically dispersed Pt, where Pt and Co atoms were well-trapped on the defective sites of the hollow graphite spheres.

Table 4 Summary of multi-atom cluster catalysts for electrocatalytic CO_2RR

Catalysts	Metal content (ICP/XPS, wt%)	M–M distance (STEM/XAS, Å)	Electrolyte	Potential (V *vs.* RHE)	Partial current density (mA cm^{-2})	Faradaic efficiency (%)	Tafel slope (mV dec^{-1})	TOF (s^{-1})	Ref.
Ni/Fe–N–C	Ni 0.97, Fe 0.34/—	—/2.06	0.5 M $KHCO_3$	−0.70	7.4 (CO)	98 (CO)	96	2.13	46
CuFe/N–C	Fe 0.52, Cu 1.74/—	—/2.53	0.5 M $KHCO_3$	−0.4	∼0.5 (CO)	95.5 (CO)	104	1.08 (−0.90 V)	71
Ni_2−N_6	Ni 0.18/—	2.9/2.83–2.94	1.0 M $KHCO_3$	—	150 (CO)	94.3 (CO)	111	—	166
Cu/C-0.4	—/Cu 0.32	—/∼2.5	0.1 M $KHCO_3$	−0.7	1.23_{total}	∼91 (ethanol)	164	0.0145	168
Cu/C-0.8	—/Cu 0.65	—/∼2.7	0.1 M $KHCO_3$	−0.7	1.38_{total}	∼90 (ethanol)	178	0.0087	168
Cu_1^0-Cu_1^{x+}/$Pd_{10}Te_3$ nanowires	Cu 0.10/—	2.11–2.12/ 2.49–2.51	0.2 M $NaHCO_3$	−0.78	8.6 (CO)	92 (CO)	—	—	169
Cu_3Br	—	—	0.5 M KOH	−0.7	73.24 (C_2H_4)	55.01 (C_2H_4)	—	—	170
Cu_3Cl	—	—	0.5 M KOH	−0.9	205.35 (C_2H_4)	44.68 (C_2H_4)	—	—	170
Cu_3I	—	—	0.5 M KOH	−0.8	109.42 (C_2H_4)	31.9 (C_2H_4)	—	—	170
Cu nanoclusters	—	—	1 M KOH	−1.0	312(C2+)	93.9 (C2+)			171
Pd_2 DAC	Pd 0.37/—	1.96/2.64	0.5 M $KHCO_3$	−0.85	6.76 (CO)	98.2 (CO)	148.9	—	172
$Ni_{2-}N_4$–C_2	Ni 1.7/Ni 0.53	∼2.5/∼2.5	0.5 M $KHCO_3$	−0.8	17.9 (CO)	96.6 (CO)	124.6	1.25 (−1.0 V)	181
	Ni 1.7/Ni 0.53	∼2.5/∼2.5	1.0 M $KHCO_3$ (flow cell)	−0.8/−1.0	—/56.1_{total}	96.8 (CO)/∼92(CO)	—	—	181
	Ni 1.7/Ni 0.53	∼2.5/∼2.5	1.0 M KOH (flow cell)	−0.5/−0.9	$\sim 33_{total}$/$\sim 100_{total}$	97.8 (CO)/81.3 (CO)	—	—	181
Ag_2-G	Ag 0.10/—	∼3.5/2.9	0.5 M $KHCO_3$	−0.7	11.87 (CO)	93.4 (CO)	265	—	229
Cu–Fe–N_6–C	Fe 0.83, Cu 0.91/—	—/2.60	0.1 M $KHCO_3$	−0.7	3.8 (CO)	98 (CO)	244.74	—	230
N4–Ni–Sn–N_4	—/Sn 0.30, Ni 0.28	—	0.5 M $KHCO_3$	−0.82	20.8 (formate)	86.1 (formate)	120	1.32	231
CoPc@Fe–N–C	Fe 1.04, Co 0.65/—	—	0.5 M KOH	−0.84	275.6 (CO)	93 (CO)	—	—	232
Ni/Cu–N–C	Ni 0.27, Cu 0.31/—	2.6/—	0.5 M $KHCO_3$ (flow cell)	−0.49/−0.59/ −0.69	6.6/14.5/22.4 (CO)	98/99/99 (CO)	86	1.10	233
Ni/Cu–N–C	Ni 1954 ppm, Cu 1878 ppm/ Ni 0.3, Cu 0.33	2.38–2.41/2.4	0.5 M $KHCO_3$ (flow cell)	−0.6	95.21(CO)	97.7 (CO)	175	5.75	234
Ag@Ag_8@Ag_6	—	3.0–3.2/	0.5 M $KHCO_3$	−0.6	∼2.5 (CO)	∼95 (CO)	—	6.37 (−1.1 V)	235
Fe_1−Ni_1−N–C	Fe 0.45, Ni 0.42/—	∼4.1/∼4.1	0.5 M $KHCO_3$	−0.5	2.4 (CO)	96.2 (CO)	83	—	237
Cu_8-2	—	—	0.5 M $KHCO_3$	−1.0	∼19.3(HCOOH)	92(HCOOH)	—	—	239
Ni–Zn–N–C	Ni 0.84, Zn 1.32/—	1.99–2.28/ 2.45–2.52	0.5 M $KHCO_3$	−0.8	20.23 (CO, −0.90 V)	99 (CO)	89.7	0.33 (−0.90 V)	240

Table 5 Summary of multi-atom cluster catalysts for electrocatalytic NRR

Catalysts	Metal content (ICP/XPS, wt%)	M–M distance (STEM/XAS, Å)	Electrolyte	Potential (V *vs.* RHE)	NH_3 yield rate ($\mu g\ h^{-1}\ mg_{cat.}^{-1}$)	Faradaic efficiency (FE, %)	Ref.
$Au_4Pd_2(SR)_8$	—	—	0.1 M HCl	−0.2	27.1	12.3	250
$Au_4Pt_2(SR)_8$			0.1 M HCl	−0.1	23.6	9.7	250
CNT@C_3N_4–Fe&Cu	Fe 7.0, Cu 7.81/—	1.8–2.5/—	0.25 M $LiClO_4$	−0.8/−1.2(Ag/AgCl)	—/10.27	34/—	251
PdCu/NC	Pd 2.23, Cu 2.32/—	—/∼2.3–2.5	0.05 H_2SO_4	−0.45	69.2 ± 2.5	24.8 ± 0.8	252

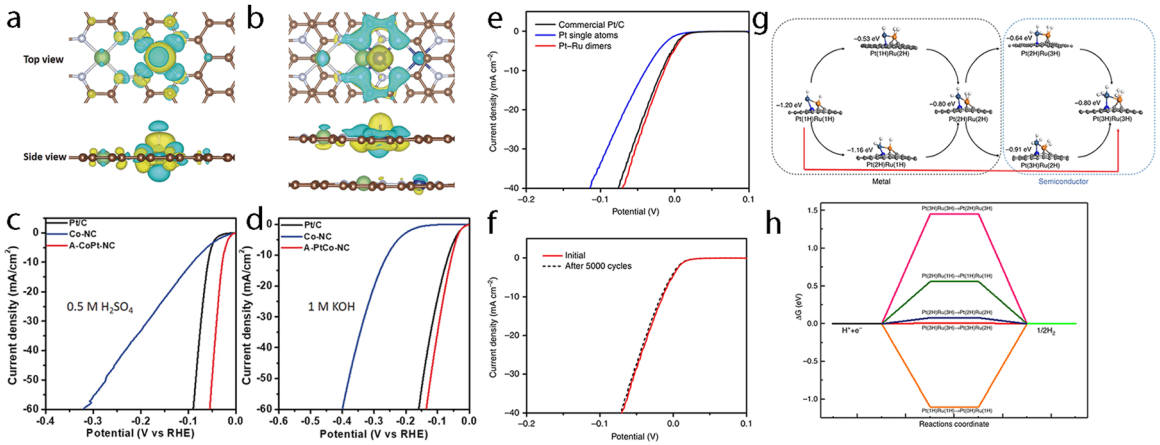

Fig. 8 (a) Side view and top view of the charge distribution of single-layered model a(Co–Pt)@N8V4. (b) Side view and top view of the charge distribution of double layered model 2(a(Co–Pt)@N8V4). C brown, N green, Pt white, and Co blue. Yellow and cyan iso-surfaces represent electron accumulation and electron depletion. (c) LSV curves of Co-NC, A-CoPt-NC and Pt/C for HER in a 0.5 M H_2SO_4 electrolyte. (d) LSV curves of Co–NC, A–CoPt–NC and Pt/C for HER in a 1 M KOH electrolyte. Reproduced with permission.[178] Copyright 2019 John Wiley & Sons. (e) The HER polarization curves recorded on Pt–Ru dimers, Pt single atoms and Pt/C catalysts. (f) Durability measurement of Pt–Ru dimer catalysts. (g) The atom structures of different H adsorption along with the adsorption energies. (h) The schematic of ΔG_H for the different hydrogen coverages of typical configurations. For each coverage, all the possible pathways were considered, and the lowest ΔG_H for each coverage is typically shown. Here, Pt(*n*H)Ru(*m*H) represents *n* H atoms adsorbed on Pt and *m* H atoms adsorbed on Ru. The orange, dark blue, light blue and gray balls represent Ru, Pt, N and C atoms, respectively. Reproduced with permission.[47] Copyright 2019 Springer Nature.

The researchers suggested based on the comprehensive understanding of the mechanism that a charge polarization may exist between the Pt and Co atoms, where a charge polarization derived from the inner layer of A–CoPt–NC may affect and alter the charge distribution of the outmost layer (Fig. 8a and b). Therefore, the adsorption strength towards *H could be tuned by the charge polarization effect around the Co atom, which leads to minimized Gibbs free energy change during the reaction. Such an optimized electronic structure could be observed from the experimental results, where the HER activity of A–CoPt–NC outperformed that of the commercial Pt/C (20 wt% Pt) in both acidic and alkaline electrolytes. Finally, the overpotential at 10 mA cm^{-2} was reported to be 27 mV for A–CoPt–NC whereas it was 59 mV for Pt/C, in an acidic solution, while the overpotential was 50 mV and 65 mV, respectively, in an alkaline solution (Fig. 8c and d).

Later, Sun *et al.* reported the preparation of a hetero-dimer structure (Pt–Ru dimers) with the use of trimethyl(methylcyclopentadienyl)-platinum(IV) ($MeCpPtMe_3$) and bis(ethylcyclopentadienyl)ruthenium(II) through an atomic layer deposition (ALD) method.[47] The electrocatalytic HER tests of the Pt–Ru dimer were compared with that of Pt/C, which showed a much-improved mass activity of 23.1 A mg^{-1} *vs.* 0.43 A mg^{-1} at an overpotential of 0.05 V (Fig. 8e). Good stability was also obtained for this catalyst as concluded after long-term stability tests (Fig. 8f). With the assistance of DFT calculations (Fig. 8g), it was found that the interaction between Ru atoms and the hydrogen intermediate could be modulated by Pt atoms and results in orbital rearrangement, where the dxz orbital of Ru became unoccupied due to sequential addition of hydrogen, thus leading to minimized Gibbs free energy towards H*, which finally improved the HER activity (Fig. 8h).

Precise synthesis of atomic-scale dual-metal electrocatalysts without the formation of nanoparticles still remains a challenge due to the inevitable aggregation during the fabrication process. Zhou *et al.* reported a top-down strategy using a dual-metal interbond as a chemical facilitator to spontaneously convert Fe nanoparticles to SACs.[212] The formation of the Rh–Fe bond may help enhance the thermodynamic stability of the dual-metal, hindering the formation of nanoparticles, thus helping to strip the Fe atom to form Rh–Fe dual metal clusters from the Fe nanoparticles (Fig. 9a). The formation of the Rh–Fe bond may endow such a catalyst with good performance towards electrocatalytic HER. This electrocatalyst outperformed commercial Pt/C, requiring an overpotential 36 mV at 10 mA cm^{-2}, with good stability in an acidic solution. From

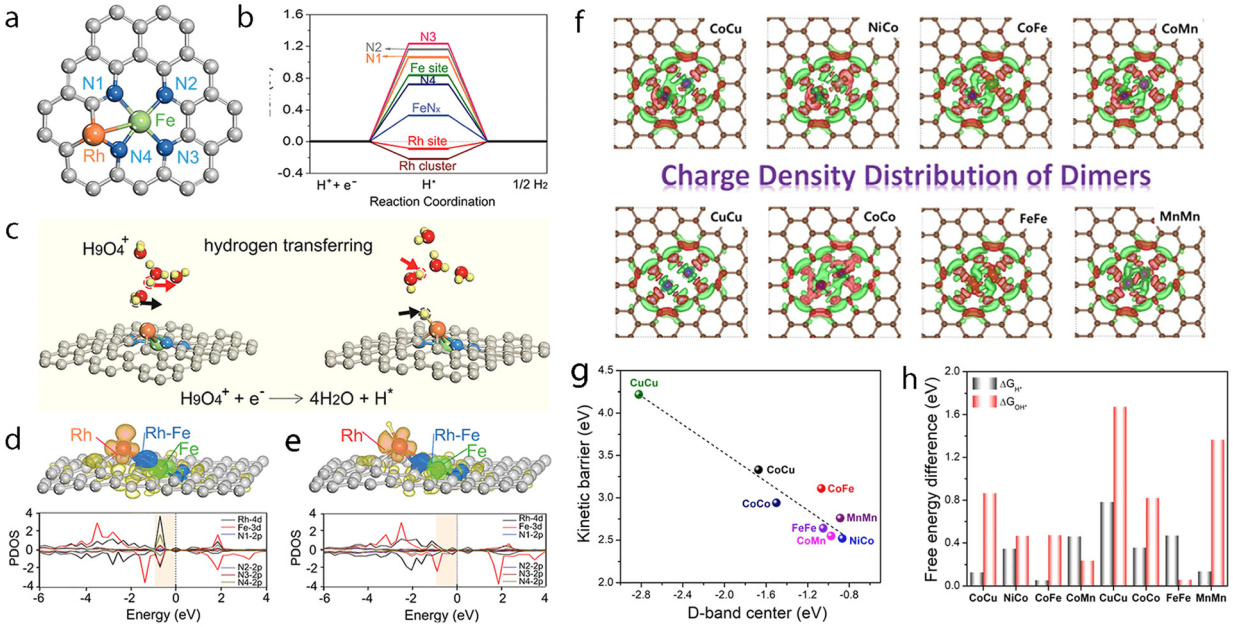

Fig. 9 (a) Possible sites to adsorb H in FR-NCS. (b) Hydrogen adsorption free energies (ΔG_H) of different sites in FR-NCS and the single Fe metal atom in NCS (Fe–N_x) and the Rh_7 cluster in NCS (Rh cluster). The Rh site in FR-NCS shows the closest value of ΔG_H to 0 eV, identifying it as the active site to bond with H. (c) Schematic illustration of the hydrogen transfer process during HER on the Rh site in FR-NCS with $H_9O_4^+$ in an acidic electrolyte. Projected density of state (pDOS) before (d) and after (e) H being adsorbed on the Rh atoms of FR-NCS with the corresponding charge distribution changes in the upper panels of each pDOS. Atomically dispersed Fe *via* the Rh–Fe bond retrieves some electrons in Rh to maintain a suitable number of active electrons in the Rh active site, which facilitates a moderate value of ΔG_H. The blue, red, and green areas correspond to the electron distribution in Rh, Rh–Fe bonding, and Fe atom, respectively. Reproduced with permission.[212] Copyright 2020 Wiley-VCH GmbH. (f) Different charge density distribution of TM-SAD-N_6C. The charge depletion and accumulation are denoted by green and red colors, respectively. (g) Linear correlation between the d-band center and the kinetic energy barrier. (h) Free energy changes of the hydronium (ΔG_{*H}) and hydroxide (ΔG_{*OH}) desorption step for TM-SAD-N_6C. Reprinted with permission.[213] Copyright 2021 Springer Nature.

the DFT calculations, it was proved that the Rh moiety could capture one hydrogen atom spontaneously from water and act as the active site (Fig. 9b and c). This can also be observed through the projected density of state (pDOS), where the density of state of Rh is one order of magnitude larger than that of Fe below the Fermi level, thus assuring Rh is active for hydrogen reduction. Meanwhile, the Fe moiety could help tune the charge distribution and the electronic structure of Rh through the Rh–Fe bond (Fig. 9d and e), releasing extra electrons from Rh for reduction. Such Rh–Fe interaction was favorable for hydrogen atom adsorption and reduction and leads to increased activity towards HER.

Recently, Kumar *et al.* reported the development of a pH-universal electrocatalyst, namely NiCo-SAD-N_6C.[213] The models of CoCu-SAD-N_6C, NiCo-SAD-N_6C, CoFe-SAD-N_6C, CoMn-SAD-N_6C, CuCu-SAD-N_6C, NiNi-SAD-N_6C, CoCo-SAD-N_6C, FeFe-SAD-N_6C, and MnMn-SAD-N_6C were considered and established to screen and guide the experimental synthesis (Fig. 9f). They found that the kinetic dissociation energy of water molecules for these models was linearly correlated with the optimized d-band centers of these electrocatalysts, where NiCo-SAD-N_6C possessed the minimum kinetic energy barrier (Fig. 9g). The calculations and comparison of the reaction profiles and the limiting step potentials also proved NiCo-SAD-N_6C to be superior to the others for HER (Fig. 9h). In total, NiCo-SAD-N_6C selected could exhibit an upshifted d-band center due to the synergistic interaction of the Ni–Co dual-site and may accelerate water dissociation and enhance HER activity, as shown by DFT calculations. Inspired by the DFT results, a precisely controlled NiCo-SAD-N_6C was obtained by co-trapping of nickel and cobalt into polydopamine, followed by pyrolysis treatment. For the HER tests in alkaline electrolytes, it required about 61 and 189 mV overpotentials to achieve -10 and -100 mA cm^{-2}, whereas for Pt/C (20%), it was about 51.5 and 227 mV, respectively. When assessed in an acidic electrolyte, the overpotentials needed were 54.7 and 116.8 mV for NiCo-SAD-N_6C to reach -10 and -100 mA cm^{-2}, while the state-of-the-art Pt/C (20%) needed 54.7 and 116.8 mV, respectively. Such an electrocatalyst also exhibited high stability with no obvious degradation during long-term stability tests, where at least 15 h runtime at -100 mA cm^{-2} and 50 h runtime at -50 mA cm^{-2} could be achieved. This work is a good example of DFT-assisted experimental screening of potential electrocatalysts for HER and is worth further endeavors.

The above studies proved that the resulted synergistic effects based on N-bridged hetero dimers, including precious metals, could help improve the HER performance. In a different approach, Yang *et al.* developed an O-bridged W-Mo non-precious transition metal hetero-dimer capable of pH-universal electrocatalytic hydrogen evolution.[214] The EXAFS fitting disclosed that such dimers

exhibited a W–O–Mo–O–C configuration, where an oxygen-bridged tetrahedron [WO_4] and a distorted octahedron [MoO_6] unit coexisted in the structure. With the assistance of theoretical calculations, they found that the non-metal atom around the metal atoms provided the active sites that were responsible for binding the hydrogen atoms with an optimized Gibbs free energy during the HER tests. The electrons from the metal centers were redistributed to the oxygen sites due to the synergistic interaction and enhanced the binding strength of the hydrogen atom, leading to an improved HER activity throughout the entire pH range.

6.2 Oxygen electrocatalysis

Catalysts capable of both ORR and OER are highly desirable for water splitting, fuel cells, metal-air batteries, *etc.* Noble metal catalysts such as Pt-based alloys and Ir/Ru-oxides are recognized as state-of-the-art ORR and OER electrocatalysts, respectively. But as rare metals, their limited availability in nature and high price hamper their scale-up application from economic considerations. Further, the multi-electron reactions of OER and ORR need large thermodynamic overpotentials, while sluggish reaction kinetics are also encountered due to their high reaction barriers. Thus, the development of novel electrocatalysts for the rapid OER and ORR remains a big challenge and the exploration of such earth-abundant element-based catalysts is urgent. Although the SACs already proved their outstanding or even better performance than the Pt-based nanocatalysts in ORR, some of the SACs tend to lose their stability during the reaction. For instance, the Fe SAC, which has been proved to be the most active one towards ORR in alkaline electrolytes, may experience the Fenton reaction during the ORR, which may destroy the catalyst, thus affecting its durability. The capability of SACs for catalyzing the OER is still unsatisfactory. However, multi-atom cluster catalysts can help enhance the catalytic activity of the active sites by reducing the reaction barriers for *OOH, *OH, and *O through synergistic effects. They can also increase the activity by increasing the loading of metals, providing a more economic use of metal elements with the maximum utilization of active metal sites.

The ORR activity of non-precious metal-based electrocatalysts is usually not satisfactory due to their sluggish reaction rates in acidic media. Despite improvement by SACs, the expectations for better activation of O_2 with lowered reaction barrier, proven reaction mechanism, smaller overpotential, and good long-term stability still call for better electrocatalysts.[215–217] In 2017, Li's group reported a kind of Fe–Co dual-site embedded into N-doped porous carbon (Fig. 10a).[45] Such a catalyst was synthesized through a host–guest strategy, where a Zn/Co bimetallic MOF was used to encapsulate the $FeCl_3$ salts in the cavity of the MOF. Subsequent pyrolysis and graphitization resulted in the production of (Fe,Co)/N–C, which was confirmed by HAADF-STEM, XAFS, and Mössbauer spectra. The (Fe,Co)/N–C catalyst exhibited an onset potential of 1.06 V *vs.* RHE and a half-wave potential of 0.863 V *vs.* RHE compared to 1.03 V *vs.* RHE and 0.858 V *vs.* RHE in acid solution, respectively, of commercial Pt/C. Long-term cyclic voltammetry testing for 50 000 times and H_2/air fuel cell testing

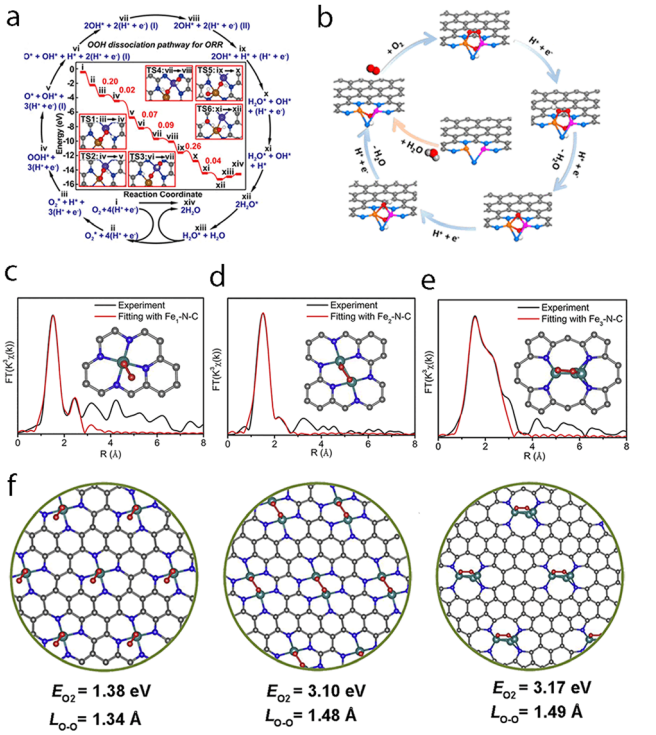

Fig. 10 (a) Energies of intermediates and transition states in the mechanism of ORR at (Fe,Co)/N-C from DFT. Reprinted with permission.[45] Copyright 2017 American Chemical Society. (b) Proposed ORR mechanism on the $FeCoN_5$–OH site. Reprinted with permission.[105] Copyright 2019 American Chemical Society. The k_3-weighted Fourier-transform experimental Fe K-edge EXAFS spectrum (black line) and the fitting curve (red line) of (c) Fe_1–N–C, (d) Fe_2–N–C, and (e) Fe_3–N–C. The insets of (c), (d), and (e) show the optimized structural model of Fe_2–N–C, Fe_1–N–C, and Fe_3–N–C (Fe green, N blue, C gray, and O red) through theoretical calculations, respectively. (f) Superoxo-like adsorption at Fe_1–N–C, peroxo-like adsorption at Fe_2–N–C and peroxo-like adsorption at Fe_3–N–C. Reprinted with permission.[164] Copyright 2019 Elsevier.

for 100 h further established the excellent stability of this dual-site catalyst. From the DFT calculations, it was suggested that the efficient activation of O_2 from the synergistic influence of Fe–Co dual sites contributed the most towards the improved activity. The free energies for the conversion of O_2 and *OOH into *O and *OH were greatly decreased for (Fe,Co)/N–C compared to that for the Fe SAs/N–C and Co SAs/N–C catalysts. Further, similar Fe–Co dual sites were investigated for ORR in alkaline media, and a better onset potential of 1.15 V *vs.* RHE and a half-wave potential of 0.954 V *vs.* RHE were exhibited, compared with 1.05 V *vs.* RHE and 0.842 V *vs.* RHE of commercial Pt/C.[218] The use of such Fe–Co catalysts was also extended to Zn–air batteries, where a high voltage of 1.31 V and 1.23 V was obtained at discharge current densities of 20 mA cm^{-2} and 50 mA cm^{-2}, respectively. In their model for theoretical calculations, it is noted that the terminal -OH groups were used to bridge dual atoms during the reaction path to help tune the reaction energies. Later, Xiao *et al.* explained in detail how a -OH coordinated Fe–Co dual-site could affect the ORR activity through the optimization of adsorption–desorption behavior of oxygen species through the electronic and geometric regulation of such catalysts (Fig. 10b).[105] As -OH is an

electron-withdrawing functional group, the coordination with -OH could upshift the E_{redox} of Fe(III)/Fe(II), which could be used as an effective M–O binding energy indicator. The higher E_{redox} may indicate a weaker Fe–O binding strength and lead to easy intermediate desorption, thus leading to promoted activity.

As discussed above, previous research suggests that the Fe SAC is an excellent catalyst for the ORR. The practical demand for performing the ORR under suitably applied bias still requires catalysts that could help with better oxygen activation and accelerate the reaction kinetics. Besides, the inevitable Fenton reaction between the Fe active sites and the by-product of H_2O_2 may produce hydroxyl and oxygen radicals, which may affect the active sites, leading to reduced durability. Ye *et al.* prepared a series of catalysts through the precursor preselection method and obtained tunable Fe_1–N–C, Fe_2–N–C, and Fe_3–N–C electrocatalysts (Fig. 10c–e).[164] They found that these three moieties could exhibit different O_2 adsorption, as concluded through the observations made from low-temperature Fourier-transform infrared spectroscopy, superoxo-like adsorption configuration (end-on adsorption mode) for Fe_1–N–C, and peroxo-like adsorption (side-on adsorption mode) for Fe_2–N–C and Fe_3–N–C (Fig. 10f). Also, the Fe clusters could promote the tailoring of N-species towards higher activity and electron transport, which were embedded in the carbon matrix during the pyrolysis process. The adsorption configuration of O_2 onto Fe_x–N–C may contribute to the activation of O_2 molecules. In detail, in the side-on mode, more electrons from the multi-active sites could be donated into the empty orbitals of the adsorbed oxygen and improve the activation of this molecule. Besides, Fe_2–N–C could provide more catalytically active sites than Fe_3–N–C when they both have comparable Fe content. Furthermore, Fe_2–N–C could provide more pyridinic N species than Fe_1–N–C and was more graphitized than Fe_3–N–C. As a result, Fe_2–N–C possessed an excellent performance in the acidic media than Fe_3–N–C and the poorest one to perform was Fe_1–N–C. Fe_2–N–C with a half-wave potential of 0.78 V *vs.* RHE was the best among the three materials and was almost comparable to the commercial Pt/C with only −20 mV and −79 mV disparity in 0.5 H_2SO_4 and 0.1 M $HClO_4$, respectively. A slight −20 mV shift was observed after the accelerated test of 20 000 cycles, which indicated the remarkable durability of Fe_2–N–C. Further measurements of these catalysts in an alkaline solution also suggested that Fe_2–N–C could be operated in a universal pH range.

All the examples listed above used either the homo-atom or hetero-atom Fe-based clusters for their potential application for ORR.[191] The use of other hetero-atom clusters is also favorable for ORR due to the inherent electronegativity difference between the atoms, which may lead to different adsorption strengths towards the intermediates and thus activate the adsorbate. For instance, Lu *et al.* reported the preparation of Zn/CoN-C with the dispersion of zinc and cobalt salts in chitosan followed by pyrolysis and a subsequent etching process.[219] As the electronegativity of zinc (1.65) is slightly smaller than that of cobalt (1.88), it makes it easier for zinc to donate the electrons from the outermost orbital due to the synergistic interaction. Experimentally, the XANES spectrum (Fig. 11a and b) of Co atoms in Zn/CoN-C suggested a valence state between that of cobalt foil and CoN-C, while the XANES spectrum of Zn atoms in Zn/CoN-C indicated a valence state higher than that of ZnN–C. This coincided with the electronegativity trend mentioned above and allowed zinc to donate electrons and helped tune the electronic structure of Zn/CoN-C.

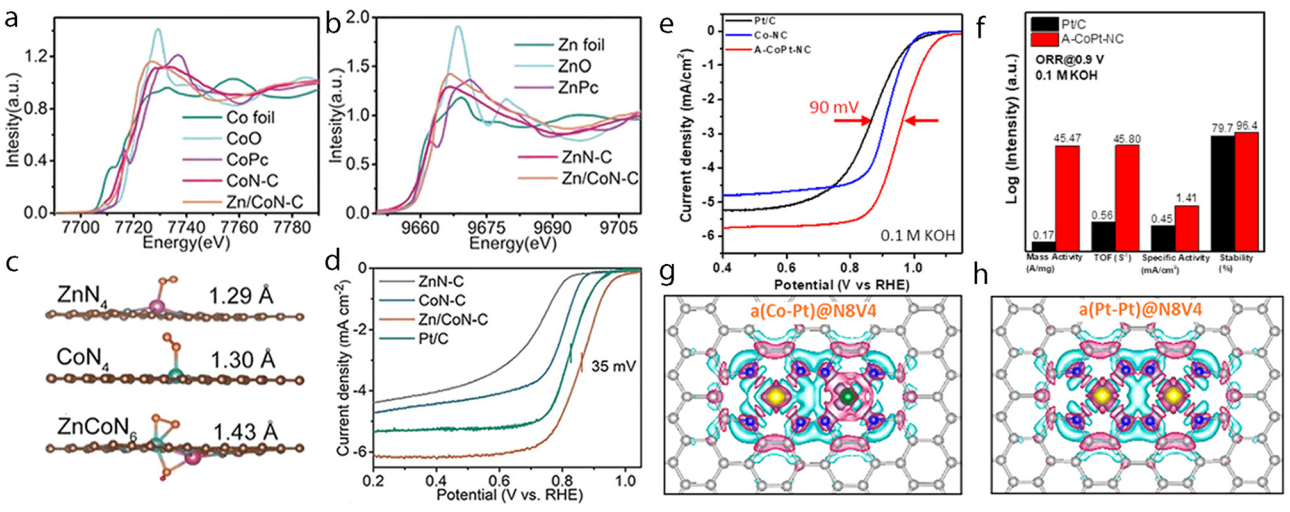

Fig. 11 (a) Co K-edge XANES. (b) Zn K-edge XANES. (c) Optimized geometry of O_2 adsorption configuration on the ZnN_4, CoN_4, and $ZnCoN_6$(OH) systems. The brown, blue, yellow, green, purple, and red balls are C, N, O, Zn, Co, and H atoms, respectively. (d) ORR linear scan voltammogram (LSV) curves for different catalysts in an O_2 saturated 0.1 M KOH solution. Reprinted with permission.[219] Copyright 2019 John Wiley & Sons. (d) ORR linear sweep voltammetry curves of Co–NC, A–CoPt–NC, and Pt/C in a 0.1 M KOH electrolyte. (e) Comparison of mass activity, TOF, specific activity, and stability of A–CoPt–NC and Pt/C for ORR. (f) ORR free energy profiles of a(Co–Pt)@N8V4 at the equilibrium potential (U = 1.23 V), onset potential, and zero potential. (g and h) Local densities of state of a(Co–Pt)@N8V4 and a(Pt–Pt)@N8V4. (i and j) Top view of the charge densities of a(Co–Pt)@N8V4 and a(Pt–Pt)@N8V4. The pink and aqua isosurfaces with an isosurface level of 0.0025e/a_0 represent electron accumulation and depletion areas, respectively. Reprinted with permission.[177] Copyright 2018 American Chemical Society.

Therefore, the O–O bond in the adsorbed $*O_2$ could be elongated from 1.23 Å to 1.43 Å by the $ZnCoN_6(OH)$ moiety (Fig. 11c). It could be shown through the DFT calculations that this may lead to decreased dissociation energy for $*O_2$. For comparison, the length of the O–O bond for ZnN_4 and CoN_4 moieties was only 1.29 Å and 1.30 Å, respectively (Fig. 11c). Furthermore, the higher activation ability for Zn/CoN-C towards the O–O bond led to greatly improved activity with a high half-wave potential of 0.861 V *vs.* RHE, which is more positive than that of Pt/C (by 35 mV) with good stability (Fig. 11d).

It has been known for SACs that the selection of the substrate has a great impact on their performance towards ORR. A similar conclusion could also be made for multi-atom cluster catalysts. In addition, interaction with other atoms could tune their electronic structures. The electronic structure and the substrate can exert a combined effect on the ORR. Zhang *et al.* prepared a Pt–Co nitrogen–carbon-based catalyst (A–CoPt–NC).[177] The local coordination environment of the metal pair was directly observed using the HAADF imaging, which suggested that the two metals were trapped in the defect sites of the substrate. The ORR measurements revealed a half-wave potential of 0.96 V *vs.* RHE, which was 90 mV superior to that of Pt/C in alkaline media (Fig. 11e and f). Both a(Co–Pt)@N8V4 and a(Pt–Pt)@N8V4 models were designed to investigate the reaction mechanism. The free energy reaction profiles suggested that the first protonation (O_2 to *OOH) was the rate-determining step, where the change in free energy was 0.3 eV for a(Co–Pt)@N8V4. This value was smaller than that of a(Pt–Pt)@N8V4 (1.07 eV) and suggested a strong binding effect between a(Co–Pt)@N8V4 and O_2. Further electronic structure analysis suggested that 3d orbitals of Co in the a(Co–Pt)@N8V4 moiety were up-shifted and might enhance the binding strength between the a(Co–Pt)@N8V4 moiety and O_2 and other intermediates. A charge accumulation on Co and a charge depletion on Pt, leading to an asymmetric deployment of the surface charge, ensured the effective reduction of O_2 on Co (Fig. 11g and h). Thus, the synergistic combination of defect coordination and electronic structure could enhance the ORR activity of a(Co–Pt)@N8V4.

The multi-atom site catalysts are usually more active than their respective single-atom counterparts for the OER in an alkaline medium. Wang *et al.* proved this using molecular dual atom-doped graphene (Fig. 12a–c).[179] In detail, as-synthesized pristine Ni sites exhibited poor activity towards the OER in an alkaline solution. However, the introduction of Fe salts into the electrolyte and the subsequent cyclic voltammetry scanning led to the *in situ* generation of the Ni–Fe dual atom moiety, which could exhibit remarkably enhanced OER activity. They concluded that the adsorption of OH^- to form a bridge geometry with Ni–Fe dual-sites helped improve the activity of such Ni–Fe catalysts. Furthermore, Hu's group reported the *in situ* formation of Co–Fe–N–C, where the Co–Fe dual sites were reconstructed from the single atom Co catalysts (Co–N–C) through cyclic voltammetry scanning of an Fe(III) containing alkaline electrolyte, and explained how the dual atom sites could be formed through operando XAS techniques (Fig. 17d–g).[173] Recently, they provided further insights into the mechanism of OER with such dual sites, with a combination of operando XAS and electrokinetic methods.[176]

The development of a bifunctional ORR/OER catalyst is necessary for its use in rechargeable metal–air batteries.[193,220–228] Multi-atom cluster catalysts are also promising as bifunctional ORR/OER catalysts. Han *et al.* reported an atomically dispersed binary Co–Ni catalyst prepared by the pyrolysis of dopamine-coated metal–organic frameworks.[167] This DAC was embedded in N-doped hollow carbon nanotubes (denoted as CoNi-SAs/NC). The remarkable activity of CoNi-SAs/NC for both ORR and OER in alkaline media is reflected by an exceptional E_{gap} of 0.81 V between the half-wave potential of ORR and that of OER at a current density of 10 mA cm^{-2} (Fig. 12d and e). This performance was close to that of Pt/C-IrO_2 catalysts and outperformed most of the other bifunctional nonprecious metal electrodes. Through theoretical calculations, they found that Co–Ni–N could change the rate-determining step (RDS) from hydrogenation of molecular O_2 in NC and Ni–N to protonation of OH* with reduced energy difference for the ORR step, where a similarly reduced RDS energy difference was also found in the OER for Co–Ni–N compared to the others (Fig. 12f–j). Inspired by these results, this catalyst was further assembled to evaluate its activity in the Zn–air battery, where a better charging and discharging polarization curve could be observed for CoNi-SAs/NC, with 1.16 V (charging) and 2.05 V (discharging) at 10 mA cm^{-2}, and 0.97 V (charging) and 2.22 V (discharging) at 50 mA cm^{-2}, when compared with that of Pt/C-IrO_2 as the cathode (1.17 V (charging) and 2.12 V (discharging) at 10 mA cm^{-2}, 1.05 V (charging) and 2.28 V (discharging) at 50 mA cm^{-2}). The maximum power density was 101.4 mW cm^{-2} and the discharge-specific capacity was 750.9 mA h g^{-1} for CoNi-SAs/NC-based cells, while these were 112 mW cm^{-2} and 719.2 mA h g^{-1}, respectively, for Pt/C. Besides, such a catalyst also exhibited a good cycling rechargeability under 5 mA cm^{-2}, where negligible voltage fading was found after 95 cycles. This was much better than the obvious decay observed for Pt/C-IrO_2, just after 46 cycles. The further assembly of flexible solid-state Zn–air batteries and related measurements at diverse angles also proved the stable discharge and charge performance of such catalysts.

6.3 Electrocatalytic CO_2 reduction reaction

The exploitation of fossil fuels has triggered an excessive emission of greenhouse CO_2 gas, which causes severe environmental problems. Thus, there is a great demand for developing powerful techniques that can reduce CO_2 to value-added products. The electrochemical CO_2 reduction technique can convert CO_2 into different kinds of energetic carbon products with the use of renewable electric energy. Thus, it can be regarded as a promising strategy to realize carbon utilization. However, the difficulty in overcoming the high thermodynamic reaction energy barrier and improving the reaction rate kinetically with high selectivity makes it imperative to develop highly active catalysts. Although the recent research on single-atom catalysts has already proven their advantage in CO_2 reduction to CO, they are normally inefficient in catalyzing CO_2 to more

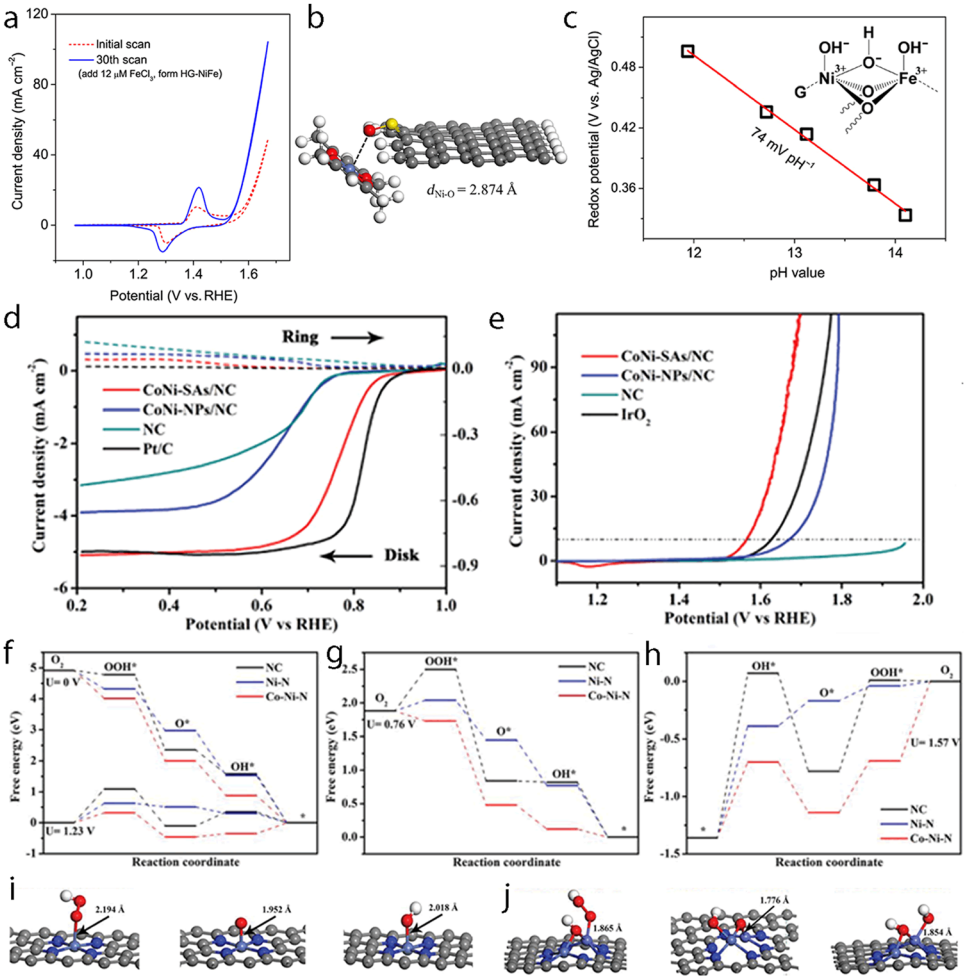

Fig. 12 (a) Comparison of the initial and steady cyclic voltammetry curves of HG–Ni conducted in a glass cell containing 1 M KOH + 12 μM $FeCl_3$. Scan rate, 50 mV s^{-1}; rotation rate, 2000 rpm. (b) A DFT calculation-derived model to indicate the conjugation of $Ni(acac)_2$ onto HG. The dopant of HG was a sulfoxide group as one representative interacting site. The gray, white, red, and yellow spheres represent C, H, O, and S atoms, respectively. The Ni atom is represented by a dark blue sphere. (c) Pourbaix diagram, illustrating the formal potentials of redox *versus* pH values of KOH solutions. The inset shows the proposed configuration for the adsorption of HO^- ions onto Ni–Fe sites before OER. Reprinted with permission from AAAS.[179] Copyright 2018. (d) ORR polarization curves at 1600 rpm. (e) OER polarization curves. Free energy diagram of (f) Ni–N and Co–Ni–N models at 0 and 1.23 V, (g) ORR, and (h) OER processes on NC, Ni–N, and Co–Ni–N. Reprinted with permission. Proposed reaction path on Ni–N (i) and Co–Ni–N (j). Reprinted with permission.[167] Copyright 2019 John Wiley and Sons.

complex products. Thus, the incorporation of more atoms to form multi-atom cluster catalysts may hold promise to either boost the performance of CO_2RR or provide more catalytic reaction sites to facilitate complex reactions and produce CO, HCOOH, CH_4, C_2H_4, *etc.*, through effective interactions.[172,229–239]

It is well known that the transition metals can exhibit varied interaction strength with the intermediates due to their electronic features. Thus, the inclusion of a hetero-atom can help tune the activity through the tuning of the interaction strength with intermediates.[46,230,231,233,240] As mentioned in previous sections, the difference in electronegativity can lead to diverse binding strength towards the adsorbate, leading to a possible decrease in free energy change to certain intermediates, thus tuning the activity during reactions. For instance, the Ni SAC could exhibit high selectivity for CO production, but a large overpotential was required for the first step of *COOH formation and thus suffered from sluggish reaction kinetics. Other catalysts such as the Fe SAC and Co SAC showed a high reaction rate for the formation of *COOH, yet the strong interaction of *CO with the metal made it difficult for CO to desorb from the catalyst's surface. Accordingly, Ren *et al.* reported the synthesis of a uniform Ni–Fe DAC, which exhibited a high selectivity of above 90% for CO production over a wide potential range from −0.5 to −0.9 V *vs.* RHE and also retained high stability even after the long-term electrolysis testing (30 hours) (Fig. 13a).[46] Their conclusion from the DFT calculations was that the Ni–Fe dual-site could synergistically decrease the reaction barrier of the first step (*COOH formation), while the CO-adsorbed moiety could facilitate the release of CO (Fig. 13b and c). Ni–Fe dual sites also gave an opportunity for their use as bifunctional electrocatalysts of CO_2RR and OER for Zn–CO_2 batteries.[241] Recently, Chen *et al.* reported that the

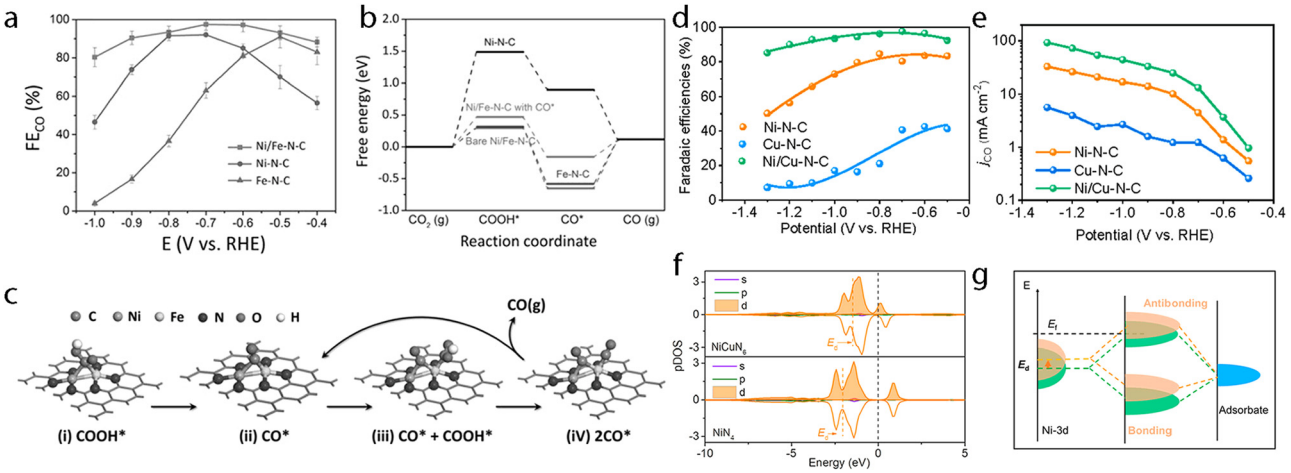

Fig. 13 (a) FE_{CO} for catalysts obtained in a CO_2-saturated 0.5 M $KHCO_3$ solution. (b) Calculated free energy diagrams for CO_2RR yielding CO on different catalysts. (c) The catalytic mechanism on a diatomic metal–nitrogen site based on the optimized structures of adsorbed intermediates COOH* and CO*. Reprinted with permission.[46] Copyright 2019 John Wiley and Sons. (d) faradaic efficiency for CO production at various applied potentials. (e) Tafel plots for CO production on various electrodes. (F) pDOS of Ni in NiN_4 and $NiCuN_6$. (f) Schematic illustration explaining the change of metal–adsorbate interaction by altering the metal d band center (E_d). Reprinted with permission. Copyright 2022 American Chemical Society.[234]

introduction of Cu atoms to form a hetero Ni/Cu–N–C material could decrease the energy barrier for intermediate adsorption and regulate the d-band center to obtain optimized binding affinity towards intermediates. Thus, $NiCuN_6$ displays excellent selectivity for CO production than its counterpart Ni–N-C and Cu–N–C with large current density in flow cell tests (Fig. 13d–g).[234] Later, other kinds of similar hetero-atom electrocatalysts were also reported, such as Ni–Fe, Ni–Cu, Ni–Zn, Ni–Sn, Cu–Fe, *etc.*,[230,231,233,234,236,237,250] and proved the existence of effective synergistic effects between them during CO_2RR.

In the above example, hetero-atom configurations were used for the synergistic benefit of decreasing the reaction barrier. By optimizing the electronic structures, homo-atom-based electrocatalysts also hold potential as promising candidates for CO_2RR. Jiao *et al.* found that the Cu-doped $Pd_{10}Te_3$ nanowires featured high activity for CO_2 conversion to CO, as the active sites in this catalyst comprised of Cu_1^0–Cu_1^{x+} pairs, which were stabilized by the Te surface defects from $Pd_{10}Te_3$ nanowires.[169] Later, Yao reported using $Ni_2(dppm)_2Cl_3$ (dppm = bis(diphenylphosphino)methane) as a precursor to be pyrolyzed and prepared N_2/NC electrocatalysts.[166] They found, through the operando XAS (Fig. 17h–i), that the oxygen bridged O–N_2–N_6 configuration could be formed during reactions, which significantly lowered the free energy change of *COOH intermediate (Fig. 14b and c) formation and led to >94% faradaic efficiency during CO_2RR (Fig. 14a). Recently, Zhang *et al.* used the electrospun-pyrolysis method to prepare Ni_2–N_4–C_2 with $Ni(acac)_2$. The samples pyrolyzed at 1000 °C could form such dual-site materials.[181] Theoretical calculation showed that the modulated d-band center could exhibit optimized adsorption towards intermediates, leading to boosted activity for CO_2RR.

Multi-atom cluster catalysts have proved their outstanding performance towards CO_2 reduction to CO. Yet, the further reduction of CO_2 to more valued-added multi-carbon chemicals is challenging.[170,171,242] Copper-based catalysts are promising as diverse carbon-based fuels could be produced by them due to their moderate strength with various intermediates during the reaction. The copper-based multi-atom clusters could provide multi-active sites for the complex reaction pathways while inheriting the advantage of high activity and selectivity from SACs. The previous research based on copper complexes successfully observed the dynamic and reversible transformation of copper to form large nanoclusters, which are necessary for CO_2 conversion to methane.[243] A similar reversible process was also reported by Karapinar *et al.* for CO_2RR to ethanol with the Cu–N–C SAC.[244] Further, Xu *et al.* reported a carbon-supported, atomically dispersed Cu SAC, fabricated from an amalgamated Cu–Li method to produce ethanol.[168] Recently, Lan *et al.* also reported using crystalline trinuclear copper clusters for the conversion of CO_2 to C_2H_4 (Fig. 14d–f).[170] In detail, Cu_3–X (X = Cl, Br, NO_3) complexes containing three different counter anions were fabricated (Fig. 14d). Among them, Cu_3–Br could deliver the highest C_2H_4 production performance with considerable stability. It exhibited good selectivity from −0.7 V to −1.1 V *vs.* RHE. For instance, the faradaic efficiency of Cu_3–Br at −0.7 V *vs.* RHE was about 55% (Fig. 14e and f). The theoretical calculations also suggested that two adjacent Cu centers played a key role in the C–C coupling of *CHO intermediates and promoted the conversion of CO_2 to C_2H_4.

6.4 Electrocatalytic N_2 reduction reaction

Ammonia contributes the most to modern agriculture and is essential for the synthesis of a great variety of pharmaceutical products. Yet the industrial production of ammonia mainly relies on the Haber–Bosch process. Harsh production conditions, high global energy consumption, and high CO_2 emissions call for the development of new techniques to achieve the fixation of

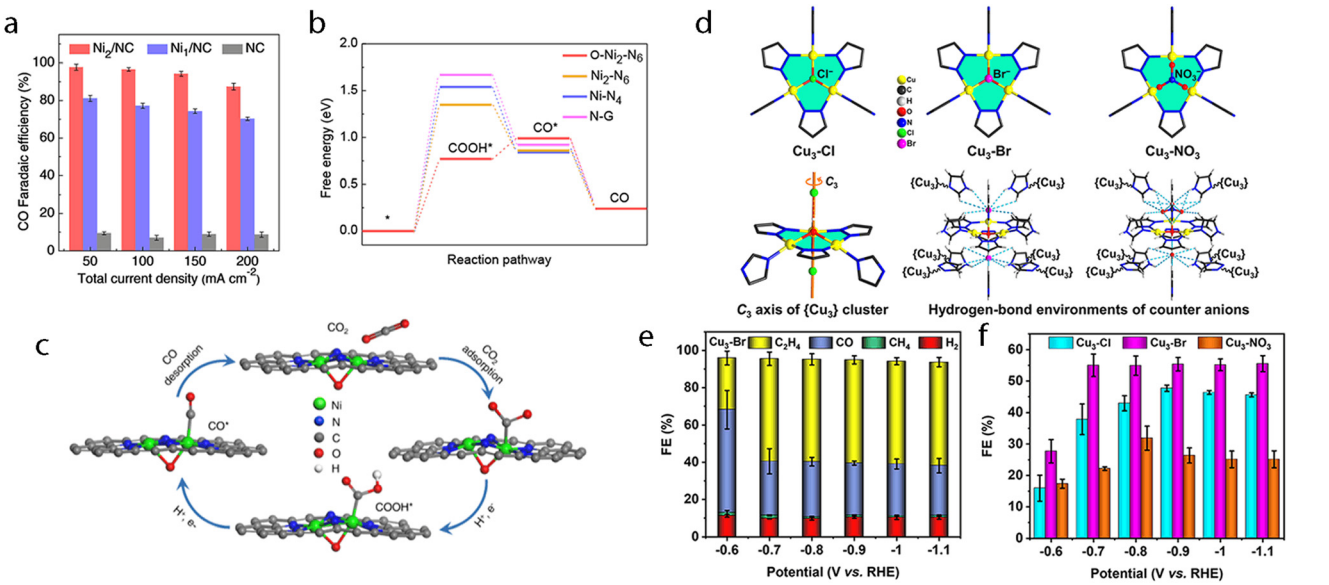

Fig. 14 (a) CO FE in the current density range 50–200 mA cm^{-2}. (b) Calculated Gibbs free energy diagrams for CO_2 electroreduction to CO on various catalysts. (c) Proposed reaction pathways on O–Ni_2–N_6. Reprinted with permission.[166] Copyright 2021 American Chemical Society. (d) The molecular structure characteristics of Cu_3-X. (e) faradaic efficiency (FE) (H_2, CH_4, CO and C_2H_4) of Cu_3–Br at different potentials (−0.6 V to −1.1 V). (f) The contrast of FE for CO_2RR catalyzed by Cu_3–Cl, Cu_3–Br and Cu_3–NO_3 at different applied potentials (−0.6 V to −1.1 V). Reprinted with permission.[170] Copyright 2021 John Wiley and Sons.

nitrogen under mild conditions. Thus, the electrocatalytic nitrogen reduction reaction (NRR) is emerging as an attractive strategy due to its favorable economics and environmentally benign fixation of nitrogen under ambient conditions. Since the emergence of multi-atom cluster catalysts, theoretical researchers have put great efforts to guide the development of NRR from the calculation aspect.[245–247] Very recently, there have been some reports on the use of multi-atom cluster catalysts for NRR from the experimental research standpoint as well.[248,249]

The precise synthesis by anchoring metal precursors to the substrate can be used to obtain the precious metal multi-atom cluster catalysts for NRR. Yao *et al.* developed the synthesis of bimetallic $Au_4Pt_2(SR)_8$ clusters.[250] After anchoring these clusters onto defective graphene, a hetero metal electrocatalyst of Au_4Pt_2/G with precise structural information could be obtained (Fig. 15a–d). The electrochemical NRR (Fig. 15c and d) using Au_4Pt_2/G demonstrated that this material could generate a maximum NH_3 yield of up to 23.6 μg mg^{-1} h^{-1} at −0.1 V *vs.* RHE with a faradaic efficiency of *ca.* 9%. The yield of NH_3 was better than that from the $Au_4Pt_2(SR)_8$ electrocatalyst, where a maximum NH_3 yield rate of 7.9 μg mg^{-1} h^{-1} could be obtained at −0.1 V with a faradaic efficiency of 9.7%. Furthermore, Au_4Pd_2/G obtained by the replacement of the Pt atom with Pd could provide a maximum NH_3 yield rate of 27 μg mg^{-1} h^{-1} at −0.2 V with a faradaic efficiency of *ca.* 12%, which was higher than that of Au_4Pt_2/G.

The confinement effect can help enhance the interaction between the reactant and the active sites from the catalysts. The unique microenvironment formed due to such a confinement effect can also promote an effective interaction between multiple active sites, which is beneficial for the complex reaction processes

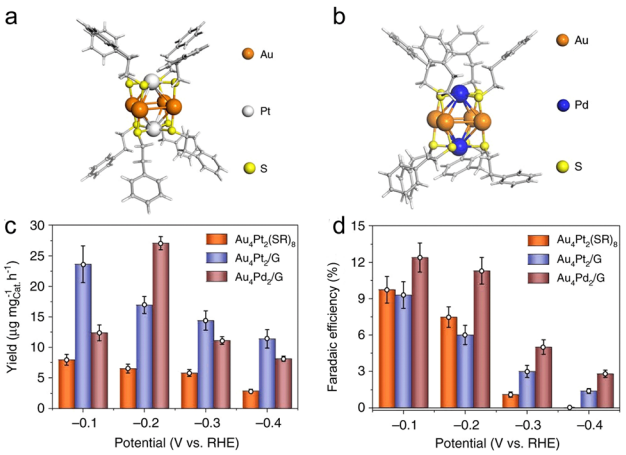

Fig. 15 (a and b) Atomic structures of the clusters. (c) NH_3 production rate. (d) faradaic efficiency of ammonia production at different potentials. Reprinted with permission.[250] Copyright 2020 Springer Nature.

of NRR. Therefore, the concept of "sub-nano reactors" was adopted by Wang *et al.* with the use of graphitic carbon nitride to confine multiple Fe and Cu atoms with the surrounding nitrogen atoms.[251] The obtained CNT@C_3N_4-Fe&Cu could achieve an NH_3 yield of 9.86 μg mg^{-1} h^{-1} with a faradaic efficiency of 34% (Fig. 16a and b). This was a nearly double yield and a 54% increase in the faradaic efficiency when compared with its single metal counterparts. From the theoretical understanding obtained with DFT calculations, they found that the formation of Fe–Cu could help optimize the reaction process of N_2 reduction. The rate-determining step could be altered from the 5th hydrogenation step (NH* → NH_2*, 0.71 eV)

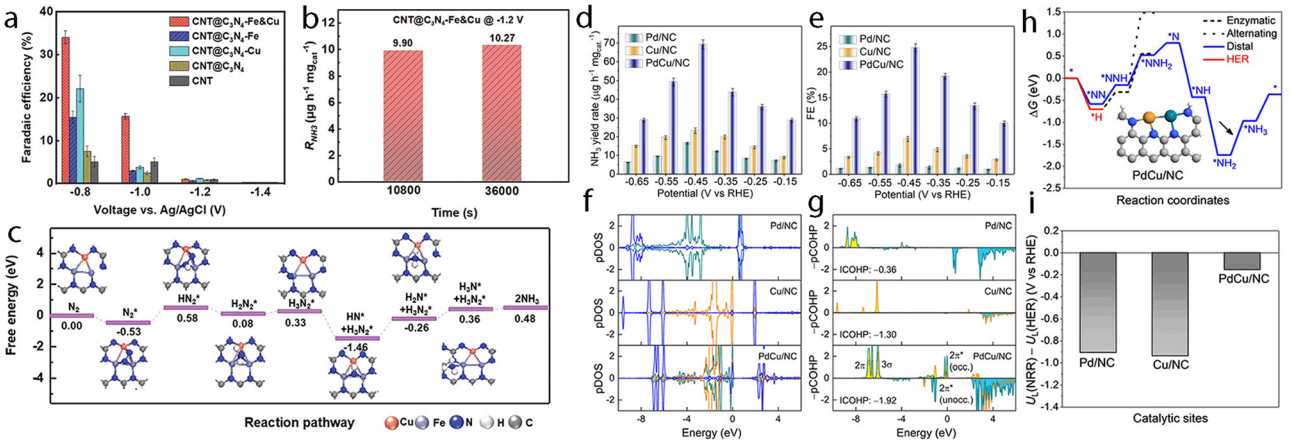

Fig. 16 (a) The faradaic efficiencies of the materials at different potentials. (b) The ammonia yield rate for 3 and 10 h tests at −1.2 V *vs.* Ag/AgCl in 0.25 M $LiClO_4$. Free energy diagrams of NRR on Fe_2Cu (c) clusters in the cavity of g-C_3N_4. Reprinted with permission.[251] Copyright 2020 Wiley-VCH GmbH. (d) NH_3 yield rates and (e) FEs of PdCu/NC, Pd/NC, and Cu/NC at each given potential in N_2-saturated 0.05 M H_2SO_4. (f) Partial density of states (pDOS) of N_2 adsorption on Pd/NC, Cu/NC, and PdCu/NC. Blue lines: 2p orbital of N, orange lines: 3d orbital of Cu, and cyan lines: 4d orbital of Pd. (g) Projected crystal orbital Hamilton population (−pCOHP) and its integrated value (ICOHP) of N_2 adsorption on Pd/NC, Cu/NC, and PdCu/NC. Orange and cyan lines indicate the bondings between N–Cu and N–Pd. The energy value is with reference to the Fermi level. Calculated free energy diagrams of NRR and HER on (h) PdCu/NC systems. The alternating pathway is favored on Pd/NC and Cu/NC, whereas the distal pathway is the most energetically preferred on PdCu/NC. The asterisk (*) represents a reactive intermediate or a vacant surface site. Insets: Structural models. (i) Difference between the limiting potentials for NRR and HER of Pd/NC, Cu/NC, and PdCu/NC. Reprinted with permission.[252] Copyright 2020 Wiley-VCH GmbH.

for CNT@C_3N_4-Fe and the N_2 adsorption step (0.86 eV) for CNT@C_3N_4-Cu to the initial hydrogenation step (N_2* → N_2H*, −0.58 eV) for CNT@C_3N_4-Fe&Cu (Fig. 16c). The introduction of Cu could also provide an electron reservoir to supply electrons to the Fe atom. The existence of Fe–Cu also improved the electron transfer when compared to single-atom catalysts. All these combined helped to boost the activity of CNT@C_3N_4-Fe&Cu towards NRR.

Based on the above-mentioned examples, effective interaction and activation of N_2 molecules from a heteroatom configuration can help enhance the intrinsic performance of an electrocatalyst. However, the NRR process is inevitably accompanied by the HER, and therefore, the development of catalysts capable of suppressing the HER and improving the NRR simultaneously is important. A Pd-hydride can help promote the hydrogenation of the intermediate *NN in the NRR process.[252] But the strong interaction between Pd and hydrogen may also block the effective reaction sites. The introduction of Cu atoms can improve the hydrogenation process and enhance the electron transfer by strong d–d orbital interactions with Pd. Along this line, the introduction of a secondary Cu to Pd was reported by Han *et al.* to obtain dual atom PdCu/NC.[252] Such a catalyst could achieve an NH_3 yield rate of *ca.* 69 μg mg^{-1} h^{-1} at −0.45 V with a high faradaic efficiency of *ca.* 24.8% in the acidic electrolyte, which outperformed the yield rate of Pd/NC by a factor of 4.2 and faradaic efficiency by 14.6 (Fig. 16d and e). Theoretical analysis disclosed that the free energy change needed for the rate-determining step of N_2 chemisorption and the following hydrogenation step could be decreased by using PdCu/NC (Fig. 16h–i). They further proved that the introduction of Cu to form PdCu/NC could not only tune the PDOS of Pd to the Fermi level (Fig. 16f), but also promote the activation of the N_2 molecule through back-donation bond formation between Pd and N_2 with an effective d-2π* coupling (Fig. 16g).

7. *In situ*/operando characterization for mechanistic investigation

As mentioned above, a better understanding of the fundamental reaction mechanism and dynamic adsorption of intermediates and catalytic site evolution is critical for catalyst design. Real-time techniques such as *in situ* Raman spectroscopy, *in situ* Fourier transform infrared spectroscopy (FTIR), on-line mass spectroscopy, operando XAS, *etc.*, could facilitate the understanding of possible phase transformation, structure reconstruction, valence state change, reaction pathways, adsorbed intermediates on active sites, *etc.* during reactions.[197,242,253–256] When combined with both theoretical and experimental results, they can provide opportunities for the mechanistic understanding of certain reactions, thus guiding the further design of electrocatalysts.

For example, through *in situ* FTIR, Lu *et al.* reported the direct observation of adsorbed intermediates on NiZn–N_6–C during CO_2RR.[240] This electrocatalyst could exhibit an earlier signal of adsorbed *CO species than that from the Ni–N_4–C and Zn–N_4–C counterparts, which indicated weaker adsorption and difficulty in producing CO for the latter ones (Fig. 17a–c). Yao *et al.* demonstrated that during CO_2RR the Ni_2–N_6 configuration could be transformed into an oxygen bridged O–Ni_2–N_6 moiety under open circuit potential and this transformation could be observed by operando XAS (Fig. 17h–i).[166] The shortened distance between Ni atoms could lead to an enhanced

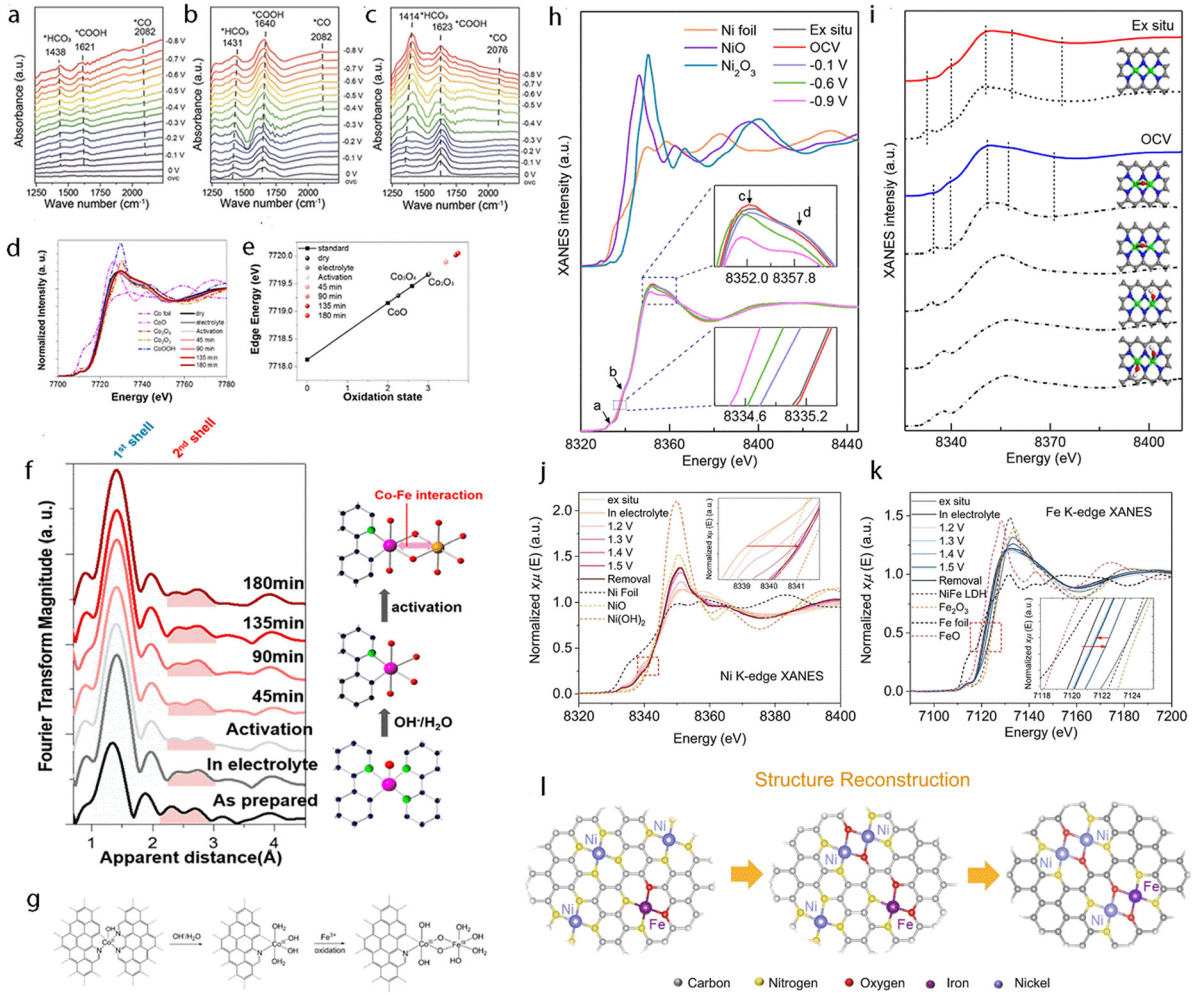

Fig. 17 (a–c) *In situ* FTIR spectra for the co-adsorption of NiZn–N_6–C (a), Ni–N_4–C (b), and Zn–N_4–C (c) in a 0.5 M $KHCO_3$ aqueous solution. Reprinted with permission.[240] Copyright 2021 Wiley-VCH GmbH. (d) XANES spectra and (e) K-edge energies (at 50% level) of XANES spectra in panel a and cobalt reference compounds containing Co(0), Co(II), or Co(III). (f) Fourier transform of Co K-edge EXAFS spectra without phase correction for as-prepared Co–N–C and the catalyst after activation as well as under OER for various durations. (g) Proposed model for the formation of a Co–Fe double-atom catalyst. After the precatalyst is immersed in the electrolyte solution, either two N or one N and one C were replaced by O. For simplicity, only the model where two N were replaced is shown. Reprinted with permission.[173] Copyright 2019 American Chemical Society. (h) Operando XANES spectra recorded at the Ni K-edge of Ni DSC, at different applied potentials from the open-circuit voltage to −0.9 V RHE during the electrocatalytic CO_2RR, and the XANES data of the referenced standards of NiO, Ni_2O_3, and Ni foil. Inset: Magnified absorption edge and white-line peak of the XANES region. (i) Comparison between the Ni K-edge XANES experimental spectra (solid lines) and the theoretical spectra (dashed lines) calculated with the depicted structures (inset). Reprinted with permission.[166] Copyright 2021 American Chemical Society. (j and k) Ni, Fe K-edge. (l) Structural reconstruction of NiFe-CNG during OER from separate Ni and Fe centers to Ni–O–Fe/Ni moieties. Reprinted with permission.[257] Copyright 2021 Springer Nature.

Ni–Ni interaction. When combined with theoretical calculations, a significantly lowered Gibbs free energy change for *COOH formation could be obtained, which explained the boosted CO_2RR activity. The structure reconstruction of active sites during reactions was also reported by Patzke *et al.* for ORR/OER (Fig. 17i and j), where the single Ni sites were easily transformed to form Ni–O–Ni and Ni–O–Fe configurations, while Fe–O–Fe was not observed during operando XAS.[257] Hu *et al.* reported another example of operando XAS measurement, used to observe the *in situ* formation of Co–Fe dual atom catalysts during the OER process (Fig. 17d–g).[173] Recently, they further disclosed the OER reaction mechanisms of a series of dual-atom electrocatalysts based on Fe, Co, and Ni SACs through a combination of operando XAS and electrokinetic measurements.[176] Take the formation of Ni–Fe–N–C as an example: the fitting result from operando Ni K-edge XAS data of the original Ni–N–C suggested a single Ni configuration coordinated with 3N, 1C, and 1O. After immersion in a 1 M KOH electrolyte, two N donors were replaced by three O donors (OH^-/H_2O). After five cyclic voltammetry scans, a new single-scattering path was found which was due to the formation of Ni–Fe dual-atoms *via* oxygen bridges. The XANES data also suggested that the oxidation state of Ni was around the range of +2 to +3 and changed little with extended electrolysis. Meanwhile, operando Fe K-edge XAS data were also collected, where the signal was only observed after one hour of electrolysis.

The oxidation state of Fe XANES data also suggested the existence of Fe(IV) species during the electrolysis. With the assistance of electrokinetic measurements, they successfully explained how hydroxyl groups, protons, and electron transfers affect the catalytic cycles of OER and proposed a possible reaction mechanism.

8. Conclusions and outlook

In this review, great emphasis has been laid on multi-atom cluster catalysts, where the origin of synergistic effects, such as optimized d-band filling, the spin state, charge difference, electronegativity, *etc.*, was discussed. The methods of modulating these parameters through effective interactions, such as inter-atomic interface, coordination environment, and substrate, were summarized. Their ability to circumvent scaling relationships and the need to develop advanced descriptors during electrocatalysis were also depicted with further discussions around the latest and well-developed synthesis methods. Following this, the recent experimental developments of such kinds of catalysts in various electrocatalytic applications (HER, OER, ORR, CO_2RR, and NRR) were reviewed, where the boosted activity compared to their SAC counterparts proved the opportunity offered by multi-atom cluster catalysts as an excellent class of electrocatalysts. Despite all the progress made, this area remains challenging to the researchers.

8.1 Maximizing the mass utilization

One of the obstacles is the relatively low mass loading of multi-atom cluster catalysts onto the substrates, which is also a pressing problem in the preparation of SACs, hampering their device-level activity. Simply increasing metal loading may not work, as most of the synthesis processes involve high-temperature pyrolysis, which may cause a severe aggregation of atomic-scale catalysts to form sub-nano clusters or nanoparticles. One solution is to enhance the interaction between the metals and the substrate to stabilize the catalysts and avoid aggregation.[245,258–260] Therefore, the use of substrates possessing plenty of functional anchoring sites to tightly bind with metal sites is likely to avoid possible aggregation. For instance, Jiang *et al.* computed that a TAC catalyst with loading as high as 35.8% could be achieved when a graphdiyne and graphene composite was introduced as the substrate.[187] The strong hybridization between the Fe-3d orbitals from the metal and the C-2p orbital from the ethynyl of the skeleton may help to stabilize the catalyst.

8.2 Precisely controlled synthesis techniques

The technique for precisely controlled synthesis of multi-atom cluster catalysts is still not mature, and therefore, their synthesis is much more challenging than that of SACs. The synthesis of catalysts with a precise structure is both meaningful and necessary. Theoretically, researchers have built plenty of models to investigate the properties of multi-atom cluster catalysts in diverse applications, but due to the limitations in the controlled synthesis of these materials, it is not easy to verify the theoretical prediction. Although the degree of atomic dispersion of the catalysts can be directly observed by HAADF-STEM and their coordination environment can be obtained from XAF spectra, their synthesis (homo- or hetero-moieties) onto substrates without introducing impurities such as SACs or nanoparticles is difficult. Some techniques such as the mass-selected deposition method have turned out to be effective to prepare such materials, but they are not easy for large-scale applications. The precursor preselection method also has its limitations and calls for a judicious selection of suitable precursors. The subsequent pyrolysis to anchor the metal catalysts onto the substrate is necessary, which makes the whole process a bit cumbersome and energy-consuming. Therefore, other reliable techniques capable of precise synthesis of multi-atom cluster catalysts are still needed.

8.3 Advanced theoretical method to simulate the real catalytic environment

The theoretical computation method is beneficial and indispensable for developing new kinds of catalysts.[261] It aids in a better understanding of the reaction mechanisms, correlates activity to the intrinsic electronic structure, accelerates the screening of effective catalysts with effective descriptors, *etc.*[250] As discussed in the review, researchers have put great efforts into the understanding of multi-atom cluster catalysts from the theoretical aspect and some credible conclusions have already been made. However, the electrochemical reactions are rather complicated. First, a given reaction may occur in between the electrode and electrolyte interface with the electrical double layer. So, the inclusion of more external conditions into the calculation system and a precise depiction of the real reaction environment are difficult but worth pursuing. Besides, although most calculations for an electrocatalytic reaction pathway rely solely on the thermodynamic states during the process, the kinetics associated with the dissociation and formation of some key intermediates are required to help the researchers understand the reactions. Moreover, even though it will be better if a model built from a computational aspect can be large enough to reflect a real reaction system as closely as possible, the calculations would still be both time and resource-consuming. So new techniques allowing researchers to study relatively large model systems should be developed.

8.4 Development of efficient descriptors and screening electrocatalysts with high activity

Finally, theoretical calculations already play an important role nowadays. They can not only help explain the reactions but also guide the design of experiments. Therefore, the universal descriptors to guide the fabrication of different catalysts are needed to better assist the screening of the optimized catalysts. Besides, the use of machine learning has also been a hot topic recently, and it will be interesting to direct some efforts in combining the concept of multi-atom cluster catalysts with machine learning to achieve more interesting progress.[262] In that case, the combination of geometrical and electronic

characteristics of electrocatalysts, such as coordination atoms, fine-tuned ligands, details about bond length, atom electronegativity, d-band center, magnetic moment, *etc.* could help build a database, which can be trained with the machine learning-based programs and screen the effective electrocatalysts.

8.5 Exploring real-time characterization techniques for mechanism understanding

The identification of catalytically active sites, the dynamic evolution behaviours, and observable reaction intermediates on multi-atom cluster catalysts during reactions with various characterization methods may help deepen the mechanistic understanding of such electrocatalysts. However, a low loading of such catalysts poses a challenge to the subsequent characterization. Therefore, the atomic scale dispersion of these catalysts requires measurements with instruments that offer high resolutions. Recently developed real-time techniques such as *in situ* FTIR, *in situ* Raman, on-line mass spectroscopy, operando XAS, *etc.*, could facilitate the observation of possible structure evolution and the real active centers, help identify valence state change, *etc.*, during reactions. Those techniques render researchers the ability to get information pertaining to the geometric and electronic characteristics of the active sites in a specific reaction, which would subsequently help guide the designing of novel electrocatalysts. While capturing the related information with an *in situ* setup to fit into diverse measuring equipment is still in its infancy, it is worth more effort.

8.6 Optimized reaction pathways and widespread applications

Multi-atom cluster catalysts can provide multiple active sites for interaction with the intermediates and help circumvent the scaling relationship with the formation of complex products, thus helping to tune the reaction pathways for certain reactions. They have demonstrated their potential in various reactions, such as glycerol hydrogenolysis,[36] oxidation of alcohols,[38] CO_2 conversions to methanol,[34] *etc.*, which require multiple reaction sites to act synergistically. While the report of multi-atom clusters towards the electrochemical catalysis to produce complex products is limited, there is one study showing the highly selective synthesis of ethanol from CO_2 on Cu_n clusters (n = 3 and 4) by involving the participation of C–C coupling from the cluster.[168] It echoes the claim made in the previous sections that multi-atom clusters may unlock the selective catalysis to obtain complex and diverse products due to the presence of multiple active sites.

In addition, more interest has been drawn toward the engineering applications of electrocatalysts. For example, in CO_2RR, significant achievements have been made with a flow cell setup. This could also provide good opportunities for the further techno-economic application of multi-atom cluster catalysts.

Conflicts of interest

There are no conflicts to declare.

Acknowledgements

This project was supported by the National Research Foundation (NRF), Prime Minister's Office, Singapore, under its Campus for Research Excellence and Technological Enterprise (CREATE) program. We also acknowledge financial support from the academic research fund AcRF tier 1 (M4012076 RG118/18), Ministry of Education, Singapore.

References

1 J. K. Nørskov, T. Bligaard, A. Logadottir, J. R. Kitchin, J. G. Chen, S. Pandelov and U. Stimming, *J. Electrochem. Soc.*, 2005, **152**, J23.
2 Y. Hori, in *Modern Aspects of Electrochemistry*, ed. C. G. Vayenas, R. E. White and M. E. Gamboa-Aldeco, Springer New York, New York, NY, 2008, pp. 89–189.
3 Y. Lee, J. Suntivich, K. J. May, E. E. Perry and Y. Shao-Horn, *J. Phys. Chem. Lett.*, 2012, **3**, 399–404.
4 E. Skúlason, T. Bligaard, S. Gudmundsdóttir, F. Studt, J. Rossmeisl, F. Abild-Pedersen, T. Vegge, H. Jónsson and J. K. Nørskov, *Phys. Chem. Chem. Phys.*, 2012, **14**, 1235–1245.
5 J. H. Montoya, C. Tsai, A. Vojvodic and J. K. Nørskov, *ChemSusChem*, 2015, **8**, 2180–2186.
6 J. Li, Y. Li and T. Zhang, *Sci. China: Mater.*, 2020, **63**, 889–891.
7 X. Li, H. Rong, J. Zhang, D. Wang and Y. Li, *Nano Res.*, 2020, **13**, 1842–1855.
8 H. Rong, S. Ji, J. Zhang, D. Wang and Y. Li, *Nat. Commun.*, 2020, **11**, 5884.
9 T. Sun, L. Xu, D. Wang and Y. Li, *Nano Res.*, 2019, **12**, 2067–2080.
10 D. Zhao, Z. Zhuang, X. Cao, C. Zhang, Q. Peng, C. Chen and Y. Li, *Chem. Soc. Rev.*, 2020, **49**, 2215–2264.
11 Y. Pan, C. Zhang, Y. Lin, Z. Liu, M. Wang and C. Chen, *Sci. China Mater.*, 2020, **63**, 921–948.
12 Z. Sun, T. Ma, H. Tao, Q. Fan and B. Han, *Chem*, 2017, **3**, 560–587.
13 S. Nitopi, E. Bertheussen, S. B. Scott, X. Liu, A. K. Engstfeld, S. Horch, B. Seger, I. E. L. Stephens, K. Chan, C. Hahn, J. K. Nørskov, T. F. Jaramillo and I. Chorkendorff, *Chem. Rev.*, 2019, **119**, 7610–7672.
14 C. J. M. van der Ham, M. T. M. Koper and D. G. H. Hetterscheid, *Chem. Soc. Rev.*, 2014, **43**, 5183–5191.
15 W. Guo, K. Zhang, Z. Liang, R. Zou and Q. Xu, *Chem. Soc. Rev.*, 2019, **48**, 5658–5716.
16 Y. C. Li, Z. Wang, T. Yuan, D.-H. Nam, M. Luo, J. Wicks, B. Chen, J. Li, F. Li, F. P. G. de Arquer, Y. Wang, C.-T. Dinh, O. Voznyy, D. Sinton and E. H. Sargent, *J. Am. Chem. Soc.*, 2019, **141**, 8584–8591.
17 X. Cui, C. Tang and Q. Zhang, *Adv. Energy Mater.*, 2018, **8**, 1800369.
18 J. Yang, W. Li, D. Wang and Y. Li, *Adv. Mater.*, 2020, **32**, 2003300.
19 A. Vasileff, C. Xu, Y. Jiao, Y. Zheng and S.-Z. Qiao, *Chem*, 2018, **4**, 1809–1831.

20 Z. W. Chen, L. X. Chen, C. C. Yang and Q. Jiang, *J. Mater. Chem. A*, 2019, **7**, 3492–3515.
21 Y. Ying, X. Luo, J. Qiao and H. Huang, *Adv. Funct. Mater.*, 2021, **31**, 2007423.
22 J. Zhang, Q.-A. Huang, J. Wang, J. Wang, J. Zhang and Y. Zhao, *Chin. J. Catal.*, 2020, **41**, 783–798.
23 S. Chen, M. Cui, Z. Yin, J. Xiong, L. Mi and Y. Li, *ChemSusChem*, 2021, **14**, 73–93.
24 S. Zhang, Y. Wu, Y.-X. Zhang and Z. Niu, *Sci. China: Chem.*, 2021, **64**, 1908–1922.
25 A. Pedersen, J. Barrio, A. Li, R. Jervis, D. J. L. Brett, M. M. Titirici and I. E. L. Stephens, *Adv. Energy Mater.*, 2022, **12**, 2102715.
26 J. Wang, C. Liu, S. Li, Y. Li, Q. Zhang, Q. Peng, J. S. Tse and Z. Wu, *Chem. Eng. J.*, 2022, **428**, 132558.
27 C. Cheng, X. Zhang, Z. Yang and Z. Zhou, *ACS Appl. Mater. Interfaces*, 2018, **10**, 32903–32912.
28 F. Li and Z. Chen, *Nanoscale*, 2018, **10**, 15696–15705.
29 F. Li, X. Liu and Z. Chen, *Small Methods*, 2019, **3**, 1800480.
30 P. Zhou, X. Hou, Y. Chao, W. Yang, W. Zhang, Z. Mu, J. Lai, F. Lv, K. Yang, Y. Liu, J. Li, J. Ma, J. Luo and S. Guo, *Chem. Sci.*, 2019, **10**, 5898–5905.
31 N. Biswakarma, P. J. Sarma, S. D. Baruah, N. K. Gour and R. C. Deka, *J. Phys. Chem. C*, 2020, **124**, 3059–3068.
32 Z. Gao, X. Liu, A. Li, X. Li, X. Ding and W. Yang, *Mol. Catal.*, 2019, **470**, 56–66.
33 B. Yang, X. Yu, A. Halder, X. Zhang, X. Zhou, G. J. A. Mannie, E. Tyo, M. J. Pellin, S. Seifert, D. Su and S. Vajda, *ACS Sustainable Chem. Eng.*, 2019, **7**, 14435–14442.
34 C. Liu, B. Yang, E. Tyo, S. Seifert, J. DeBartolo, B. von Issendorff, P. Zapol, S. Vajda and L. A. Curtiss, *J. Am. Chem. Soc.*, 2015, **137**, 8676–8679.
35 H. Li, L. Wang, Y. Dai, Z. Pu, Z. Lao, Y. Chen, M. Wang, X. Zheng, J. Zhu, W. Zhang, R. Si, C. Ma and J. Zeng, *Nat. Nanotechnol.*, 2018, **13**, 411–417.
36 X. Zhang, G. Cui, H. Feng, L. Chen, H. Wang, B. Wang, X. Zhang, L. Zheng, S. Hong and M. Wei, *Nat. Commun.*, 2019, **10**, 5812.
37 S. Tian, Q. Fu, W. Chen, Q. Feng, Z. Chen, J. Zhang, W.-C. Cheong, R. Yu, L. Gu, J. Dong, J. Luo, C. Chen, Q. Peng, C. Draxl, D. Wang and Y. Li, *Nat. Commun.*, 2018, **9**, 2353.
38 S. Ji, Y. Chen, Q. Fu, Y. Chen, J. Dong, W. Chen, Z. Li, Y. Wang, L. Gu, W. He, C. Chen, Q. Peng, Y. Huang, X. Duan, D. Wang, C. Draxl and Y. Li, *J. Am. Chem. Soc.*, 2017, **139**, 9795–9798.
39 E. Vorobyeva, E. Fako, Z. Chen, S. M. Collins, D. Johnstone, P. A. Midgley, R. Hauert, O. V. Safonova, G. Vilé, N. López, S. Mitchell and J. Pérez-Ramírez, *Angew. Chem., Int. Ed.*, 2019, **58**, 8724–8729.
40 D.-H. Xing, C.-Q. Xu, Y.-G. Wang and J. Li, *J. Phys. Chem. C*, 2019, **123**, 10494–10500.
41 C. Cui, Z. Luo and J. Yao, *CCS Chem.*, 2019, **1**, 215–225.
42 J. Fu, J. Dong, R. Si, K. Sun, J. Zhang, M. Li, N. Yu, B. Zhang, M. G. Humphrey, Q. Fu and J. Huang, *ACS Catal.*, 2021, **11**, 1952–1961.
43 C. Dong, Y. Li, D. Cheng, M. Zhang, J. Liu, Y.-G. Wang, D. Xiao and D. Ma, *ACS Catal.*, 2020, **10**, 11011–11045.
44 Z. W. Chen, J.-M. Yan and Q. Jiang, *Small Methods*, 2019, **3**, 1800291.
45 J. Wang, Z. Huang, W. Liu, C. Chang, H. Tang, Z. Li, W. Chen, C. Jia, T. Yao, S. Wei, Y. Wu and Y. Li, *J. Am. Chem. Soc.*, 2017, **139**, 17281–17284.
46 W. Ren, X. Tan, W. Yang, C. Jia, S. Xu, K. Wang, S. C. Smith and C. Zhao, *Angew. Chem., Int. Ed.*, 2019, **58**, 6972–6976.
47 L. Zhang, R. Si, H. Liu, N. Chen, Q. Wang, K. Adair, Z. Wang, J. Chen, Z. Song, J. Li, M. N. Banis, R. Li, T.-K. Sham, M. Gu, L.-M. Liu, G. A. Botton and X. Sun, *Nat. Commun.*, 2019, **10**, 4936.
48 Y. Ouyang, L. Shi, X. Bai, Q. Li and J. Wang, *Chem. Sci.*, 2020, **11**, 1807–1813.
49 M. Ma, A. Kumar, D. Wang, Y. Wang, Y. Jia, Y. Zhang, G. Zhang, Z. Yan and X. Sun, *Appl. Catal., B*, 2020, **274**, 119091.
50 M. Fan, J. Cui, J. Wu, R. Vajtai, D. Sun and P. M. Ajayan, *Small*, 2020, **16**, 1906782.
51 J. K. Nørskov, F. Studt, F. Abild-Pedersen and T. Bligaard, *Fundamental Concepts in Heterogeneous Catalysis*, 2014, pp. 155–174.
52 Y. Yang, M. Luo, W. Zhang, Y. Sun, X. Chen and S. Guo, *Chem*, 2018, **4**, 2054–2083.
53 B. Garlyyev, J. Fichtner, O. Piqué, O. Schneider, A. S. Bandarenka and F. Calle-Vallejo, *Chem. Sci.*, 2019, **10**, 8060–8075.
54 X. Zhang, A. Chen, Z. Zhang and Z. Zhou, *J. Mater. Chem. A*, 2018, **6**, 18599–18604.
55 H.-L. Jiang and Q. Xu, *J. Mater. Chem.*, 2011, **21**, 13705–13725.
56 L. Jasin Arachchige, Y. Xu, Z. Dai, X. Zhang, F. Wang and C. Sun, *J. Phys. Chem. C*, 2020, **124**, 15295–15301.
57 W. Huang and W.-X. Li, *Phys. Chem. Chem. Phys.*, 2019, **21**, 523–536.
58 M. Sankar, N. Dimitratos, P. J. Miedziak, P. P. Wells, C. J. Kiely and G. J. Hutchings, *Chem. Soc. Rev.*, 2012, **41**, 8099–8139.
59 R. Kubo, *J. Phys. Soc. Jpn.*, 1962, **17**, 975–986.
60 D. Buceta, Y. Piñeiro, C. Vázquez-Vázquez, J. Rivas and M. A. López-Quintela, *Catalysts*, 2014, **4**, 356–374.
61 J. A. Alonso, *Chem. Rev.*, 2000, **100**, 637–678.
62 V. N. Popok, I. Barke, E. E. Campbell and K. H. Meiwes-Broer, *Surf. Sci. Rep.*, 2011, **66**, 347–377.
63 L. Liu and A. Corma, *Chem. Rev.*, 2018, **118**, 4981–5079.
64 M. Xiao, H. Zhang, Y. Chen, J. Zhu, L. Gao, Z. Jin, J. Ge, Z. Jiang, S. Chen, C. Liu and W. Xing, *Nano Energy*, 2018, **46**, 396–403.
65 Y. Zhou, W. Yang, W. Utetiwabo, Y.-M. Lian, X. Yin, L. Zhou, P. Yu, R. Chen and S. Sun, *J. Phys. Chem. Lett.*, 2020, **11**, 1404–1410.
66 J. Shan, C. Ye, Y. Jiang, M. Jaroniec, Y. Zheng and S. Z. Qiao, *Sci. Adv.*, 2022, **8**, eabo0762.
67 X. Zhu, D. Zhang, C.-J. Chen, Q. Zhang, R.-S. Liu, Z. Xia, L. Dai, R. Amal and X. Lu, *Nano Energy*, 2020, **71**, 104597.
68 Y. Xu, W. Zhang, Y. Li, P. Lu, Y. Wang and Z.-S. Wu, *Front. Mater.*, 2019, 6.

69 C. Wu, X. Zhang, Z. Xia, M. Shu, H. Li, X. Xu, R. Si, A. I. Rykov, J. Wang, S. Yu, S. Wang and G. Sun, *J. Mater. Chem. A*, 2019, **7**, 14001–14010.
70 L. Chen, Y. Zhang, L. Dong, W. Yang, X. Liu, L. Long, C. Liu, S. Dong and J. Jia, *J. Mater. Chem. A*, 2020, **8**, 4369–4375.
71 F. Wang, H. Xie, T. Liu, Y. Wu and B. Chen, *Appl. Energy*, 2020, **269**, 115029.
72 R. Ku, G. Yu, J. Gao, X. Huang and W. Chen, *Phys. Chem. Chem. Phys.*, 2020, **22**, 3254–3263.
73 X. Gao, L. Mei, Y. Zhou and Z. Shen, *Nanoscale*, 2020, **12**, 7814–7821.
74 Y. Yang, H. Zhang, Z. Liang, Y. Yin, B. Mei, F. Song, F. Sun, S. Gu, Z. Jiang, Y. Wu and Z. Zhu, *J. Energy Chem.*, 2020, **44**, 131–137.
75 F. He, Z. Wang, S. Wei and J. Zhao, *Appl. Surf. Sci.*, 2020, **506**, 144943.
76 H. He, C. Morrissey, L. A. Curtiss and P. Zapol, *J. Phys. Chem. C*, 2018, **122**, 28629–28636.
77 T. Yang, S. Tang, X. Li, E. Sharman, J. Jiang and Y. Luo, *J. Phys. Chem. C*, 2018, **122**, 25441–25446.
78 G. Zhu, M. Kan, Q. Sun and P. Jena, *J. Phys. Chem. A*, 2014, **118**, 304–307.
79 G. Zheng, L. Li, Z. Tian, X. Zhang and L. Chen, *J. Energy Chem.*, 2021, **54**, 612–619.
80 H. Shen, Y. Li and Q. Sun, *J. Phys. Chem. C*, 2017, **121**, 3963–3969.
81 T. Deng, C. Cen, H. Shen, S. Wang, J. Guo, S. Cai and M. Deng, *J. Phys. Chem. Lett.*, 2020, **11**, 6320–6329.
82 Y. Zhao, S. Zhou and J. Zhao, *iScience*, 2020, **23**, 101051.
83 R. Hu, Y. Li, Q. Zeng, F. Wang and J. Shang, *ChemSusChem*, 2020, **13**, 3636–3644.
84 W. Pei, S. Zhou, J. Zhao, X. Xu, Y. Du and S. X. Dou, *Nano Energy*, 2020, **76**, 105049.
85 R. Guo, M. Hu, W. Zhang and J. He, *Molecules*, 2019, **24**, 1777.
86 C. Hu, Y. Wang, J. Chen, H. F. Wang, K. Shen, K. Tang, L. Chen and Y. Li, *Small*, 2022, 2201391.
87 X. Li, W. Zhong, P. Cui, J. Li and J. Jiang, *J. Phys. Chem. Lett.*, 2016, **7**, 1750–1755.
88 G. Yang, J. Zhu, P. Yuan, Y. Hu, G. Qu, B.-A. Lu, X. Xue, H. Yin, W. Cheng, J. Cheng, W. Xu, J. Li, J. Hu, S. Mu and J.-N. Zhang, *Nat. Commun.*, 2021, **12**, 1734.
89 M. A. Hunter, J. M. T. A. Fischer, Q. Yuan, M. Hankel and D. J. Searles, *ACS Catal.*, 2019, **9**, 7660–7667.
90 Y. Sun, J. Wang, Q. Liu, M. Xia, Y. Tang, F. Gao, Y. Hou, J. Tse and Y. Zhao, *J. Mater. Chem. A*, 2019, **7**, 27175–27185.
91 J. Zhao, J. Zhao, F. Li and Z. Chen, *J. Phys. Chem. C*, 2018, **122**, 19712–19721.
92 Y. Meng, C. Yin, K. Li, H. Tang, Y. Wang and Z. Wu, *ACS Sustainable Chem. Eng.*, 2019, **7**, 17273–17281.
93 T. He, A. R. Puente Santiago and A. Du, *J. Catal.*, 2020, **388**, 77–83.
94 Y. Zhu, J. Sokolowski, X. Song, Y. He, Y. Mei and G. Wu, *Adv. Energy Mater.*, 2020, **10**, 1902844.
95 X. Li, L. Liu, X. Ren, J. Gao, Y. Huang and B. Liu, *Sci. Adv.*, 2020, **6**, eabb6833.
96 Y. Pan, C. Zhang, Z. Liu, C. Chen and Y. Li, *Matter*, 2020, **2**, 78–110.
97 Y. Li, H. Su, S. H. Chan and Q. Sun, *ACS Catal.*, 2015, **5**, 6658–6664.
98 D. Ma, Z. Zeng, L. Liu, X. Huang and Y. Jia, *J. Phys. Chem. C*, 2019, **123**, 19066–19076.
99 E. F. Holby and C. D. Taylor, *Sci. Rep.*, 2015, **5**, 9286.
100 J. Wang, S. Dou and X. Wang, *Sci. Adv.*, 2021, **13**, eabf3989.
101 D. Liu, B. Wang, H. Li, S. Huang, M. Liu, J. Wang, Q. Wang, J. Zhang and Y. Zhao, *Nano Energy*, 2019, **58**, 277–283.
102 B. Wang, J. Zou, X. Shen, Y. Yang, G. Hu, W. Li, Z. Peng, D. Banham, A. Dong and D. Zhao, *Nano Energy*, 2019, **63**, 103851.
103 M. A. Hunter, J. M. T. A. Fischer, M. Hankel, Q. Yuan and D. J. Searles, *J. Chem. Inf. Model.*, 2019, **59**, 2242–2247.
104 X. Zhao, X. Liu, B. Huang, P. Wang and Y. Pei, *J. Mater. Chem. A*, 2019, **7**, 24583–24593.
105 M. Xiao, Y. Chen, J. Zhu, H. Zhang, X. Zhao, L. Gao, X. Wang, J. Zhao, J. Ge, Z. Jiang, S. Chen, C. Liu and W. Xing, *J. Am. Chem. Soc.*, 2019, **141**, 17763–17770.
106 Q. Huang, H. Liu, W. An, Y. Wang, Y. Feng and Y. Men, *ACS Sustainable Chem. Eng.*, 2019, **7**, 19113–19121.
107 Y. Meng, K. Li, D. Xiao, Y. Yuan, Y. Wang and Z. Wu, *Int. J. Hydrogen Energy*, 2020, **45**, 14311–14319.
108 X. Bai, Q. Li, L. Shi, X. Niu, C. Ling and J. Wang, *Small*, 2020, **16**, 1901981.
109 Z. Liang, M. Luo, M. Chen, C. Liu, S. G. Peera, X. Qi, J. Liu, U. P. Kumar and T. L. T. Liang, *J. Colloid Interface Sci.*, 2020, **568**, 54–62.
110 Y. Meng, C. Yin, K. Li, H. Tang, Y. Wang and Z. Wu, *Appl. Surf. Sci.*, 2019, **480**, 905–911.
111 H. Zhang, C. Cui and Z. Luo, *J. Phys. Chem. C*, 2020, **124**, 6260–6266.
112 Y. Zhao, K. R. Yang, Z. Wang, X. Yan, S. Cao, Y. Ye, Q. Dong, X. Zhang, J. E. Thorne, L. Jin, K. L. Materna, A. Trimpalis, H. Bai, S. C. Fakra, X. Zhong, P. Wang, X. Pan, J. Guo, M. Flytzani-Stephanopoulos, G. W. Brudvig, V. S. Batista and D. Wang, *Proc. Natl. Acad. Sci. U. S. A.*, 2018, **115**, 2902–2907.
113 W. Yang, H. Huang, X. Ding, Z. Ding, C. Wu, I. D. Gates and Z. Gao, *Electrochim. Acta*, 2020, **335**, 135667.
114 J. Liu, D. Cao, H. Xu and D. Cheng, *Nano Sel.*, 2021, **2**, 251–270.
115 C.-C. Hou, H.-F. Wang, C. Li and Q. Xu, *Energy Environ. Sci.*, 2020, **13**, 1658–1693.
116 E. Guan, J. Ciston, S. R. Bare, R. C. Runnebaum, A. Katz, A. Kulkarni, C. X. Kronawitter and B. C. Gates, *ACS Catal.*, 2020, **10**, 9065–9085.
117 Z. He, K. He, A. W. Robertson, A. I. Kirkland, D. Kim, J. Ihm, E. Yoon, G.-D. Lee and J. H. Warner, *Nano Lett.*, 2014, **14**, 3766–3772.
118 J.-C. Liu, X.-L. Ma, Y. Li, Y.-G. Wang, H. Xiao and J. Li, *Nat. Commun.*, 2018, **9**, 1610.
119 A. A. Peterson, F. Abild-Pedersen, F. Studt, J. Rossmeisl and J. K. Nørskov, *Energy Environ. Sci.*, 2010, **3**, 1311–1315.
120 A. A. Peterson and J. K. Nørskov, *J. Phys. Chem. Lett.*, 2012, **3**, 251–258.

121 M. T. M. Koper, *Chem. Sci.*, 2013, **4**, 2710–2723.
122 J. K. Nørskov, J. Rossmeisl, A. Logadottir, L. Lindqvist, J. R. Kitchin, T. Bligaard and H. Jónsson, *J. Phys. Chem. B*, 2004, **108**, 17886–17892.
123 M. Che, *Catal. Today*, 2013, **218–219**, 162–171.
124 J. K. Nørskov, T. Bligaard, J. Rossmeisl and C. H. Christensen, *Nat. Chem.*, 2009, **1**, 37–46.
125 J. Suntivich, H. A. Gasteiger, N. Yabuuchi, H. Nakanishi, J. B. Goodenough and Y. Shao-Horn, *Nat. Chem.*, 2011, **3**, 546–550.
126 H. Xu, D. Cheng, D. Cao and X. C. Zeng, *Nat. Catal.*, 2018, **1**, 339–348.
127 F. Abild-Pedersen, J. Greeley, F. Studt, J. Rossmeisl, T. R. Munter, P. G. Moses, E. Skúlason, T. Bligaard and J. K. Nørskov, *Phys. Rev. Lett.*, 2007, **99**, 016105.
128 G. Lendvay, *J. Phys. Chem.*, 1989, **93**, 4422–4429.
129 J. Rossmeisl, A. Logadottir and J. K. Nørskov, *Chem. Phys.*, 2005, **319**, 178–184.
130 Z. Xu, J. Rossmeisl and J. R. Kitchin, *J. Phys. Chem. C*, 2015, **119**, 4827–4833.
131 E. M. Fernández, P. G. Moses, A. Toftelund, H. A. Hansen, J. I. Martínez, F. Abild-Pedersen, J. Kleis, B. Hinnemann, J. Rossmeisl, T. Bligaard and J. K. Nørskov, *Angew. Chem., Int. Ed.*, 2008, **47**, 4683–4686.
132 Z. W. Seh, J. Kibsgaard, C. F. Dickens, I. Chorkendorff, J. K. Nørskov and T. F. Jaramillo, *Science*, 2017, **355**, eaad4998.
133 T. Bligaard, J. K. Nørskov, S. Dahl, J. Matthiesen, C. H. Christensen and J. Sehested, *J. Catal.*, 2004, **224**, 206–217.
134 A. Vojvodic and J. K. Nørskov, *Natl. Sci. Rev.*, 2015, **2**, 140–143.
135 J. Greeley, *Annu. Rev. Chem. Biomol. Eng.*, 2016, **7**, 605–635.
136 M. T. Darby, M. Stamatakis, A. Michaelides and E. C. H. Sykes, *J. Phys. Chem. Lett.*, 2018, **9**, 5636–5646.
137 M. Andersen, A. J. Medford, J. K. Nørskov and K. Reuter, *ACS Catal.*, 2017, **7**, 3960–3967.
138 M. J. Craig, G. Coulter, E. Dolan, J. Soriano-López, E. Mates-Torres, W. Schmitt and M. García-Melchor, *Nat. Commun.*, 2019, **10**, 4993.
139 Z.-F. Huang, J. Song, S. Dou, X. Li, J. Wang and X. Wang, *Matter*, 2019, **1**, 1494–1518.
140 T. Sours, A. Patel, J. Nørskov, S. Siahrostami and A. Kulkarni, *J. Phys. Chem. Lett.*, 2020, **11**, 10029–10036.
141 G. Luo, Y. Jing and Y. Li, *J. Mater. Chem. A*, 2020, **8**, 15809–15815.
142 Y. Qian, Y. Liu, Y. Zhao, X. Zhang and G. Yu, *EcoMat*, 2020, **2**, e12014.
143 L. Li, K. Yuan and Y. Chen, *Acc. Mater. Res.*, 2022, **3**, 584–596.
144 L. Gong, D. Zhang, Y. Shen, X. Wang, J. Zhang, X. Han, L. Zhang and Z. Xia, *J. Catal.*, 2020, **390**, 126–134.
145 L. Wu, T. Guo and T. Li, *Adv. Funct. Mater.*, 2022, 2203439.
146 Z. F. Huang, J. Song, S. Dou, X. Li, J. Wang and X. Wang, *Matter*, 2019, 1494–1519.
147 V. Viswanathan, H. A. Hansen, J. Rossmeisl and J. K. Nørskov, *ACS Catal.*, 2012, **2**, 1654–1660.
148 A. Nilsson and L. G. M. Pettersson, in *Chemical Bonding at Surfaces and Interfaces*, ed. A. Nilsson, L. G. M. Pettersson and J. K. Nørskov, Elsevier, Amsterdam, 2008, pp. 57–142.
149 B. Hammer and J. K. Norskov, *Nature*, 1995, **376**, 238–240.
150 V. Stamenkovic, B. S. Mun, K. J. J. Mayrhofer, P. N. Ross, N. M. Markovic, J. Rossmeisl, J. Greeley and J. K. Nørskov, *Angew. Chem., Int. Ed.*, 2006, **45**, 2897–2901.
151 V. R. Stamenkovic, B. Fowler, B. S. Mun, G. Wang, P. N. Ross, C. A. Lucas and N. M. Marković, *Science*, 2007, **315**, 493–497.
152 V. R. Stamenkovic, B. S. Mun, M. Arenz, K. J. J. Mayrhofer, C. A. Lucas, G. Wang, P. N. Ross and N. M. Markovic, *Nat. Mater.*, 2007, **6**, 241–247.
153 J. H. Montoya, A. D. Doyle, J. K. Nørskov and A. Vojvodic, *Phys. Chem. Chem. Phys.*, 2018, **20**, 3813–3818.
154 J. Suntivich, K. J. May, H. A. Gasteiger, J. B. Goodenough and Y. Shao-Horn, *Science*, 2011, **334**, 1383–1385.
155 R. Chattot, O. Le Bacq, V. Beermann, S. Kühl, J. Herranz, S. Henning, L. Kühn, T. Asset, L. Guétaz, G. Renou, J. Drnec, P. Bordet, A. Pasturel, A. Eychmüller, T. J. Schmidt, P. Strasser, L. Dubau and F. Maillard, *Nat. Mater.*, 2018, **17**, 827–833.
156 H. B. Tao, L. Fang, J. Chen, H. B. Yang, J. Gao, J. Miao, S. Chen and B. Liu, *J. Am. Chem. Soc.*, 2016, **138**, 9978–9985.
157 X. Guan, W. Gao and Q. Jiang, *J. Mater. Chem. A*, 2021, **9**, 4770–4780.
158 X. Guo, J. Gu, S. Lin, S. Zhang, Z. Chen and S. Huang, *J. Am. Chem. Soc.*, 2020, **142**, 5709–5721.
159 C. Jia, Q. Wang, J. Yang, K. Ye, X. Li, W. Zhong, H. Shen, E. Sharman, Y. Luo and J. Jiang, *ACS Catal.*, 2022, **12**, 3420–3429.
160 H. Li, Z. Zhao, Q. Cai, L. Yin and J. Zhao, *J. Mater. Chem. A*, 2020, **8**, 4533–4543.
161 X. Liu, Y. Jiao, Y. Zheng, K. Davey and S.-Z. Qiao, *J. Mater. Chem. A*, 2019, **7**, 3648–3654.
162 C. Zhu, M. Wang, C. Wen, M. Zhang, Y. Geng, G. Zhu and Z. Su, *Adv. Sci.*, 2022, **9**, 2105697.
163 H. Chen, Y. Zhang, Q. He, H. Zhang, S. Xu, X. He and H. Ji, *J. Mater. Chem. A*, 2020, **8**, 2364–2368.
164 W. Ye, S. Chen, Y. Lin, L. Yang, S. Chen, X. Zheng, Z. Qi, C. Wang, R. Long, M. Chen, J. Zhu, P. Gao, L. Song, J. Jiang and Y. Xiong, *Chem*, 2019, **5**, 2865–2878.
165 Y.-S. Wei, L. Sun, M. Wang, J. Hong, L. Zou, H. Liu, Y. Wang, M. Zhang, Z. Liu, Y. Li, S. Horike, K. Suenaga and Q. Xu, *Angew. Chem., Int. Ed.*, 2020, **59**, 16013–16022.
166 T. Ding, X. Liu, Z. Tao, T. Liu, T. Chen, W. Zhang, X. Shen, D. Liu, S. Wang, B. Pang, D. Wu, L. Cao, L. Wang, T. Liu, Y. Li, H. Sheng, M. Zhu and T. Yao, *J. Am. Chem. Soc.*, 2021, **143**, 11317–11324.
167 X. Han, X. Ling, D. Yu, D. Xie, L. Li, S. Peng, C. Zhong, N. Zhao, Y. Deng and W. Hu, *Adv. Mater.*, 2019, **31**, 1905622.
168 H. Xu, D. Rebollar, H. He, L. Chong, Y. Liu, C. Liu, C.-J. Sun, T. Li, J. V. Muntean, R. E. Winans, D.-J. Liu and T. Xu, *Nat. Energy*, 2020, **5**, 623–632.
169 J. Jiao, R. Lin, S. Liu, W.-C. Cheong, C. Zhang, Z. Chen, Y. Pan, J. Tang, K. Wu, S.-F. Hung, H. M. Chen, L. Zheng,

Q. Lu, X. Yang, B. Xu, H. Xiao, J. Li, D. Wang, Q. Peng, C. Chen and Y. Li, *Nat. Chem.*, 2019, **11**, 222–228.
170 Y.-F. Lu, L.-Z. Dong, J. Liu, R.-X. Yang, J.-J. Liu, Y. Zhang, L. Zhang, Y.-R. Wang, S.-L. Li and Y.-Q. Lan, *Angew. Chem., Int. Ed.*, 2021, **60**, 26210–26217.
171 W. Rong, H. Zou, W. Zang, S. Xi, S. Wei, B. Long, J. Hu, Y. Ji and L. Duan, *Angew. Chem., Int. Ed.*, 2021, **60**, 466–472.
172 N. Zhang, X. Zhang, Y. Kang, C. Ye, R. Jin, H. Yan, R. Lin, J. Yang, Q. Xu, Y. Wang, Q. Zhang, L. Gu, L. Liu, W. Song, J. Liu, D. Wang and Y. Li, *Angew. Chem., Int. Ed.*, 2021, **60**, 13388–13393.
173 L. Bai, C.-S. Hsu, D. T. L. Alexander, H. M. Chen and X. Hu, *J. Am. Chem. Soc.*, 2019, **141**, 14190–14199.
174 M. Li, K. Duanmu, C. Wan, T. Cheng, L. Zhang, S. Dai, W. Chen, Z. Zhao, P. Li, H. Fei, Y. Zhu, R. Yu, J. Luo, K. Zang, Z. Lin, M. Ding, J. Huang, H. Sun, J. Guo, X. Pan, W. A. Goddard, P. Sautet, Y. Huang and X. Duan, *Nat. Catal.*, 2019, **2**, 495–503.
175 J.-C. Liu, H. Xiao and J. Li, *J. Am. Chem. Soc.*, 2020, **142**, 3375–3383.
176 L. Bai, C.-S. Hsu, D. T. L. Alexander, H. M. Chen and X. Hu, *Nat. Energy*, 2021, **6**, 1054–1066.
177 L. Zhang, J. M. T. A. Fischer, Y. Jia, X. Yan, W. Xu, X. Wang, J. Chen, D. Yang, H. Liu, L. Zhuang, M. Hankel, D. J. Searles, K. Huang, S. Feng, C. L. Brown and X. Yao, *J. Am. Chem. Soc.*, 2018, **140**, 10757–10763.
178 L. Zhang, Y. Jia, H. Liu, L. Zhuang, X. Yan, C. Lang, X. Wang, D. Yang, K. Huang, S. Feng and X. Yao, *Angew. Chem., Int. Ed.*, 2019, **58**, 9404–9408.
179 J. Wang, L. Gan, W. Zhang, Y. Peng, H. Yu, Q. Yan, X. Xia and X. Wang, *Sci. Adv.*, 2018, **4**, eaap7970.
180 H. Yan, Y. Lin, H. Wu, W. Zhang, Z. Sun, H. Cheng, W. Liu, C. Wang, J. Li, X. Huang, T. Yao, J. Yang, S. Wei and J. Lu, *Nat. Commun.*, 2017, **8**, 1070.
181 X. Cao, L. Zhao, B. Wulan, D. Tan, Q. Chen, J. Ma and J. Zhang, *Angew. Chem., Int. Ed.*, 2022, **61**, e202113918.
182 H. Wang, X. Wang, J. Pan, L. Zhang, M. Zhao, J. Xu, B. Liu, W. Shi, S. Song and H. Zhang, *Angew. Chem., Int. Ed.*, 2021, **60**, 23154–23158.
183 Y. Wu, C. Ye, L. Yu, Y. Liu, J. Huang, J. Bi, L. Xue, J. Sun, J. Yang, W. Zhang, X. Wang, P. Xiong and J. Zhu, *Energy Storage Mater.*, 2022, **45**, 805–813.
184 M. Jiang, F. Wang, F. Yang, H. He, J. Yang, W. Zhang, J. Luo, J. Zhang and C. Fu, *Nano Energy*, 2022, **93**, 106793.
185 X. He, Y. Deng, Y. Zhang, Q. He, D. Xiao, M. Peng, Y. Zhao, H. Zhang, R. Luo, T. Gan, H. Ji and D. Ma, *Cell Rep. Phys. Sci.*, 2020, **1**, 100004.
186 Y. Lei, F. Mehmood, S. Lee, J. Greeley, B. Lee, S. Seifert, R. E. Winans, J. W. Elam, R. J. Meyer, P. C. Redfern, D. Teschner, R. Schlögl, M. J. Pellin, L. A. Curtiss and S. Vajda, *Science*, 2010, **328**, 224–228.
187 Z. W. Chen, L. Chen, M. Jiang, D. Chen, Z. Wang, X. Yao, C. V. Singh and Q. Jiang, *J. Mater. Chem. A*, 2020, **8**, 15086–15093.
188 X. Li, X. Yang, J. Zhang, Y. Huang and B. Liu, *ACS Catal.*, 2019, **9**, 2521–2531.
189 J. Li and J. Gong, *Energy Environ. Sci.*, 2020, **13**, 3748–3779.
190 D. S. Su, B. Zhang and R. Schlögl, *Chem. Rev.*, 2015, **115**, 2818–2882.
191 Z. Wang, X. Jin, C. Zhu, Y. Liu, H. Tan, R. Ku, Y. Zhang, L. Zhou, Z. Liu, S.-J. Hwang and H. J. Fan, *Adv. Mater.*, 2021, **33**, 2104718.
192 J. Timoshenko and B. Roldan Cuenya, *Chem. Rev.*, 2021, **121**, 882–961.
193 M. Xiao, J. Zhu, S. Li, G. Li, W. Liu, Y.-P. Deng, Z. Bai, L. Ma, M. Feng, T. Wu, D. Su, J. Lu, A. Yu and Z. Chen, *ACS Catal.*, 2021, **11**, 8837–8846.
194 W. L. Bragg, *Proc. Math. Phys.*, 1913, **89**, 248–277.
195 F. A. Stevie and C. L. Donley, *J. Vac. Sci. Technol.*, 2020, **38**, 063204.
196 X. Peng, H.-X. Liu, Y. Zhang, Z.-Q. Huang, L. Yang, Y. Jiang, X. Wang, L. Zheng, C. Chang, C.-T. Au, L. Jiang and J. Li, *Chem. Sci.*, 2021, **12**, 7125–7137.
197 X. Li, H.-Y. Wang, H. Yang, W. Cai, S. Liu and B. Liu, *Small Methods*, 2018, **2**, 1700395.
198 G. Gourdin and V. Doan-Nguyen, *Cell Rep. Phys. Sci.*, 2021, **2**, 100660.
199 H. T. Chung, D. A. Cullen, D. Higgins, B. T. Sneed, E. F. Holby, K. L. More and P. Zelenay, *Science*, 2017, **357**, 479–484.
200 Z. Weng, Y. Wu, M. Wang, J. Jiang, K. Yang, S. Huo, X. F. Wang, Q. Ma, G. W. Brudvig, V. S. Batista and Y. Liang, *Nat. Commun.*, 2018, **9**, 1–9.
201 D. H. Nam, O. S. Bushuyev, J. Li, P. De Luna, A. Seifitokaldani, C. T. Dinh, F. P. García de Arquer, Y. Wang, Z. Liang, A. H. Proppe and C. S. Tan, *J. Am. Chem. Soc.*, 2018, **140**, 11378–11386.
202 S. Liu, H. B. Yang, S. F. Hung, J. Ding, W. Cai, L. Liu, J. Gao, X. Li, X. Ren, Z. Kuang and Y. Huang, *Angew. Chem., Int. Ed.*, 2020, **59**, 798–803.
203 E. Martínez-Periñán, M. Revenga-Parra, J. Pastore, F. Pariente, F. Zamora, O. Castillo, E. Lorenzo and H. D. Abruña, *J. Phys. Chem. C*, 2018, **122**, 12377–12383.
204 C. J. Chang, S. F. Hung, C. S. Hsu, H. C. Chen, S. C. Lin, Y. F. Liao and H. M. Chen, *ACS Cent. Sci.*, 2019, **5**, 1998–2009.
205 F. Li, Y. C. Li, Z. Wang, J. Li, D. H. Nam, Y. Lum, M. Luo, X. Wang, A. Ozden, S. F. Hung and B. Chen, *Nat. Catal.*, 2020, **3**, 75–82.
206 J. Gu, C. S. Hsu, L. Bai, H. M. Chen and X. Hu, *Science*, 2019, **364**, 1091–1094.
207 Z. Chen, S. Jiang, G. Kang, D. Nguyen, G. C. Schatz and R. P. Van Duyne, *J. Am. Chem. Soc.*, 2019, **141**, 15684–15692.
208 K. Yang, R. Kas and W. A. Smith, *J. Am. Chem. Soc.*, 2019, **141**, 15891–15900.
209 S. Zhu, T. Li, W. B. Cai and M. Shao, *ACS Energy Lett.*, 2019, **4**, 682–689.
210 T. Chao, X. Luo, W. Chen, B. Jiang, J. Ge, Y. Lin, G. Wu, X. Wang, Y. Hu, Z. Zhuang, Y. Wu, X. Hong and Y. Li, *Angew. Chem., Int. Ed.*, 2017, **56**, 16047–16051.
211 X. Zeng, J. Shui, X. Liu, Q. Liu, Y. Li, J. Shang, L. Zheng and R. Yu, *Adv. Energy Mater.*, 2018, **8**, 1701345.

212 Y. Zhou, E. Song, W. Chen, C. U. Segre, J. Zhou, Y.-C. Lin, C. Zhu, R. Ma, P. Liu, S. Chu, T. Thomas, M. Yang, Q. Liu, K. Suenaga, Z. Liu, J. Liu and J. Wang, *Adv. Mater.*, 2020, **32**, 2003484.
213 A. Kumar, V. Q. Bui, J. Lee, L. Wang, A. R. Jadhav, X. Liu, X. Shao, Y. Liu, J. Yu, Y. Hwang, H. T. D. Bui, S. Ajmal, M. G. Kim, S.-G. Kim, G.-S. Park, Y. Kawazoe and H. Lee, *Nat. Commun.*, 2021, **12**, 6766.
214 Y. Yang, Y. Qian, H. Li, Z. Zhang, Y. Mu, D. Do, B. Zhou, J. Dong, W. Yan, Y. Qin, L. Fang, R. Feng, J. Zhou, P. Zhang, J. Dong, G. Yu, Y. Liu, X. Zhang and X. Fan, *Sci. Adv.*, 2020, **6**, eaba6586.
215 S.-H. Yin, J. Yang, Y. Han, G. Li, L.-Y. Wan, Y.-H. Chen, C. Chen, X.-M. Qu, Y.-X. Jiang and S.-G. Sun, *Angew. Chem., Int. Ed.*, 2020, **59**, 22160–22163.
216 G. Zhang, Y. Jia, C. Zhang, X. Xiong, K. Sun, R. Chen, W. Chen, Y. Kuang, L. Zheng, H. Tang, W. Liu, J. Liu, X. Sun, W.-F. Lin and H. Dai, *Energy Environ. Sci.*, 2019, **12**, 1317–1325.
217 F. Kong, R. Si, N. Chen, Q. Wang, J. Li, G. Yin, M. Gu, J. Wang, L.-M. Liu and X. Sun, *Appl. Catal., B*, 2022, **301**, 120782.
218 J. Wang, W. Liu, G. Luo, Z. Li, C. Zhao, H. Zhang, M. Zhu, Q. Xu, X. Wang, C. Zhao, Y. Qu, Z. Yang, T. Yao, Y. Li, Y. Lin, Y. Wu and Y. Li, *Energy Environ. Sci.*, 2018, **11**, 3375–3379.
219 Z. Lu, B. Wang, Y. Hu, W. Liu, Y. Zhao, R. Yang, Z. Li, J. Luo, B. Chi, Z. Jiang, M. Li, S. Mu, S. Liao, J. Zhang and X. Sun, *Angew. Chem., Int. Ed.*, 2019, **131**, 2648–2652.
220 S. Li, C. Cheng, X. Zhao, J. Schmidt and A. Thomas, *Angew. Chem., Int. Ed.*, 2018, **57**, 1856–1862.
221 J. Zang, F. Wang, Q. Cheng, G. Wang, L. Ma, C. Chen, L. Yang, Z. Zou, D. Xie and H. Yang, *J. Mater. Chem. A*, 2020, **8**, 3686–3691.
222 Y. Chen, S. Hu, F. Nichols, F. Bridges, S. Kan, T. He, Y. Zhang and S. Chen, *J. Mater. Chem. A*, 2020, **8**, 11649–11655.
223 Y.-j Wu, X.-h Wu, T.-x Tu, P.-f Zhang, J.-t Li, Y. Zhou, L. Huang and S.-g Sun, *Appl. Catal., B*, 2020, **278**, 119259.
224 J. Xu, S. Lai, D. Qi, M. Hu, X. Peng, Y. Liu, W. Liu, G. Hu, H. Xu, F. Li, C. Li, J. He, L. Zhuo, J. Sun, Y. Qiu, S. Zhang, J. Luo and X. Liu, *Nano Res.*, 2021, **14**, 1374–1381.
225 Y. Wang, Z. Li, P. Zhang, Y. Pan, Y. Zhang, Q. Cai, S. R. P. Silva, J. Liu, G. Zhang, X. Sun and Z. Yan, *Nano Energy*, 2021, **87**, 106147.
226 T. Cui, Y.-P. Wang, T. Ye, J. Wu, Z. Chen, J. Li, Y. Lei, D. Wang and Y. Li, *Angew. Chem., Int. Ed.*, 2022, **61**, e202115219.
227 Y. He, X. Yang, Y. Li, L. Liu, S. Guo, C. Shu, F. Liu, Y. Liu, Q. Tan and G. Wu, *ACS Catal.*, 2022, **12**, 1216–1227.
228 M. Liu, N. Li, S. Cao, X. Wang, X. Lu, L. Kong, Y. Xu and X.-H. Bu, *Adv. Mater.*, 2022, **34**, 2107421.
229 Y. Li, C. Chen, R. Cao, Z. Pan, H. He and K. Zhou, *Appl. Catal., B*, 2020, **268**, 118747.
230 R. Yun, F. Zhan, X. Wang, B. Zhang, T. Sheng, Z. Xin, J. Mao, S. Liu and B. Zheng, *Small*, 2021, **17**, 2006951.
231 W. Xie, H. Li, G. Cui, J. Li, Y. Song, S. Li, X. Zhang, J. Y. Lee, M. Shao and M. Wei, *Angew. Chem., Int. Ed.*, 2021, **60**, 7382–7388.
232 L. Lin, H. Li, C. Yan, H. Li, R. Si, M. Li, J. Xiao, G. Wang and X. Bao, *Adv. Mater.*, 2019, **31**, 1903470.
233 H. Cheng, X. Wu, M. Feng, X. Li, G. Lei, Z. Fan, D. Pan, F. Cui and G. He, *ACS Catal.*, 2021, **11**, 12673–12681.
234 J. Zhu, M. Xiao, D. Ren, R. Gao, X. Liu, Z. Zhang, D. Luo, W. Xing, D. Su, A. Yu and Z. Chen, *J. Am. Chem. Soc.*, 2022, **144**, 9661–9671.
235 L. Qin, F. Sun, X. Ma, G. Ma, Y. Tang, L. Wang, Q. Tang, R. Jin and Z. Tang, *Angew. Chem., Int. Ed.*, 2021, **60**, 26136–26141.
236 J. Hao, Z. Zhuang, J. Hao, C. Wang, S. Lu, F. Duan, F. Xu, M. Du and H. Zhu, *Adv. Energy Mater.*, 2022, 2200579.
237 L. Jiao, J. Zhu, Y. Zhang, W. Yang, S. Zhou, A. Li, C. Xie, X. Zheng, W. Zhou, S.-H. Yu and H.-L. Jiang, *J. Am. Chem. Soc.*, 2021, **143**, 19417–19424.
238 M. Feng, X. Wu, H. Cheng, Z. Fan, X. Li, F. Cui, S. Fan, Y. Dai, G. Lei and G. He, *J. Mater. Chem. A*, 2021, **9**, 23817–23827.
239 L. J. Liu, Z. Y. Wang, Z. Y. Wang, R. Wang, S. Q. Zang and T. C. Mak, *Angew. Chem., Int. Ed.*, 2022, **61**, e2022056.
240 Y. Li, B. Wei, M. Zhu, J. Chen, Q. Jiang, B. Yang, Y. Hou, L. Lei, Z. Li, R. Zhang and Y. Lu, *Adv. Mater.*, 2021, **33**, 2102212.
241 Z. Zeng, L. Y. Gan, H. Bin Yang, X. Su, J. Gao, W. Liu, H. Matsumoto, J. Gong, J. Zhang, W. Cai, Z. Zhang, Y. Yan, B. Liu and P. Chen, *Nat. Commun.*, 2021, **12**, 4088.
242 X. Su, Z. Jiang, J. Zhou, H. Liu, D. Zhou, H. Shang, X. Ni, Z. Peng, F. Yang, W. Chen, Z. Qi, D. Wang and Y. Wang, *Nat. Commun.*, 2022, **13**, 1322.
243 Z. Weng, Y. Wu, M. Wang, J. Jiang, K. Yang, S. Huo, X.-F. Wang, Q. Ma, G. W. Brudvig, V. S. Batista, Y. Liang, Z. Feng and H. Wang, *Nat. Commun.*, 2018, **9**, 415.
244 D. Karapinar, N. T. Huan, N. Ranjbar Sahraie, J. Li, D. Wakerley, N. Touati, S. Zanna, D. Taverna, L. H. Galvão Tizei, A. Zitolo, F. Jaouen, V. Mougel and M. Fontecave, *Angew. Chem., Int. Ed.*, 2019, **58**, 15098–15103.
245 Y. Wu, C. He and W. Zhang, *ACS Appl. Mater. Interfaces*, 2021, **13**, 47520–47529.
246 J.-C. Chen, H. Cao, J.-W. Chen, S.-J. Qian, G.-J. Xia, Y.-G. Wang and J. Li, *J. Phys. Chem. C*, 2021, **125**, 19821–19830.
247 Y. Wu, C. He and W. Zhang, *J. Am. Chem. Soc.*, 2022, **144**, 9344–9353.
248 Y. Li, Q. Zhang, C. Li, H.-N. Fan, W.-B. Luo, H.-K. Liu and S.-X. Dou, *J. Mater. Chem. A*, 2019, **7**, 22242–22247.
249 P. Saha, S. Amanullah and A. Dey, *J. Am. Chem. Soc.*, 2020, **142**, 17312–17317.
250 C. Yao, N. Guo, S. Xi, C.-Q. Xu, W. Liu, X. Zhao, J. Li, H. Fang, J. Su, Z. Chen, H. Yan, Z. Qiu, P. Lyu, C. Chen, H. Xu, X. Peng, X. Li, B. Liu, C. Su, S. J. Pennycook, C.-J. Sun, J. Li, C. Zhang, Y. Du and J. Lu, *Nat. Commun.*, 2020, **11**, 4389.
251 X. Wang, S. Qiu, J. Feng, Y. Tong, F. Zhou, Q. Li, L. Song, S. Chen, K.-H. Wu, P. Su, S. Ye, F. Hou, S. X. Dou, H. K. Liu, G. Q. Lu, C. Sun, J. Liu and J. Liang, *Adv. Mater.*, 2020, **32**, 2004382.

252 L. Han, Z. Ren, P. Ou, H. Cheng, N. Rui, L. Lin, X. Liu, L. Zhuo, J. Song, J. Sun, J. Luo and H. L. Xin, *Angew. Chem., Int. Ed.*, 2020, **60**, 345–350.
253 K. S. Adarsh, N. Chandrasekaran and V. Chakrapani, *Front. Chem.*, 2020, **8**, 137.
254 L. Jin and A. Seifitokaldani, *Catalysts*, 2020, **10**, 481.
255 Z. Chen, Y. Xu, D. Ding, G. Song, X. Gan, H. Li, W. Wei, J. Chen, Z. Li, Z. Gong, X. Dong, C. Zhu, N. Yang, J. Ma, R. Gao, D. Luo, S. Cong, L. Wang, Z. Zhao and Y. Cui, *Nat. Commun.*, 2022, **13**, 763.
256 L. Han, P. Ou, W. Liu, X. Wang, H. T. Wang, R. Zhang, C. W. Pao, X. Liu, W. F. Pong, J. Song and Z. Zhuang, *Sci. Adv.*, 2022, **8**, eabm3779.
257 W. Wan, Y. Zhao, S. Wei, C. A. Triana, J. Li, A. Arcifa, C. S. Allen, R. Cao and G. R. Patzke, *Nat. Commun.*, 2021, **12**, 5589.
258 B. Hu, A. Huang, X. Zhang, Z. Chen, R. Tu, W. Zhu, Z. Zhuang, C. Chen, Q. Peng and Y. Li, *Nano Res.*, 2021, **14**, 3482–3488.
259 M. He, W. An, Y. Wang, Y. Men and S. Liu, *Small*, 2021, **17**, 2104445.
260 Y. Wang, X. Wan, J. Liu, W. Li, Y. Li, X. Guo, X. Liu, J. Shang and J. Shui, *Nano Res.*, 2021, 1–8.
261 H. Li, S. Di, P. Niu, S. Wang, J. Wang and L. Li, *Energy Environ. Sci.*, 2022, **15**, 1601–1610.
262 J. Liu, W. Luo, L. Wang, J. Zhang, X.-Z. Fu and J.-L. Luo, *Adv. Funct. Mater.*, 2022, **32**, 2110748.

